Wannier-function software ecosystem for materials simulations

Antimo Marrazzo*

Scuola Internazionale Superiore di Studi Avanzati (SISSA), I-34136 Trieste, Italy and Dipartimento di Fisica, Università di Trieste, I-34151 Trieste, Italy

Sophie Beck

Center for Computational Quantum Physics, Flatiron Institute, 162 5th Avenue, New York, New York 10010, USA

Elena R. Margine

Department of Physics, Applied Physics, and Astronomy, Binghamton University–SUNY, Binghamton, New York 13902, USA

Nicola Marzari

Theory and Simulation of Materials (THEOS), and National Centre for Computational Design and Discovery of Novel Materials (MARVEL), École Polytechnique Fédérale de Lausanne, CH-1015 Lausanne, Switzerland and Laboratory for Materials Simulations (LMS), and National Centre for Computational Design and Discovery of Novel Materials (MARVEL), Paul Scherrer Institut (PSI), CH-5232 Villigen PSI, Switzerland

Arash A. Mostofi

Departments of Materials and Physics and the Thomas Young Centre for Theory and Simulation of Materials, Imperial College London, London SW7 2AZ, United Kingdom

Junfeng Qiao

Theory and Simulation of Materials (THEOS), and National Centre for Computational Design and Discovery of Novel Materials (MARVEL), École Polytechnique Fédérale de Lausanne, CH-1015 Lausanne, Switzerland

Ivo Souza and Stepan S. Tsirkin

Centro de Física de Materiales, Universidad del País Vasco, 20018 San Sebastián, Spain and Ikerbasque Foundation, 48013 Bilbao, Spain

Jonathan R. Yates

Department of Materials, University of Oxford, Parks Road, Oxford OX1 3PH, United Kingdom

Giovanni Pizzi†

Laboratory for Materials Simulations (LMS), and National Centre for Computational Design and Discovery of Novel Materials (MARVEL), Paul Scherrer Institut (PSI), CH-5232 Villigen PSI, Switzerland

(published 23 December 2024)

Over the past two decades, following the early developments on maximally localized Wannier functions, an ecosystem of electronic-structure simulation techniques and software packages leveraging the Wannier representation has flourished. This environment includes codes to obtain Wannier functions and interfaces with first-principles simulation software, as well as an increasing number of related postprocessing packages. Wannier functions can be obtained for isolated or

*Contact author: amarrazz@sissa.it

†Contact author: giovanni.pizzi@psi.ch

extended systems (both crystalline and disordered) and can be used to understand chemical bonding; to characterize electric polarization, magnetization, and topology; and as an optimal basis set, providing accurate interpolations in reciprocal space or large-scale Hamiltonians in real space. This review summarizes the current landscape of techniques, materials properties, and simulation codes based on Wannier functions that have been made accessible to the research community and that are now well integrated into what is referred to as a Wannier-function software ecosystem. To begin, the theory and practicalities of Wannier functions, starting with their broad domains of applicability to advanced minimization methods using alternative approaches beyond maximal localization, are introduced. The concept of a Wannier ecosystem and its interactions and interoperability with many quantum simulations engines and postprocessing packages are then defined. The review focuses on some of the key properties and capabilities that are empowered by such an ecosystem (from band interpolations and large-scale simulations to electronic transport, Berryology, topology, electron-phonon couplings, dynamical mean-field theory, embedding, and Koopmans functionals) and concludes with the current status of interoperability and automation. The review aims at highlighting the basic theory and concepts behind codes while providing mentions of more in-depth references. It also elucidates the relationships and connections between codes and, where relevant, the different motivations and objectives behind their development strategies. Finally, an outlook on future developments is provided and comments are made on the goals of biodiversity and sustainability for the entire software ecosystem.

DOI: 10.1103/RevModPhys.96.045008

CONTENTS

I. INTRODUCTION

Wannier functions (WFs) (Wannier, 1937), and, in particular, maximally localized Wannier functions (MLWFs) (Marzari and Vanderbilt, 1997), provide an accurate, compact, and localized representation of the electronic-structure problem and have become widely used in computational condensed-matter physics and materials science (Marzari *et al.*, 2012).

Thanks to developments in theory, algorithms, and implementations over the past few decades, as summarized in Sec. II, it has now become possible to widely apply the concept of MLWFs to single-particle theories, particularly to Kohn-Sham (KS) density-functional theory (DFT) simulations, to obtain localized orbitals from Bloch states, which can themselves be represented with localized or extended basis sets such as plane waves. On the one hand, these developments have benefited from profound connections between WFs and physical quantities such as electric polarization, orbital magnetization, and topological invariants (Vanderbilt

and King-Smith, 1993; Thonhauser *et al.*, 2005; Xiao, Shi, and Niu, 2005; Soluyanov and Vanderbilt, 2011b; Vanderbilt, 2018). On the other hand, the ability to obtain MLWFs from DFT simulations can enable the calculation of physical quantities with high accuracy but at a fraction of the computational cost thanks to their role as accurate interpolators (Souza, Marzari, and Vanderbilt, 2001; Lee, Nardelli, and Marzari, 2005; Yates *et al.*, 2007). Finally, although they are not discussed here, localized representations have long been pioneered by the quantum chemistry community to interpret coordination and bonding (Edmiston and Ruedenberg, 1963), and MLWFs extend to periodic systems the concept of Foster-Boys localized orbitals (Boys, 1966) thanks to algorithmic breakthroughs in calculating the position operator in solids (Blount, 1962; Zak, 1989; Nenciu, 1991; Resta, 1992; King-Smith and Vanderbilt, 1993).

Wannier functions are typically localized or even exponentially localized (Brouder *et al.*, 2007; Panati, 2007; Panati and Pisante, 2013) and, due to the nearsightedness of interacting electrons (Des Cloizeaux, 1964a, 1964b; Kohn, 1996), local electronic properties depend only on the nearby environment (Bianco and Resta, 2011, 2013; Marrazzo and Resta, 2016, 2019). As a consequence, the resulting Hamiltonian matrix expressed in a localized basis set [such as MLWFs (Calzolari *et al.*, 2004; Lee, Nardelli, and Marzari, 2005)] becomes sparse; i.e., it displays negligible matrix elements—or hoppings, in the language of a tight-binding (TB) formalism—if the distance between the corresponding localized basis functions exceeds a given threshold. In this sense MLWFs constitute an optimal choice, as they decay exponentially in real space (Panati and Pisante, 2013) and minimize a localization functional by design (Marzari and Vanderbilt, 1997; Marzari *et al.*, 2012). The resulting MLWFs can be used as a basis set to build, LEGO-like, the electronic structure of large-scale nanostructures (Lee, Nardelli, and Marzari, 2005) [that, thanks to the sparsity of the resulting Hamiltonian matrix, can be solved with linear-scaling methods (Mauri, Galli, and Car, 1993; Ordejón *et al.*, 1993; Nunes and Vanderbilt, 1994)], or as highly accurate interpolators of electronic properties, operators, and quantities defined as integrals over the Brillouin zone (BZ) of periodic systems (Souza, Marzari, and Vanderbilt, 2001; Yates *et al.*, 2007). Interpolation on dense grids becomes essential when fine features need to be resolved, as when integrals are restricted to lower-dimensional manifolds (such as the Fermi surface, in the case of transport properties of metals).

MLWFs are now routinely used in many research areas of condensed-matter physics and materials science. In Sec. II we summarize past and current challenges, discussing how we reached the current state. The flourishing of this field is not only due to theoretical advances but also strongly driven by the concerted development of accessible and efficient software. Indeed, thanks to the availability of robust software packages (often open source, thus encouraging further contributions) and to the user support provided by developers, researchers can now not only easily compute MLWFs but also use them as core ingredients for advanced simulations. As more codes appear, they adopt the *de facto* standardization of input and output formats, resulting in a set of interacting and interoperating codes that we refer to here as the Wannier-function software ecosystem.

This review does not aim to provide an extensive discussion of the theory of MLWFs, for which we refer the interested reader to Marzari *et al.* (2012), although we do provide a general introduction to the field in Sec. I.A. Instead, the goal is to discuss the nature of the ecosystem and the capabilities of existing codes, focusing in Sec. III on a selection of physical phenomena or quantities that can be efficiently predicted thanks to WFs, and on how WFs are used as an ingredient to extend the accuracy of beyond-DFT simulations. Nevertheless, we do mention a few notable developments of the past decade whenever they are useful for contextualizing the theoretical and software developments. Our aim is to help newcomers and existing practitioners alike navigate the ecosystem: which properties can be computed by which codes, when and why the use of WFs is beneficial, which quantities are exchanged between codes, and how interoperability is being addressed.

To facilitate the discussion of the codes, in this review we group them into three major categories: *Wannier engines*, i.e., codes to obtain WFs; *interface codes* between the first-principles engines (for example, DFT or *GW* codes) and the Wannier engines; and *Wannier-enabled codes*, which range from relatively simple postprocessing tools to more advanced codes that use WFs as one of the ingredients to accelerate accurate simulations. A fourth category of codes that we discuss in Sec. III.J encompasses *automation workflows*. Indeed, until recently the generation of WFs typically required human intuition by experienced researchers to provide initial trial orbitals. This barrier has largely been removed through recent algorithmic and automation efforts (see Sec. II.D), thereby enabling the use of WFs both by new users and for high-throughput materials discovery and characterization. In the latter case managing thousands (or more) simulations poses new challenges that require not only the use of robust workflow engines but also the implementation of WF-specific workflows to effectively interconnect multiple codes within the ecosystem. We conclude in Sec. IV with some perspectives on the field related to the sustainability of the entire effort, current challenges that still need to be addressed, and possible future developments.

A. *Ab initio* electronic structure and Wannier functions

Electronic-structure simulations aim to determine the behavior of electrons in materials and molecules, as governed by the Schrödinger or Dirac equations. Electrons feel Coulomb interactions among themselves and with the nuclei, in addition to couplings with external fields (for example, electrical, magnetic, or electromagnetic) or perturbations (such as strain and phonons). The core electrons of heavy chemical elements can reach relativistic speeds, thus requiring the Schrödinger equation to be corrected with terms obtained from an expansion of the Dirac equation in powers of $1/c^2$, where c is the speed of light. The most relevant relativistic correction is spin-orbit coupling, which is responsible for several important phenomena related to magnetism and to geometrical and topological properties of the electronic manifold; see Secs. III.E and III.F.

An exact solution of the Schrödinger equation (either a bare solution or one with relativistic corrections) would give access to essentially all properties of materials. This problem was already clear in 1929 when Paul Dirac declared, "The underlying physical laws necessary for the mathematical theory of a large part of physics and the whole of chemistry are thus completely known, and the difficulty is only that the exact application of these laws leads to equations much too complicated to be soluble" (Dirac, 1929).

For more than 50 years, *ab initio* or first-principles methods have been developed to approximately solve the Schrödinger equation in realistic settings (Giustino, 2014; Martin, 2020), with more accurate strategies and theories being developed. In parallel the exponential growth of computational power (Moore's law) has allowed these new theoretical instruments to be deployed through numerical simulations that constantly seek to not only improve accuracy but also target more complex and realistic systems. Numerical solutions quickly became sufficiently accurate to be predictive for a number of properties in relevant systems: the era of first-principles materials modeling had begun (Yin and Cohen, 1980; Marzari, Ferretti, and Wolverton, 2021).

An iconic example is given by DFT, which has made it possible to determine the electronic structure of complex materials with reasonable accuracy at low cost. In DFT the total energy of the electrons is expressed as a functional of the electronic charge density (Giustino, 2014; Martin, 2020). The theory is supported by two pillars, the Hohenberg-Kohn theorems, which not only state a one-to-one correspondence between the ground-state many-body wave function and the ground-state charge density but also formulate a variational total-energy functional: the solution of the Schrödinger equation can be recast as a minimization problem for the charge density, a much simpler object (a real function of $\mathbf{r}$) than the many-body wave function we started from (a complex function of $3N_e$ variables, where N_e is the number of electrons in the system).

In KS DFT the interacting many-body problem is mapped onto a noninteracting problem sharing the same ground-state charge density but in the presence of a suitable local external potential; the latter is generally unknown. This ansatz enables the kinetic energy contribution to be calculated accurately through the second derivatives of the KS orbitals; this quantity is difficult to calculate directly from the charge density alone. The success of DFT has been possible thanks also to the discovery and development of simple functionals that approximate the exact, but unknown, total-energy functional. Hence, the KS-DFT approach to solving the many-body Schrödinger equation translates into solving a set of noninteracting one-particle Schrödinger equations in the presence of an external potential that depends, self-consistently, upon the charge density only. Although the importance of DFT was recognized through the 1998 Nobel Prize in Chemistry awarded to Walter Kohn (for DFT) and John Pople (for computational methods in quantum chemistry), its impact on the physics community has been, if possible, even greater: the top ten most highly cited articles published by the American Physical Society deal with DFT and its related applications (Talirz, Ghiringhelli, and Smit, 2021).

The electronic structure of materials and molecular systems is at the same time both similar and different. To some extent extended bulk materials can be seen as large molecules and one could focus on the local electronic structure in real space, which is periodically repeated in the case of crystalline materials such as metals, semiconductors, and oxides. This viewpoint is supported by the mathematical structure of the Schrödinger equation and its solutions, as observed by Kohn (1996): the electronic structure is fundamentally a local property, "nearsighted" to what happens farther away in real space. The effect of chemical bonding and the presence of the lattice can be seen as perturbations to the case of isolated atoms, with their well-defined s, p, d, and f orbitals. This perspective is powerful and foundational for linear-scaling methods, which target the simulation of large systems and leverage a description based on localized orbitals. Yet, materials are not just large molecules, and "more is different" (Anderson, 1972). Extended systems are practically infinite and can thus be described using periodic boundary conditions (PBCs). As discussed in more formal terms in Sec. II, the electronic structure of a material under PBCs is more naturally described in terms of Bloch orbitals, which are not localized in real space. Indeed, a different perspective often drives the discussion of the electronic structure of periodic crystals: the behavior in reciprocal (i.e., Fourier-transformed) space. A textbook example is semiconductor physics, which is in general much better understood (and taught) by studying solutions of the Schrödinger equation in such reciprocal space. This approach, which is somewhat orthogonal to the large-molecule perspective, is indeed also powerful at both a conceptual and a practical level. As a side note, many electronic-structure codes for materials actually adopt a completely delocalized basis (for example, plane waves) to describe the periodic part of the Bloch orbitals (Pickett, 1989; Martin, 2004, 2020).

How can we reconcile these two (almost opposite) perspectives? One can use the fundamental "gauge freedom" of quantum mechanics: First, any quantum state is defined modulo a phase factor. Second, if one considers a set of single-particle states separated in energy from other states, then any trace operation on this manifold is invariant with respect to any unitary transformation among the orbitals; we call this a generalized gauge freedom. However—and this is the crucial aspect—the localization properties of that set of states strongly depend on their gauge.

WFs provide a rigorous and insightful way to reconcile the real-space and localized perspective with the reciprocal-space (Fourier) and delocalized one. As clarified in Sec II, MLWFs, in particular, exploit the generalized gauge freedom to transform delocalized orbitals into localized ones (and vice versa) by constructing the proper unitary matrices.

II. WANNIER-FUNCTION FUNDAMENTALS

The electronic structure of periodic crystals is most commonly described in terms of Bloch waves $\psi_{n\mathbf{k}}(\mathbf{r}) = u_{n\mathbf{k}}(\mathbf{r})e^{i\mathbf{k}\cdot\mathbf{R}}$, where $\mathbf{k}$ is the crystal momentum and n is the band index. This is the case in textbooks on solid-state theory, but also for the many software packages that solve the KS

equations for crystalline solids. A few years after Felix Bloch developed the theory of electron waves in periodic crystals (Bloch, 1929), Gregory Wannier introduced an alternative representation in terms of an orthonormal set of localized functions (Wannier, 1937), the Wannier functions. Given an isolated Bloch band n, the WF $w_{n\mathbf{R}}(\mathbf{r}) = \langle \mathbf{r}|\mathbf{R}n\rangle = w_{n\mathbf{0}}(\mathbf{r}-\mathbf{R})$ associated with the unit cell labeled as lattice vector $\mathbf{R}$ is defined as (Wannier, 1937)

$$|\mathbf{R}n\rangle = \frac{V_{\text{cell}}}{(2\pi)^3}\int_{\text{BZ}} d\mathbf{k}\, e^{-i\mathbf{k}\cdot\mathbf{R}}|\psi_{n\mathbf{k}}\rangle, \tag{1}$$

where V_{cell} is the unit-cell volume.

Since their inception, WFs have been employed as a conceptual tool to tackle problems in solid-state physics; see Kivelson (1982). However, in the first 60 years following Wannier's paper, there were few actual calculations of WFs for real materials; see Callaway and James Hughes (1967), Satpathy and Pawlowska (1988), and Sporkmann and Bross (1994). The main obstacle was the fact that WFs are strongly nonunique, as they are sensitive to the generalized gauge freedom discussed earlier, for example, to k-dependent phase changes $|\psi_{n\mathbf{k}}\rangle \to e^{-i\beta_{n\mathbf{k}}}|\psi_{n\mathbf{k}}\rangle$, with $\beta_{n\mathbf{k}} \in \mathbb{R}$ (gauge transformations), of the Bloch eigenstates. In addition, the energy bands of real materials typically become degenerate at points, lines, or even entire planes in the BZ. The presence of degeneracies leads to poor localization properties of the WFs obtained from Eq. (1) because no matter how the phase factors $e^{-i\beta_{n\mathbf{k}}}$ are chosen, the Bloch eigenfunctions are nondifferentiable functions of $\mathbf{k}$ at the degeneracy points.

A. Maximally localized Wannier functions

In the following we discuss the widely used Wannierization methods introduced by Marzari and Vanderbilt (1997) and Souza, Marzari, and Vanderbilt (2001); see Sec. II.D for an overview of more recent and advanced minimization methods.

1. Isolated composite groups of bands

Consider a group of J Bloch bands of orthonormal $|\psi_{n\mathbf{k}}\rangle$ Bloch states that may be connected among themselves by degeneracies but are isolated from all lower or higher bands, such as the six valence bands in Fig. 3. Given such a composite group, the most general expression for the associated WFs is (Marzari and Vanderbilt, 1997)

$$|\mathbf{R}j\rangle = \frac{V_{\text{cell}}}{(2\pi)^3}\int_{\text{BZ}} d\mathbf{k}\, e^{-i\mathbf{k}\cdot\mathbf{R}}|\psi^{\text{W}}_{j\mathbf{k}}\rangle, \tag{2a}$$

$$|\psi^{\text{W}}_{j\mathbf{k}}\rangle = \sum_{n=1}^{J}|\psi_{n\mathbf{k}}\rangle U_{\mathbf{k},nj}, \tag{2b}$$

where $U_{\mathbf{k}}$ are $J\times J$ unitary matrices that describe the generalized (multiband) gauge freedom within the Bloch manifold at each $\mathbf{k}$. The superscript W denotes a Wannier gauge, as opposed to a Hamiltonian gauge (later denoted by H), where the Hamiltonian matrix is diagonal. Note that, unlike in Eq. (1), in Eq. (2) there is not a one-to-one correspondence between the band index n and the intracell Wannier index j.

Marzari and Vanderbilt (1997) introduced the concept of MLWFs, in which the $U_{\mathbf{k}}$ matrices are chosen so as to minimize the total quadratic spread of the WFs,

$$\Omega = \sum_{j=1}^{J}[\langle \mathbf{0}j|r^2|\mathbf{0}j\rangle - |\langle \mathbf{0}j|\mathbf{r}|\mathbf{0}j\rangle|^2]. \tag{3}$$

As discussed in Sec. II.C.1, the spread (also known as localization) functional Ω and its gradient with respect to an infinitesimal gauge transformation can be expressed in reciprocal space; furthermore, the BZ integration in Eq. (2) is replaced by a discrete sum $(1/N)\sum_{\mathbf{k}}$, where N is the number of k points in the finite grid used in the numerical simulations and the optimal $U_{\mathbf{k}}$ matrices are found by iteratively minimizing the functional Ω; see Marzari and Vanderbilt (1997) for the mathematical details.

From general Fourier-transform considerations (Duffin, 1953), the good real-space localization properties of the MLWFs on the left-hand side of Eq. (2) mean that the Bloch-like states $|\psi^{\text{W}}_{j\mathbf{k}}\rangle$ appearing on the right-hand side are smooth functions of $\mathbf{k}$ for the optimal choice of $U_{\mathbf{k}}$ matrices in Eq. (2b) (or for any other choice leading to well-localized WFs).

The details of the Marzari-Vanderbilt (MV) methodology were given by Marzari and Vanderbilt (1997) and Marzari *et al.* (2012); in the case of single k-point sampling (large unit cells), it is equivalent to the Foster-Boys scheme used in quantum chemistry to construct localized molecular orbitals (Boys, 1966). It should be noted that other localization criteria can be used for the purpose of obtaining localized orbitals, such as the Edmiston-Ruedenberg (Edmiston and Ruedenberg, 1963) and Pipek-Mizey approaches (Pipek and Mezey, 1989), which are based on maximizing the Coulomb self-repulsion of the orbitals and the sum of the squares of the Mulliken charges (Mulliken, 1955) associated with the orbitals, respectively. While these approaches are more challenging to adapt to a periodic, multi-k-point formulation, there has been recent work to obtain WFs for periodic systems using the Pipek-Mizey localization criterion (Jónsson *et al.*, 2017; Clement, Wang, and Valeev, 2021). Nevertheless, the MV approach of minimizing the quadratic spread is still the most widely used approach for periodic systems.

To provide an illustrative example of the Wannierization procedure, we now discuss the simple example of a slightly dimerized polyynelike carbon chain, i.e., a chain of carbon atoms with two atoms per unit cell and alternating distances d_1 and d_2. Figure 1 displays the results of actual DFT calculations, where carbon-carbon distances are $d_1 = 1.245$ Å and $d_2 = 1.345$ Å, and the lattice parameter is thus $a = 2.6$ Å. We compute the electronic band structure of this linear chain with the `Quantum ESPRESSO` code (Giannozzi *et al.*, 2009, 2017), which uses pseudopotentials with a plane-wave basis set, where the bands originating from the 1s orbitals of carbon are not explicitly computed. If these 1s core orbitals were computed explicitly, they would form almost-flat bands (since the orbitals are highly localized) at lower energy. At the center

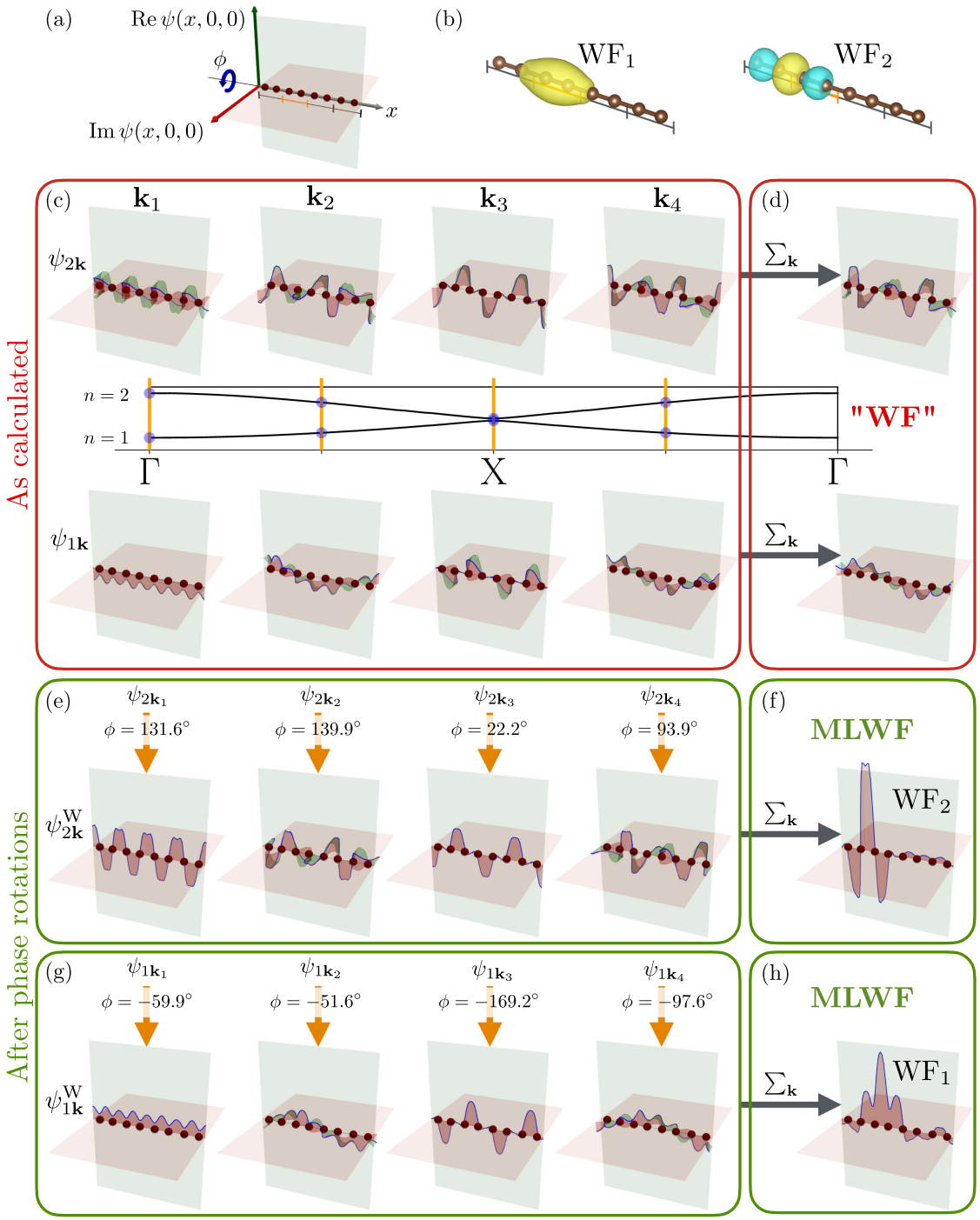

FIG. 1. Band-by-band Wannierization of the two lowest bands of a dimerized carbon chain. (a) Graphical representation of the 4-times-longer supercell where all quantities are plotted in (c)–(h). Given our sampling of the BZ with four k points, both the Bloch states and the WFs have the supercell periodicity. The eight carbon atoms are represented as dark (red) spheres, and the primitive cell of length a is marked as the orange (gray) segment. As marked in (a), one axis is the real-space x axis of the carbon chain, while the other two are used to plot the real and imaginary components (green and red, respectively) of complex wave functions $\psi(x,0,0)$ along x (the profiles are highlighted in blue in subsequent panels). Multiplying ψ by a phase factor $e^{i\phi}$ corresponds to a rotation by an angle ϕ, as indicated by the circular arrow. (b) 3D isosurfaces of the resulting MLWFs for each of the two bands (band $n=1$ leads to WF_1 and $n=2$ leads to WF_2). (c) The Bloch orbitals $\psi_{n\mathbf{k}}$ as calculated by the *ab initio* (DFT) code at the k points $\mathbf{k}_1=\Gamma=(0,0,0)$, $\mathbf{k}_2=(\pi/2a,0,0)$, $\mathbf{k}_3=X=(\pi/a,0,0)$, and $\mathbf{k}_4=(3\pi/2a,0,0)$, which are indicated by the blue dots and vertical orange lines in the center, together with the full DFT band structure. (d) The sum of these Bloch orbitals, as in the original Wannier definition of Eq. (1), delivers WFs that are not well localized (labeled "WF" in the panel). (e) The construction of a MLWF associated with the second lowest band ($n=2$). For an isolated band in one dimension, the procedure amounts to a complex phase rotation at each k point; the optimal values of these complex phases for this specific example are indicated. (f) The sum of these rotated Bloch states results in the MLWF WF_2, which is also shown in (b). (g),(h) Same as (e) and (f), but for the lowest band ($n=1$).

of Fig. 1(c), we show the two lowest bands considered in the DFT calculation. A projected density of states calculation (not shown in the figure) shows that these two lowest bands originate from a combination of $2s$ and $2p_x$ orbitals centered on the two atoms in the unit cell. In addition to being separated from all other bands, these two bands are also separated from each other by a small gap at X (the two bands would instead be degenerate at X for a nondimerized chain, i.e., when $d_1 = d_2$). Therefore, they are isolated, and each of them can be Wannierized separately.

In Fig. 1(c) we also plot the wave functions $\psi_{n\mathbf{k}}$ as provided by the *ab initio* engine, computed on a regular $4 \times 1 \times 1$ grid in the BZ composed of the four points $\mathbf{k}_1 = \Gamma = (0,0,0)$, $\mathbf{k}_2 = (\pi/2a, 0, 0)$, $\mathbf{k}_3 = X = (\pi/a, 0, 0)$, and $\mathbf{k}_4 = (3\pi/2a, 0, 0)$. The legend to interpret these plots is provided in Fig. 1(a). In particular, we represent the real (green) and imaginary (red) components of complex wave functions ($\psi_{n\mathbf{k}}$, $\psi^{\mathrm{W}}_{n\mathbf{k}}$, etc.) along the x axis passing through the carbon chain, i.e., $\psi_{n\mathbf{k}}(x, 0, 0)$. Given the $4 \times 1 \times 1$ sampling of the BZ, both the wave functions and the resulting WFs are periodic in a real-space $4 \times 1 \times 1$ supercell, i.e., the same one shown in Fig. 1. Note that, while in most cases the $\psi_{n\mathbf{k}}$ are eigenstates of the Hamiltonian, this might not be true for all codes. In general, the phases of each state $\psi_{n\mathbf{k}}$ are random (for example, they often come from independent diagonalizations at each k point). In addition, if we consider multiple bands with degeneracies, then the degenerate states would also be randomly mixed among each other. (This would happen at the k point X for a nondimerized chain, as discussed earlier.) As a consequence, the simple sum of the $\psi_{n\mathbf{k}}$ according to Eq. (1) does not provide a well-localized function, as shown in Fig. 1(d).

However, each $\psi_{n\mathbf{k}}$ at every k point can be rotated by the optimized $U_{\mathbf{k}}$ matrices obtained from a Wannierization procedure. In this case, since $J = 1$, the $U_{\mathbf{k}}$ at each k point is a 1×1 matrix, i.e., simply a complex phase $U_{\mathbf{k}} = e^{i\phi_{\mathbf{k}}}$ that can be visualized as a rotation in the plot; this is marked with the circular blue arrow in Fig. 1(a). In this simple one-dimensional case (i.e., for a single band), the Wannierization is essentially trivial, as discussed by Marzari and Vanderbilt (1997). One simply has to require that the same-band overlaps between adjacent k points be equal to $e^{i\phi_n/4}$, where ϕ_n is the Berry phase of the entire band n and the factor $1/4$ accounts for the fact that there are four k points; see Eq. (69) in Sec. III.F for a discussion of Berry phases. This condition is realized by making the appropriate phase rotations $e^{i\phi_{\mathbf{k}}}$ at every k point that counterbalance the random phases coming from the *ab initio* code, thus delivering maximal smoothness in reciprocal space, corresponding to the so-called twisted parallel-transport gauge (Vanderbilt, 2018). The rotated states $\psi^{\mathrm{W}}_{n\mathbf{k}}$ are shown in Figs. 1(e) and 1(g) for the second lowest ($n = 2$) and lowest bands ($n = 1$), respectively. When these $\psi^{\mathrm{W}}_{n\mathbf{k}}$ are summed as prescribed by Eq. (2), localization emerges and we obtain the final MLWFs WF_1 and WF_2, shown in Figs. 1(f) and 1(h), respectively, and in Fig. 1(b) as 3D isosurfaces. Note that a final global phase rotation might be required to ensure real-valued MLWFs. Intuitively, WF_1 can be interpreted as predominantly originating from a linear combination of s orbitals on the C atoms, while WF_2 can be interpreted as predominantly originating from a linear combination of p_x orbitals on the C atoms (with opposite signs so that the positive part of the p_x orbitals centered on two neighboring C atoms sums constructively in the middle of the C–C bond).

We can also treat the two bottom energy bands as a composite group. In this case $U_{\mathbf{k}}$ are 2×2 unitary matrices whose action on the Bloch wave functions

$$(\psi^{\mathrm{W}}_1 \psi^{\mathrm{W}}_2) = (\psi_1 \psi_2) \begin{pmatrix} U_{11} & U_{12} \\ U_{21} & U_{22} \end{pmatrix} \tag{4}$$

is schematically represented in Fig. 2(a). We note that, in such a simple case with only two bands, the action of a unitary matrix could generally be interpreted as a sequence of complex phase rotations of the two initial states, a rotation that mixes the two states, and a final additional complex phase rotation between the two final states. In this case each pair of $\psi_{n\mathbf{k}}$ at every k point can be mixed by the optimized $U_{\mathbf{k}}$ matrices obtained from a Wannierization procedure. The rotated states $\psi^{\mathrm{W}}_{n\mathbf{k}}$ are shown in Fig. 2(e) [we repeat in Figs. 2(c) and 2(d) the same band structure and $\psi_{n\mathbf{k}}$ wave functions as in Figs. 1(c) and 1(d)]. When these $\psi^{\mathrm{W}}_{n\mathbf{k}}$ are summed as prescribed by Eq. (2), we obtain the final MLWFs $|\mathbf{R}j\rangle$ ($j = 1$ and 2) shown in Fig. 2(f), and localization is now apparent (Fig. 2 shows the MLWFs for $\mathbf{R} = \mathbf{0}$). As before, a final global phase rotation might be required to ensure real-valued MLWFs. Finally, we note that, since we now give more freedom to the states to mix, the resulting MLWFs are more localized than those in Fig. 1(b). In addition, the two WFs of Fig. 1 (separate Wannierization) can be obtained as a linear combination of the eight WFs of Fig. 2 (combined Wannierization), i.e., WF_1 and WF_2 translated by $\mathbf{R}_{-1} = (-a, 0, 0)$, $\mathbf{R}_0 = (0,0,0)$, $\mathbf{R}_1 = (a, 0, 0)$, and $\mathbf{R}_2 = (2a, 0, 0)$. The opposite is also true: WF_1 and WF_2 of Fig. 2 are a linear combination of the eight WFs of Fig. 1 translated by $\mathbf{R}_{-1}$, $\mathbf{R}_0$, $\mathbf{R}_1$, and $\mathbf{R}_2$.

2. Entangled bands

The previously described MV approach provides a means to construct well-localized WFs from isolated groups of bands, such as the valence bands of insulators. However, it is often useful to obtain WFs from nonisolated (or "entangled") groups of bands. Typical examples include the low-lying conduction bands or the valence plus conduction bands of insulators (see Fig. 3), and the bands crossing the Fermi level in metals.

A possible strategy to deal with such cases is to first identify an appropriate J-dimensional Bloch manifold at each k point from a larger set of $\mathcal{J}_{\mathbf{k}}$ Bloch eigenstates $|\psi_{m\mathbf{k}}\rangle$, for example, the ones within some energy window. Formally, this band-disentanglement step can be expressed as

$$|\tilde{\psi}_{n\mathbf{k}}\rangle = \sum_{m=1}^{\mathcal{J}_{\mathbf{k}}} |\psi_{m\mathbf{k}}\rangle \tilde{V}_{\mathbf{k},mn}, \tag{5}$$

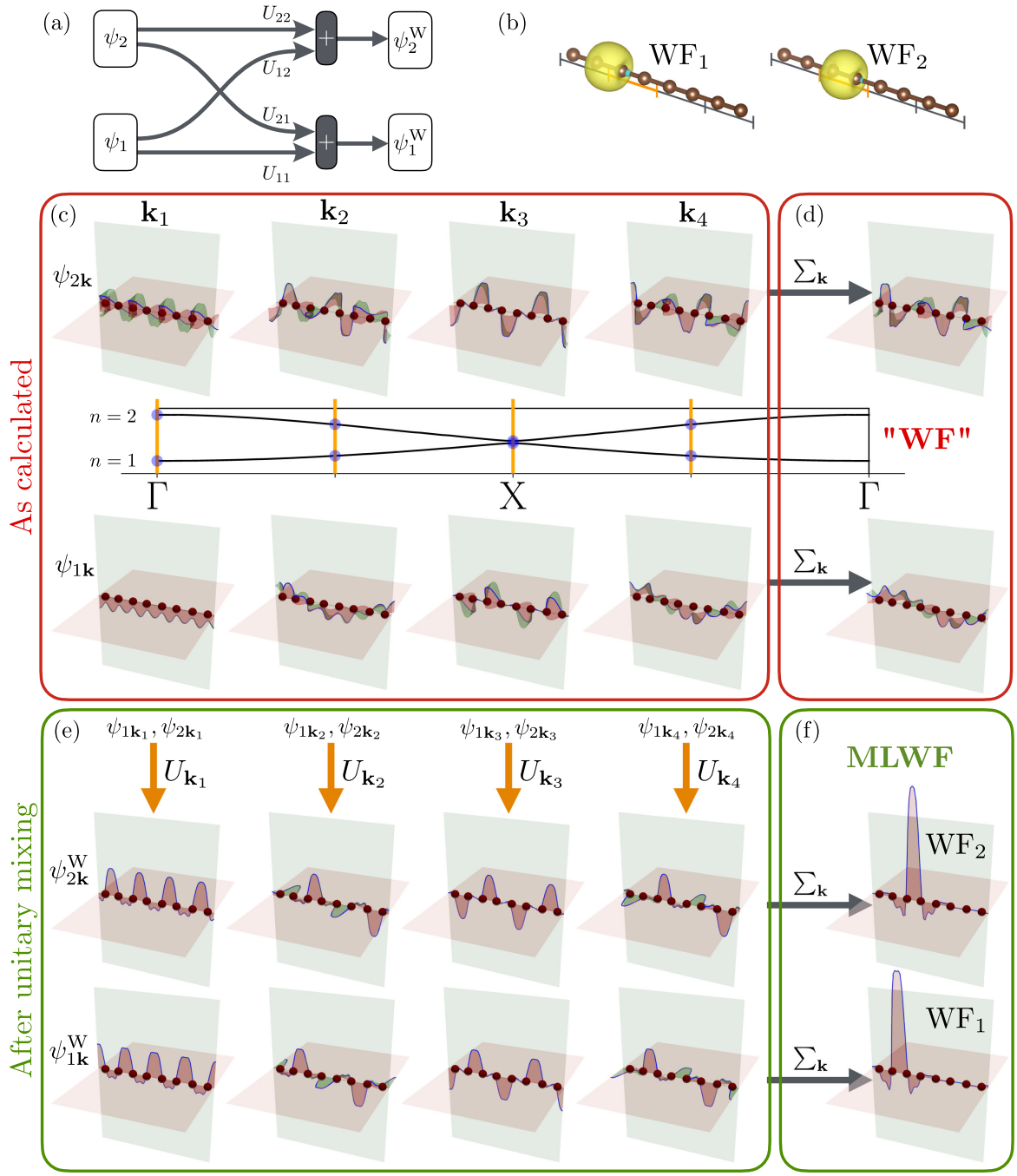

FIG. 2. Same as Fig. 1 but now treating the two lowest bands as a composite group. (a) Graphical representation of the generalized gauge transformation $U_{\mathbf{k}}$ in Eq. (4) that mixes the Bloch states from the two bands. As the result of this mixing, it is no longer possible to associate each MLWF obtained from Eq. (1) with a specific band. By taking advantage of the generalized gauge freedom, the two composite MLWFs in the $\mathbf{R} = 0$ cell, shown in (b) and (f), are better localized than their single-band counterparts in Fig. 1. Note that WF_1 and WF_2 are not identical (i.e., they are not related by a rigid translation), even though they are both bond centered and look similar. This is because the chain is dimerized, and thus the respective bond lengths are different.

where $\tilde{V}_{\mathbf{k}}$ are $\mathcal{J}_{\mathbf{k}} \times J$ matrices satisfying $\tilde{V}_{\mathbf{k}}^{\dagger}\tilde{V}_{\mathbf{k}} = \mathbb{1}_{J\times J}$. Souza, Marzari, and Vanderbilt (2001) introduced a practical scheme to extract an optimally smooth Bloch-like subspace $\hat{P} = \sum_{n=1}^{J} |\tilde{u}_{n\mathbf{k}}\rangle\langle\tilde{u}_{n\mathbf{k}}|$ across the BZ, from which a set of MLWFs could then be obtained using the MV prescription. The resulting "disentangled WFs" are given by Eq. (2), with the *ab initio* Bloch eigenstates $|\psi_{n\mathbf{k}}\rangle$ therein replaced by the disentangled Bloch-like states $|\tilde{\psi}_{n\mathbf{k}}\rangle$, that is,

$$|\mathbf{R}j\rangle = \frac{1}{N}\sum_{\mathbf{k}} e^{-i\mathbf{k}\cdot\mathbf{R}} |\psi_{j\mathbf{k}}^{\mathrm{W}}\rangle, \tag{6a}$$

$$|\psi_{j\mathbf{k}}^{\mathrm{W}}\rangle = \sum_{n=1}^{\mathcal{J}_{\mathbf{k}}} |\psi_{n\mathbf{k}}\rangle V_{\mathbf{k},nj}, \tag{6b}$$

where the $\mathcal{J}_{\mathbf{k}} \times J$ matrices $V_{\mathbf{k}} = \tilde{V}_{\mathbf{k}} U_{\mathbf{k}}$ encode the net result of the disentanglement (subspace-selection) and

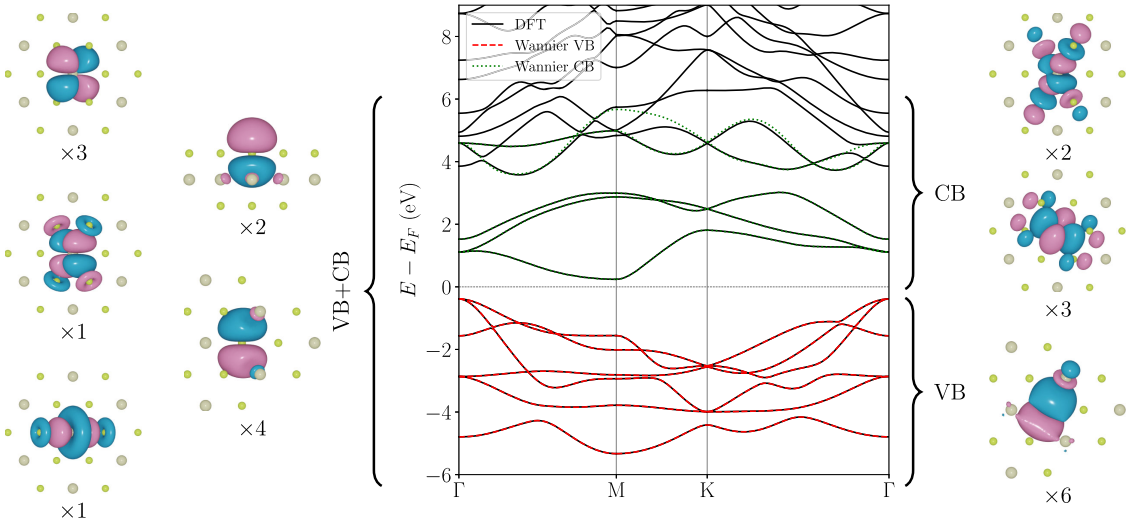

FIG. 3. MLWFs and band structure of the 2D material $HfSe_2$. Center panel: comparison between the DFT band structure (black lines) and the Wannier-interpolated band structure from valence MLWFs only (VB; red dashed lines) and from low-lying conduction MLWFs only (CB; green dotted lines) are shown. Note that the Wannier-interpolated bands from both valence and conduction (VB + CB) MLWFs are not shown, since they are visually indistinguishable from the combination of the VB and CB MLWFs. Left panels: real-space shapes of 11 valence and conduction MLWFs, obtained starting with Hf d and Se p initial guess orbitals, followed by disentanglement (see Sec. II.A.2) from high-energy conduction states. Specifically, three of them resemble $d_{xy,xz,yz}$ orbitals, one resembles a d_{z^2} orbital, one resembles a $d_{x^2-y^2}$ orbital, and the remaining six resemble p orbitals. Some small hybridization with orbitals from nearby atoms is visible. Right panels: real-space shapes of six valence MLWFs (lower panel) and five conduction MLWFs (upper panel). The valence MLWFs span an isolated group of bands (see Sec. II.A.1) and are composed of six hybridized bonding orbitals, where the Hf d and Se p orbitals overlap constructively. The conduction MLWFs are instead five hybridized antibonding orbitals, where Hf d and Se p orbitals overlap destructively, forming nodal planes close to bond centers. The notation $\times n$ below each shape denotes the multiplicity of the corresponding MLWF, i.e., n MLWFs having similar shapes but different spatial orientation.

maximal-localization (gauge-selection) steps. As in the case of Eq. (2), the states $|\psi^{\mathrm{W}}_{j\mathbf{k}}\rangle$ in Eq. (6) are smooth functions of $\mathbf{k}$ whenever the associated WFs are well localized.

The disentanglement step can be carried out in such a way that the *ab initio* eigenstates are described exactly within a "frozen" or "inner" energy window that is contained by the "outer" energy window mentioned earlier (Souza, Marzari, and Vanderbilt, 2001). This is useful when studying transport properties, for which one wants to obtain a faithful description of the states within some small energy range around the Fermi level. Note that, because of these energy windows, the required input from the first-principles calculation includes the energy eigenvalues $\varepsilon_{n\mathbf{k}}$ in addition to the overlap matrices Eq. (12). For illustrative purposes in Fig. 4 we display the $\tilde{V}_{\mathbf{k}}$ matrices as calculated for the carbon chain discussed earlier. We also stress that, in this simple illustrative example, we can exactly disentangle all six bands from the rest, but this is not true in general; see the conduction bands in Fig. 3.

Over the years many alternative approaches and algorithms have been developed—from partially occupied Wannier functions (Thygesen, Hansen, and Jacobsen, 2005; Fontana *et al.*, 2021) to quasiatomic orbitals (Qian *et al.*, 2008) to the selected columns of the density matrix (SCDM) (Damle, Lin, and Ying, 2015; Damle, Lin, and Ying, 2017) to projectability disentanglement and manifold remixing (Qiao, Pizzi, and Marzari, 2023a; Qiao, Pizzi, and Marzari, 2023b). These and other approaches are discussed in Sec. II.D.

3. The projection method

The MV and Souza-Marzari-Vanderbilt (SMV) approaches leverage iterative minimization. Hence, a good starting guess for the unitary matrices $U_{\mathbf{k}}$ and $\tilde{V}_{\mathbf{k}}$ is crucial to avoid being trapped in local minima of the spread functional. A popular approach is the *projection method*, where a set of J localized "trial functions" $g_n(\mathbf{r})$ are chosen by guessing the orbital character and location of the target WFs. These functions are typically Gaussians, atomiclike orbitals with angular character such as s, p, and d or hybrid orbitals such as sp^3. The first step is to project the Bloch manifold onto these trial orbitals,

$$|\phi_{n\mathbf{k}}\rangle = \sum_{m=1}^{\mathcal{J}_{\mathbf{k}}} |\psi_{m\mathbf{k}}\rangle\langle\psi_{m\mathbf{k}}|g_n\rangle. \tag{7}$$

Then Löwdin orthonormalization is performed by inverting the overlap matrix $S_{\mathbf{k},mn} = \langle\phi_{m\mathbf{k}}|\phi_{n\mathbf{k}}\rangle = (A^\dagger A)_{\mathbf{k},mn}$,

$$|\tilde{\psi}_{n\mathbf{k}}\rangle = \sum_{m=1}^{\mathcal{J}_{\mathbf{k}}} |\psi_{m\mathbf{k}}\rangle(A_{\mathbf{k}} S_{\mathbf{k}}^{-1/2})_{mn}, \tag{8}$$

where $A_{\mathbf{k},mn} = \langle\psi_{m\mathbf{k}}|g_n\rangle$ is called the projection matrix. The matrix $A_{\mathbf{k}} S_{\mathbf{k}}^{-1/2}$ is unitary and can be computed through the singular value decomposition of $A = ZDW$,

$$A_{\mathbf{k}} S^{-1/2} = Z\mathbb{1}W, \tag{9}$$

where the diagonal matrix D is replaced by the identity $\mathbb{1}$.

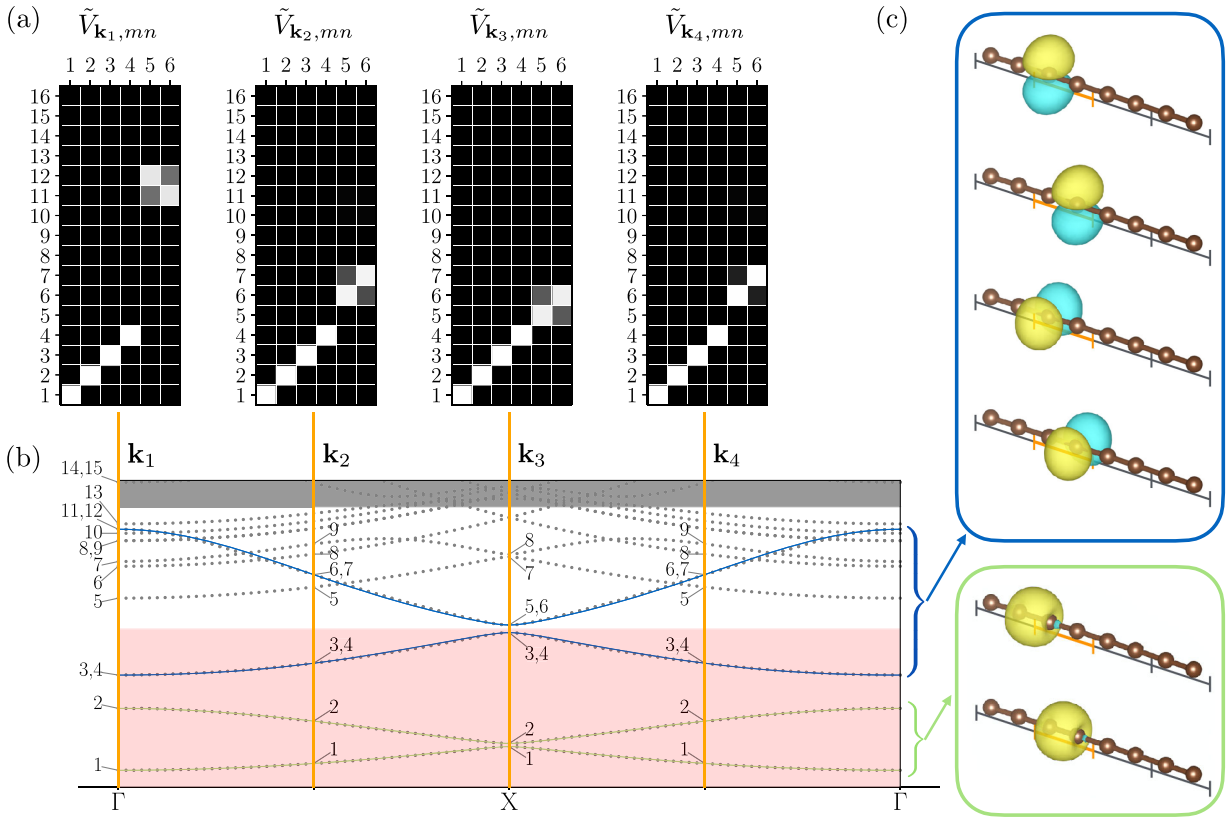

FIG. 4. Illustration of the disentanglement procedure for the same linear carbon chain as in Figs. 1 and 2. (a) Graphical representation of the $\tilde{V}_{\mathbf{k},mn}$ matrices in Eq. (5) at k points $\mathbf{k} = \mathbf{k}_1, \mathbf{k}_2, \mathbf{k}_3$, and $\mathbf{k}_4$. The color scale represents the absolute values of the matrix elements from black (zero) to white (maximum absolute value). The index m (from 1 to 16) labels the bands, and the index n (from 1 to 6) labels the disentangled Bloch states $|\tilde{\psi}_{n\mathbf{k}}\rangle$. (b) Band structure of the carbon chain. Dotted gray points denote the DFT bands, whereas solid lines indicate the disentangled (Wannier-interpolated) bands. The frozen energy window is shown with a red (light gray) background, while the energy range with the dark gray background is outside the disentanglement window. The relevant band indices at $\mathbf{k}_1$, $\mathbf{k}_2$, $\mathbf{k}_3$, and $\mathbf{k}_4$ are indicated. The six disentangled bands are shown: the bottom two are the same bands as in Figs. 1 and 2, while the top four are doubly degenerate. To construct the topmost four bands, the disentanglement procedure correctly picks up the optimally connected DFT bands as a function of $\mathbf{k}$: bands 11 and 12 at $\mathbf{k}_1$, bands 6 and 7 at $\mathbf{k}_2$ and $\mathbf{k}_4$, and bands 5 and 6 at $\mathbf{k}_3$. Notably, in this example the four topmost bands can be exactly disentangled from all other DFT bands such that the disentangled bands coincide at every $\mathbf{k}$ with the corresponding DFT bands. We note, however, that this is not possible in general for an arbitrary band structure; compare these bands to the conduction bands in Fig. 3. (c) Resulting MLWFs on a $4 \times 1 \times 1$ supercell [the primitive unit cell is indicated by the orange (gray) segment]. Since in this example the disentanglement matrices $\tilde{V}$ are block diagonal (as well as the U matrices from the Wannierization procedure, which are not shown), the two bondinglike MLWFs originate only from the bottom two bands and do not mix with the four p_y and p_z MLWFs from the other four bands.

The choice of trial orbitals is less critical for composite bands than for entangled bands, and for simple compounds even a set of Gaussians randomly centered in the cell might work. We emphasize that if the manifold of composite bands coincides with the valence bands of an insulator or semiconductor, then the MLWFs will reflect the local chemistry. For instance, in covalent materials MLWFs are typically bond centered as in Si or GaAs (Marzari and Vanderbilt, 1997), with some notable exceptions such as MoS_2 (Gibertini, Pizzi, and Marzari, 2014) where one WF is centered in the middle of the hexagonal cell due to the hybridization of several orbitals. On the contrary, the SMV disentanglement hinges on a careful choice of trial functions that defines the orbital character of the bands to be extracted. While disentangling the valence and conduction manifold often yields atom-centered WFs, this is not true in general: MLWFs for the low-lying bands of copper result in five Cu d-like WFs and two additional WFs centered at the tetrahedral-interstitial sites (Souza, Marzari, and Vanderbilt, 2001). Different aspects of the projection method are discussed in Secs. II.C and II.D.

B. Major applications of Wannier functions

1. Interpolation

An efficient interpolation in reciprocal space of k-dependent quantities, arguably the most common application of WFs, enables the calculation of electronic-structure properties that can be simple (for example, the band structure) or complex (for example, electron-phonon coupling). A large part of this review is devoted to the fundamentals of WF interpolation (Sec. III.C) and their applications, including ballistic transport (Sec. III.D), Berry-phase-related properties (Sec. III.E), and

electron-phonon interactions (Sec. III.G). As discussed in Sec. III.C, the reason for such a widespread set of applications (not all of which are covered in this review) is that WFs can be easily applied to any generic operator that is local in reciprocal space, i.e., any lattice-periodic operator. More generally we note that even some nonlocal operators in reciprocal space (such as those containing the position operator, which is not lattice periodic and transforms into k derivatives) can also be interpolated; see the discussion of "Berryology" in Sec. III.E. Equally important is that WFs allow the correct band connectivity to be reproduced: in particular, avoided crossings are not mistaken for actual crossings. This distinguishes Wannier interpolation from other methods based on direct Fourier interpolation of the energy eigenvalues. In other words, WFs allow one to exploit the fundamental locality ["nearsightedness," according to Kohn (Des Cloizeaux, 1964a, 1964b; Kohn, 1996)] of the electronic structure and the related exponential localization of WFs to construct a potentially exact representation of an operator in real space such that any interpolation back to reciprocal space is exact as well. The procedure is also systematic, as WFs are guaranteed to exist and the convergence is exponential with the linear sampling density (Brouder *et al.*, 2007; Panati, 2007; Panati and Pisante, 2013). Naturally, prefactors and coefficients will depend on electronic-structure properties such as the band gap and on the specific operator under consideration.

2. Geometry and topology

WFs have several profound connections with quantum-geometrical and topological aspects of the electronic structure (Vanderbilt, 2018); some of these are discussed in Secs. III.E and III.F. In the following we refer to topological properties as a subset of geometrical properties that are quantized and hence represented by integer topological invariants robust to certain classes of perturbations. A prime example of a geometrical—and in some circumstances also topological—quantity is the electric polarization of periodic solids, which can be calculated in reciprocal space as a Berry phase (Vanderbilt, 2018); see Sec. III.E. Electric polarization can also be equivalently computed by summing over WFs centers in real space (Marzari and Vanderbilt, 1997; Marzari *et al.*, 2012; Vanderbilt, 2018), which provides a more intuitive formulation of the modern theory of polarization (Resta, 1992, 1994; King-Smith and Vanderbilt, 1993; Vanderbilt, 2018) and restores some justification to the classical Clausius-Mossotti viewpoint (Mossotti, 1850; Clausius, 1879). While electronic-structure geometry in reciprocal space speaks the language of differential geometry (curvatures, parallel transport, smoothness of manifolds, etc.), WFs allow the same quantities to be expressed in terms of the matrix elements of the Hamiltonian and position operator $\hat{\mathbf{r}}$. The reciprocal-space smoothness, which is measured by the quantum-geometric tensor (Provost and Vallee, 1980), can be equivalently analyzed in real space by measuring the degree of WF localization.

To some extent the connection between WFs and topological invariants is even stronger, as the former provide not only powerful approaches to calculate invariants for real materials (see Sec. III.F for a discussion) but also a fundamental understanding of topological phases. In fact, topological insulators are essentially systems that cannot be connected adiabatically to atomic insulators; hence, it is impossible to truly represent their ground state with WFs (Thonhauser and Vanderbilt, 2006; Vanderbilt, 2018). In reciprocal space nontrivial topological invariants translate into unavoidable obstructions to choosing a smooth gauge over the BZ (Bernevig and Hughes, 2013; Vanderbilt, 2018). The fundamental connection between nontrivial topology of electronic bands and the corresponding absence of a Wannier representation has been generalized and made systematic in the context of elementary band representation (Zak, 1982; Michel and Zak, 1999), which has led to the so-called topological quantum chemistry (Bradlyn *et al.*, 2017; Vergniory *et al.*, 2017; Cano *et al.*, 2018) [see also related efforts on symmetry-based indicators provided by Kruthoff *et al.* (2017), Po, Vishwanath, and Watanabe (2017), Khalaf *et al.* (2018), and Song *et al.* (2018)] and has allowed materials databases to be screened and nontrivial materials of various classes to be identified (Tang *et al.*, 2019; Vergniory *et al.*, 2019; Zhang *et al.*, 2019; Wieder *et al.*, 2022).

3. Advanced electronic-structure methods

DFT simulations of periodic solids can be conveniently (but definitely not necessarily) performed by adopting a plane-wave basis set in conjunction with smooth pseudopotentials that reproduce the interaction between valence electrons and nuclei plus core electrons (Martin, 2020). The resulting KS eigenstates are also not particularly localized functions, and DFT is invariant under unitary rotations of the occupied electronic states. However, several electronic-structure methods, aiming at improving or complementing the capabilities of DFT, fundamentally require to be formulated in terms of localized orbitals; see Sec. III.H. In addition, several of these beyond-DFT methods are not deployed directly on the crystal structure but instead operate more as corrections to starting DFT calculations. In addition, beyond-DFT methods can be rather computationally intensive, and it is common practice to apply them only on a subset of bands extracted from the entire manifold. In this context WFs provide a robust way to bridge DFT with advanced electronic-structure methods by allowing one to systematically construct orthogonal localized states that represent the manifold of interest. WFs are first constructed on the KS-DFT solution and then fed into beyond-DFT methods; a technical overview of how this is carried out in practice is the subject of Sec. III.H.

C. Wannier functions for the practitioner

1. The spread functional in reciprocal space

The Blount identities (Blount, 1962) provide the matrix elements of the position operator between WFs and prefigure the link between macroscopic properties and integrals (Berry phases) of Berry connections (King-Smith and Vanderbilt, 1993),

$$\langle \mathbf{R}\, i|\mathbf{r}|\mathbf{0}\, j\rangle = i\frac{V_{\mathrm{cell}}}{(2\pi)^3}\int d\mathbf{k}\; e^{i\mathbf{k}\cdot\mathbf{R}}\langle u_{i\mathbf{k}}|\boldsymbol{\nabla}_{\mathbf{k}}|u_{j\mathbf{k}}\rangle \qquad (10)$$

and

$$\langle \mathbf{R}i|r^2|\mathbf{0}j\rangle = -\frac{V_{\text{cell}}}{(2\pi)^3}\int d\mathbf{k}\, e^{i\mathbf{k}\cdot\mathbf{R}}\langle u_{i\mathbf{k}}|\nabla^2_{\mathbf{k}}|u_{j\mathbf{k}}\rangle. \quad (11)$$

It is through these identities that one can recast the spread functional Ω using reciprocal-space expressions, where the gradients and higher derivatives are obtained from finite differences. The building blocks for these finite-difference expressions are the overlap matrices

$$M_{ij}^{(\mathbf{k},\mathbf{b})} = \langle u_{i\mathbf{k}}|u_{j\mathbf{k}+\mathbf{b}}\rangle \quad (12)$$

between cell-periodic Bloch eigenstates $|u_{n\mathbf{k}}\rangle$ at neighboring points on a regular grid in the BZ (the $\mathbf{b}$ vectors connect one k point to its neighbors on a regular discrete grid). In the limit of dense meshes the $\mathbf{b}$ vectors tend to zero and the gradient in $\mathbf{k}$ is recovered. This finite-difference construction remains valid even in the case of Γ-only sampling (such as for molecular systems treated with PBCs or when considering large supercells), where the neighboring k points are given by the primitive reciprocal lattice vectors $\mathbf{G}$, with the Bloch orbitals differing only by phase factors $\exp(i\mathbf{G}\cdot\mathbf{r})$. We note that the gradient in $\mathbf{k}$ of a function $f(\mathbf{k})$ can be written as

$$\nabla f(\mathbf{k}) = \sum_{\mathbf{b}} w_b \mathbf{b}[f(\mathbf{k}+\mathbf{b}) - f(\mathbf{k})] + \mathcal{O}(b^2) \quad (13)$$

using stars ("shells") of neighboring k points where each shell has a weight w_b; see Marzari and Vanderbilt (1997) and Mostofi *et al.* (2008) for detailed descriptions. For a linear function $f(\mathbf{k}) = f_0 + \mathbf{g}\cdot\mathbf{k}$, one can verify that the exact result $\nabla_\alpha f(\mathbf{k}) = g_\alpha$ is recovered. In the simple case of cubic Bravais lattices, the first shell of reciprocal-space nearest neighbors (6, 8, or 12 for Bravais lattices in direct space that are simple cubic, fcc, or bcc) is sufficient. The general case where several shells need to be chosen automatically was detailed by Mostofi *et al.* (2008). While the procedure is automated, for unusual cases such as elongated cells, it might be convenient to manually find the most symmetric choice of shells (Posternak *et al.*, 2002). With this definition the diagonal matrix elements of the position operator can be evaluated via finite differences as

$$\langle \mathbf{0}i|\mathbf{r}|\mathbf{0}i\rangle = -\frac{1}{N}\sum_{\mathbf{k},\mathbf{b}} w_b \mathbf{b}\,\text{Im}\,\ln M_{ii}^{(\mathbf{k},\mathbf{b})}, \quad (14)$$

where N is the number of k points on the reciprocal-space grid. More complex expressions for the second derivatives and for the entire spread functional can be obtained (Berghold *et al.*, 2000), all of which are equal to the leading order in b. The choices made by Marzari and Vanderbilt (1997) were driven by the need to provide the same value for the localization functional under a transformation that shifts $|\mathbf{R}i\rangle$ via a lattice vector. We also note that when using such a finite-difference formalism, the spread functional converges slowly (polynomially) with reciprocal-space sampling, and hence care must be taken when comparing its actual values in the case of calculations performed with different discrete samplings.

The finite-difference scheme is particularly convenient for constructing MLWFs in a code-agnostic form, as the only input needed from the original first-principles calculation is encoded in the overlap matrices $M_{ij}^{(\mathbf{k},\mathbf{b})}$. Thus, once $M_{ij}^{(\mathbf{k},\mathbf{b})}$ have been calculated, no further interaction is necessary with the electronic-structure code that calculated the ground-state wave functions, making the entire Wannierization procedure a code-independent postprocessing step; see Ferretti *et al.* (2007) for an examination of the extension to ultrasoft pseudopotentials and to the projector-augmented wave method, and Posternak *et al.* (2002), Freimuth *et al.* (2008), and Kune *et al.* (2010) for discussions of the full-potential linearized augmented plane-wave method. In regard to the disentanglement procedure, note that because of energy windows the needed input from the first-principles calculation includes the energy eigenvalues $\varepsilon_{n\mathbf{k}}$ in addition to the overlap matrices (12).

2. Accuracy and convergence

While the main focus of this review is on the powerful applications of WFs, their successful use relies on the Wannierization process being done correctly. In the following we comment on fundamental tests and established procedures to assess and improve the quality of WFs.

Two major convergence parameters control the quality (and the cost) of the Wannierization procedure: the spread minimization and the k-point grid used to obtain the initial Hamiltonian eigenstates (for example, the cell-periodic part of Bloch states if one is working with PBCs). The spread minimization is generally performed with an iterative steepest-descent or conjugate-gradient algorithm until results do not change within a certain tolerance. While the iterative algorithm is generally robust, the minimization can become trapped in local minima. As introduced in Sec. II.A.3, the strategy to avoid that is to select a good starting point: if the initial spread is sufficiently close to the absolute minimum, it is more likely to reach it by following the local gradient. Hence, particular care needs to be paid to select good projection functions to obtain the initial unitary matrix of Eq. (6b), which are then iteratively optimized. In the absence of chemical intuition, a common strategy is to calculate a projected density of states on the pseudoatomic orbitals and identify the orbital character in the energy region of interest: the atomic orbitals that project more on the relevant bands can be used as the initial projection. Note that MLWFs are often not atom centered and atomic orbitals are not always good starting projections, as in the case of the valence bands of monolayer MoS_2 (Gibertini, Pizzi, and Marzari, 2014). In Secs. II.D and III.J, we cover advanced methods to automate the selection of the starting point for the minimization procedure.

The spread functional measures the degree of localization in real space and, to some extent, the efficiency of the interpolation. More localized WFs decay faster in real space; hence, they require a smaller Born–von Kármán (BvK) supercell to include all nonvanishing matrix elements of the Hamiltonian and the other operators, which in turn allows one to adopt coarser k-point grids in the starting electronic-structure simulation that is performed in reciprocal space.

Indeed, the accuracy of band interpolation can be considered a proxy for the quality of the underlying WFs in regard to more than just k-point convergence: especially in the case of entangled bands (see Sec. II.A.2), poor interpolation might signal problems in the disentanglement procedure. In addition, we emphasize that in general the Wannierization procedure is not forced to preserve symmetries (unless dedicated methods designed to do so are employed; see Sec. II.D). Hence, the spurious splitting of symmetry-protected degeneracies in the interpolated band structure might signal convergence problems related to the minimization, to the k-point convergence, or to the choice of projection functions. This holds true not only for crystalline symmetries but also for time-reversal symmetry, which is particularly relevant in noncollinear simulations of nonmagnetic materials in the presence of spin-orbit coupling (for example, topological insulators).

Another indicator of the quality of WFs is the ratio between their imaginary (Im) and real (Re) parts: for isolated bands (and not considering spin-orbit coupling), MLWFs at the global minimum should be real functions (Marzari and Vanderbilt, 1997). Note that the calculation of the Im or Re part, and anything related to WFs themselves and their visualization, requires one to have access to the full Bloch orbitals, not just the overlap matrices. We emphasize that different quantities derived from WFs (such as the WF spread and centers as well as the unitary matrices $\tilde{V}_{\mathbf{k}}$ and $U_{\mathbf{k}}$) generally converge with different speeds, depending on the specific formulation adopted (Stengel and Spaldin, 2006).

Finally, we remark that many of the complications related to producing WFs for periodic solids are related to construction of a smooth gauge across the BZ. Hence, supercell Wannierizations with Γ-only sampling are typically more straightforward and less prone to be trapped in local minima. The challenge there is more on algorithmic efficiency due to the large size of the systems involved; a number of Γ-only dedicated methods have been developed (Silvestrelli, 1999; Gygi, Fattebert, and Schwegler, 2003; Stubbs, Watson, and Lu, 2021).

D. Advanced minimization methods and beyond maximally localized Wannier functions

As discussed in Sec. II, there is in principle large freedom in choosing the recipe to obtain well-localized WFs. One can replace the MV spread functional with not only other cost functions but also different minimization procedures, and their starting points can be chosen, hence affecting the resulting WFs and their localization properties. Over the years a number of methods have been developed to address all of the different aspects of the Wannierization procedure. We emphasize that, for many of these methods, the initial guess already provides well-localized WFs, so an iterative minimization can in principle be avoided. The unitary matrices $U_{\mathbf{k}}$ of these "projection-only" WFs are set directly by the initial projection functions; see Sec. II.A.3. While this choice cannot guarantee optimal localization properties, it has the advantage of enforcing some degree of symmetry induced by the choice of atomic orbitals used as projection functions. However, in all of these cases it is possible—and in some cases even recommended—to minimize the MV spread or some other functional as a final step.

The prime decision deals with the functional that is to be minimized in order to determine the unitary matrices of Eq. (6). The most popular choice is the MV MLWF procedure (Marzari and Vanderbilt, 1997) for composite bands (see Sec. II.A.1) and the SMV disentanglement scheme for entangled bands (Souza, Marzari, and Vanderbilt, 2001); see Sec. II.A.2. The minimization of the spread functional leads to well-localized WFs, hence reducing the size of the BvK supercell needed to represent operators (such as the Hamiltonian) in a WF basis. While MLWFs and disentanglement represent the most convenient choice in most applications, substantial work has been done to augment the MLWF scheme or develop alternatives that satisfy the needs of specific applications.

The MLWF iterative algorithm leads to localized WFs in real space but is not guaranteed to yield orbitals that preserve desirable crystal symmetries. This is only partially relieved using symmetric initial projections, as typically obtained with a proper selection of atomiclike orbitals. Symmetry-preserving WFs are appealing for providing the correct orbital or site symmetries for many-body approaches like dynamical mean-field theory (DMFT). Hence, it is not surprising that several non-MLWF procedures directly or indirectly include crystal symmetries in the functional to minimize. In the symmetry-adapted Wannier-function (SAWF) method (Sakuma, 2013), symmetric WFs are obtained through additional constraints on the unitary matrices $U_{\mathbf{k}}$, which are based on symmetry operations of the site-symmetry group. The SAWF method is fully compatible with the maximal-localization procedure and the SMV disentanglement [and has also recently been extended to the case where a frozen window is used (Koretsune, 2023)], although the additional constraints imply a possibly larger total spread, even if some individual WFs can actually be more localized than in the MLWF procedure. Currently, the implementation of the SAWF method in the `Wannier90` code (see Sec. III.A for more about software) is interfaced with the `Quantum ESPRESSO` distribution and, once the site positions and the orbital symmetries of the SAWFs are chosen (through the initial projection functions), the site-symmetry group can be automatically computed by the interface code. If needed, the site-symmetry group can also be manually specified by the user to construct SAWFs with target symmetries.

While the SAWF method provides a rigorous way to include symmetries in the maximal-localization procedure, it requires some prior knowledge of the electronic structure of the material under study. An alternative and simpler approach is to construct selectively localized Wannier functions (SLWFs), in which the MLWF procedure is applied to only a subset of the entire WFs considered (Wang *et al.*, 2014). In addition, some WF centers can be constrained (SLWF + C) to specific positions by adding a quadratic penalty term to the spread functional. While the SLWF + C approach does not enforce symmetries, it has been observed that the resulting WFs typically exhibit the site symmetries corresponding to the constrained centers (Wang *et al.*, 2014). The SLWF + C approach can be used in the case of entangled bands, where the SMV disentanglement step is performed as usual, while

the selective localization and constrained centers are applied only to the final Wannierization step. A more in-depth review of the SAWF and SLWF + C methods, including their implementation and usage in `Wannier90`, was given by Pizzi *et al.* (2020). Dedicated tools for symmetry analysis and symmetrization of the real-space WF Hamiltonian are available (Zhi *et al.*, 2022).

The localization and possibly the symmetry can crucially depend on the number of WFs considered in a given energy range. The so-called partly occupied Wannier functions (POWFs) (Thygesen, Hansen, and Jacobsen, 2005) formalize this observation by including the relevant unoccupied states which lead to the minimal spread functional, essentially implementing a bonding-antibonding closing procedure. POWFs can have a high degree of symmetry, while the bonding-antibonding criterion has been shown to correspond to the condition of maximal average localization (Thygesen, Hansen, and Jacobsen, 2005). Notably, in the POWF scheme the total spread functional $\Omega = \Omega_I + \tilde{\Omega}$ is minimized at once. This is at variance with the SMV scheme, where first the gauge-invariant part Ω_I is minimized through the disentanglement step—and only after the gauge-dependent part $\tilde{\Omega}$ is minimized through the usual MV scheme. The iterative minimization of the total spread Ω was further developed by Damle, Levitt, and Lin (2019). They reformulated the Wannierization, which is a constrained nonlinear optimization problem, as unconstrained optimization on matrix manifolds, where the SMV disentanglement procedure can be interpreted as a splitting method that represents an approximate solution.

We stress that even if minimization of the full spread functional Ω guarantees the highest degree of overall localization, several of the methods discussed here can actually produce WFs such that a subset of them might individually be more localized than their maximally localized counterparts. Along those lines, Fontana *et al.* (2021) developed spread-balanced WFs in which they added a penalty term to the spread functional that was proportional to the variance of the spread distribution among all WFs of the system. This scheme could be less prone to produce solutions with one or several poorly localized WFs, at the price of an increased total spread for the entire set. The addition of terms to the spread functional can also be used to preserve some degree of locality in energy, as in the case of mixed Wannier-Bloch functions (Giustino and Pasquarello, 2006) and dually localized Wannier functions (Mahler *et al.*, 2022). These approaches are based on a generalized spread functional (Gygi, Fattebert, and Schwegler, 2003) designed to carry both spatial localization (Wannier character) and limited spectral broadening (Bloch character) by minimizing a functional that contains not only a spatial variance (as with MLWFs) but also an energy variance.

Once a choice for the functional to be minimized is made (the total spread as in the MLWF scheme, or any other choice), there is still a lot of flexibility on the choice of algorithm to perform the minimization. One first needs to define a starting guess for the unitary matrices $U_{\mathbf{k}}$, which is customarily obtained by specifying a set of localized projection functions through the projection method introduced in Sec. II.A.3. While for composite bands a set of randomly centered spherically symmetric Gaussian orbitals might work, in general more sophisticated choices are required. Typically, atomic orbitals are used as projection functions, such as s, p, and d orbitals, as well as hybrid orbitals (such as sp^3), which are often centered either on atoms or along bond directions. As discussed in Sec. II.C.2, the choice of the right atomic orbitals is typically based on chemical intuition and can be partly informed by inspecting the projected density of states in the energy region of interest. Nevertheless, the choice of the right projection orbitals—i.e., those providing a good starting point for a successful minimization of the target functional—can often be a nontrivial task, especially in the context of automated high-throughput materials screening and, more generally, when one wants to study a novel material never before investigated (especially in the case of unfamiliar orbital composition). Hence, in the past decade substantial effort has been targeted at developing automated algorithms that remove the need for users to define appropriate initial projections. A first approach in this direction is the optimized projection function (OPF) method for composite bands (Mustafa *et al.*, 2015). In the OPF approach a larger set of functions that overspan the space of MLWFs is built and used as a starting point. While in plane-wave codes the OPF approach (Mustafa *et al.*, 2015) still needs the user to provide a list of initial projections, for instance, atomiclike local orbitals (LOs), *ab initio* codes operating with localized (or mixed plane-wave–localized) basis sets can leverage the built-in localized orbitals. For instance, the full-potential linearized augmented-plane-wave (LAPW) method can be extended by adding the so-called LOs, which are atomiclike and highly localized and can be employed in the construction of WFs. Tillack, Gulans, and Draxl (2020) combined the SMV disentanglement with the OPF method (Mustafa *et al.*, 2015) to construct initial guesses for MLWFs from a set of LOs in an automated way. Finally, another set of parameters that require tuning in the standard SMV disentanglement scheme are the inner and outer energy windows. Gresch *et al.* (2018) targeted the removal of the need for manual input by focusing on the automated optimization of both windows.

On the algorithmic side, in the quest for fully automating the generation of localized WFs, various general and practical approaches have been proposed that target the construction of well-localized WFs using algorithms that are often noniterative. This not only makes them more automatable but also provides a good starting point for a final Wannierization, if required: the SCDM approach (Damle, Lin, and Ying, 2015, 2017; Damle and Lin, 2018), the continuous Bloch gauges (Cancès *et al.*, 2017; Gontier, Levitt, and Siraj-dine, 2019), and the projectability disentanglement and manifold remixing approaches (Qiao, Pizzi, and Marzari, 2023a, 2023b).

SCDM is based on QR factorization with column pivoting (QRCP) of the reduced single-particle density matrix. The approach either can be used to produce well-localized WFs without performing an iterative minimization or can be considered a linear-algebra method to identify a good starting point for a MLWF procedure. The SCDM method is implemented (Vitale *et al.*, 2020) in the interface code to `Quantum ESPRESSO`, with an algorithm for the QRCP that works on a smaller matrix instead of the full density matrix (Damle, Lin,

and Ying, 2015, 2017; Damle and Lin, 2018). For a set of composite bands, SCDM is parameter-free. A comprehensive study on 81 insulators (Vitale *et al.*, 2020) showed how the MLWF procedure applied to SCDM initial projections (SCDM + MLWF) improves the interpolation accuracy and localization of the resulting WFs, although SCDM-only WFs already perform well, both in terms of accuracy of band-structure interpolation and in terms of localization. In the case of entangled bands, SCDM requires one to specify an energy-window function, its center and width, and the number of WFs to consider. Vitale *et al.* (2020) introduced a recipe to automatically select those parameters (see Sec. III.J) that was tested on 200 bulk materials. Unlike in the case of isolated groups of bands, for entangled bands the SCDM + MLWF method greatly improved the localization of the WFs with respect to SCDM-only WFs. Notably, however, the reduced spread induced by the MV procedure might result in lower band-interpolation accuracy. Although the SCDM projections could be used together with the SMV disentanglement scheme, this more complex procedure does not provide a systematic gain in accuracy such that a SCDM-only or SCDM + MLWF approach (with MV minimization for $\tilde{\Omega}$) would be recommended (Vitale *et al.*, 2020). In addition, we note that SCDM requires real-space wave functions as input, and therefore has a higher computational and memory cost with respect to other methods discussed later in this section, which are implemented in reciprocal space.

Another noniterative approach for composite bands is based on ensuring a continuous Bloch gauge over the entire BZ (Cancès *et al.*, 2017; Gontier, Levitt, and Siraj-dine, 2019), resulting in good localization properties of the WFs and not requiring any chemical intuition for their construction. The main idea is that one can construct a sequence of gauge matrices that not only are continuous across the BZ but also satisfy its periodicity at the BZ edges. This is achieved by first adopting parallel transport for the gauge matrix, starting with a chosen k point (usually the Γ point) and propagating along a line (such as the k_x line). This enables the periodicity to be fixed at the two end points of the line while preserving the continuity. Then, for each k point on the line, parallel transport is applied to each of the gauge matrices along an orthogonal direction (for example, in the k_y direction), and all gauge matrices are fixed again at the end points to ensure periodicity of the 2D plane. Finally, for each k point on the 2D plane, one can apply a similar procedure to construct gauge matrices along the third direction, therefore obtaining a global continuous gauge across the full BZ. Often the resulting gauge is continuous but not smooth enough: a subsequent conventional MV iterative minimization can improve the localization and reach the MLWF gauge. Such an algorithm is able to construct MLWFs for difficult cases such as $\mathbb{Z}_2$ topological insulators (Gontier, Levitt, and Siraj-dine, 2019).

Finally, a robust approach has emerged in the form of projectability disentanglement (Qiao, Pizzi, and Marzari, 2023b), where the inner and outer energy windows are replaced by projectability thresholds. For each state $|u_{n\mathbf{k}}\rangle$ a projectability (Agapito *et al.*, 2013; Vitale *et al.*, 2020) onto localized atomic orbitals (typically, those coming from the pseudopotentials) is calculated. Then states that have high projectability are retained identically (exactly as done for states inside the inner frozen window in the SMV method), states that have low projectability are discarded altogether since they do not provide useful contributions to MLWFs, and states that span the intermediate projectability values are treated with the standard SMV disentanglement. This approach leads to atomiclike projectability-disentangled Wannier functions (PDWFs) spanning both occupied and unoccupied states corresponding to Bloch sums of bonding-antibonding combinations of atomic orbitals.

These PDWFs can in turn be remixed into linear combinations that aim to describe target submanifolds, for example, the valence states only, the conduction states only, or certain groups of bands that are separated in energy from the rest. This may be beneficial for finding optimal target states for beyond-DFT methods; see Sec. III.H.

This remixing is particularly valuable for Koopmans functionals (see Sec. III.H.2), which require separate sets of MLWFs for the valence and conduction manifolds, or for transport calculations. For this purpose the manifold-remixed Wannier functions (MRWFs) (Qiao, Pizzi, and Marzari, 2023a) are obtained by starting with the PDWFs spanning the entire manifold (valence plus conduction), which is then split by rotating the gauge matrices into a block-diagonal structure across all the k points while simultaneously maintaining the gauge smoothness for each block. This is achieved through a combination of automated Wannierization of the entire manifold, diagonalization of the Wannier Hamiltonian, parallel transport, and maximal localization. The automated Wannierization of the entire manifold can be obtained using the PDWF method; the Hamiltonian diagonalization splits the manifold into desired submanifolds (for example, two for valence and conduction, respectively); the parallel transport fixes the gauge randomness to construct two sets of localized WFs; and the final maximal localization smoothens the gauge, leading to subsets of MLWFs for the respective submanifolds. Qiao, Pizzi, and Marzari (2023a) demonstrated that, when combined with PDWFs, the MRWF method can be fully automated and can also be extended to other types of band manifolds gapped in energy, such as the single top valence band of MoS_2 or the $3d$ and t_{2g}/e_g submanifolds of $SrVO_3$. For high-throughput results of PDWF and MRWF, see Sec. III.J.

III. THE WANNIER ECOSYSTEM: THEORY AND SOFTWARE PACKAGES

A. Development of widely available Wannier engines

The MV and SMV methods described by Marzari and Vanderbilt (1997) and Souza, Marzari, and Vanderbilt (2001) were originally implemented in `Fortran 77`. The code would compute the overlaps in Eq. (12) and the projection of the periodic part of the Bloch orbitals onto trial localized states by reading the former evaluated on a regular k-point grid using a DFT code—originally by an early version of `CASTEP` (Marzari, Vanderbilt, and Payne, 1997; Clark *et al.*, 2005). To provide a more general model, driven by the need to interface with a DFT code based on the LAPW method (Posternak *et al.*, 2002), the choice was made to keep the calculation of all

the scalar products involving Bloch orbitals needed by the Wannier code within the electronic-structure code of choice, typically as a postprocessing step. Well-defined protocols were established to exchange this information writing (reading) files to (from) disk and the format of those files was fully documented. The resulting Wannier77 code was released under a GNU General Public License (GPL) version 2 in March 2004.

In 2005 Arash A. Mostofi and Jonathan R. Yates, then working in the groups of Nicola Marzari and Ivo Souza, respectively, rewrote the routines using modern modular Fortran, relying on their experience of software development gained from working on the ONETEP (Prentice *et al.*, 2020) and CASTEP (Clark *et al.*, 2005) DFT programs. The resulting program Wannier90 (Mostofi *et al.*, 2008) was released under a GPL license in April 2006. Following the early layout in the Wannier77 code, Wannier90 was designed to be easily interfaced to any electronic-structure code, irrespective of its underlying basis set. The first release of Wannier90 came with extensive documentation, tutorials, and two validation tests. Development used Concurrent Versions System (CVS) as a version control system. Giovanni Pizzi joined the development effort in 2012, and a new parallel postprocessing code (postw90) was developed and released in Wannier90 version 2 in October 2013 (Mostofi *et al.*, 2014).

While the development of Wannier90 as an open-source interoperable code was innovative in 2006, by 2016 it was clear that the development tools being used did not make use of what was then considered best practice. For example, having only a few developers with access to the main repository presented a barrier to adding new functionality to the program. A decision was made to move to a community development model, and the Wannier90 repository was migrated to GitHub with the adoption of a "fork and pull request" approach. This new model was launched with a community developer workshop held in San Sebastián, Spain, in September of 2016. This event is recognizable in Fig. 5, which shows the number of commits to the code repository over time, with a large number of commits contributed during (or immediately after) the 2016 event. Moreover, once the code made its transition to a community development model, the rate of commits significantly increased, as did the number of individual contributors (more than 35 different people had contributed code, tests, or documentation via commits by November 2024). Essential to this change was the development of an extensive suite of tests that run automatically to validate each pull request. In 2019 Wannier90 version 3 was released, including all community contributions to the code (Pizzi *et al.*, 2020).

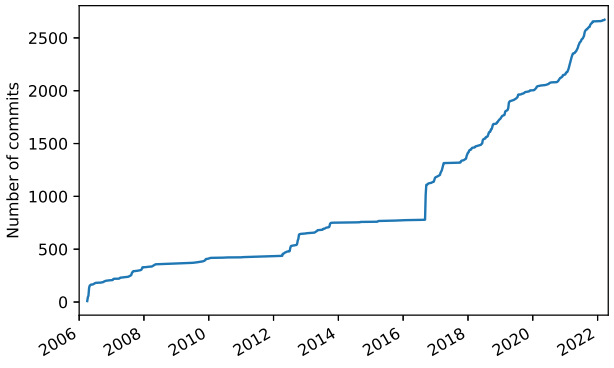

FIG. 5. Total number of commits over time for the Wannier90 repository (CVS until August 2016, then transferred to Git and hosted on GitHub). Note the significant increase during and immediately after the community developer workshop in September 2016.

In addition to Wannier90 there are a few electronic-structure software packages that currently implement internal functionality for computing WFs in periodic systems. These include GPAW (Enkovaara *et al.*, 2010), Qbox (Gygi, 2008), CP2K (Kühne *et al.*, 2020), exciting (Tillack, Gulans, and Draxl, 2020), OpenMX (Weng, Ozaki, and Terakura, 2009), RESPACK (Nakamura *et al.*, 2021), and CRYSTAL (Zicovich-Wilson, Dovesi, and Saunders, 2001). However, in this review we use the term *Wannier engines* to describe software packages that both generate WFs and are designed to be used interoperably with other software packages: for example, with the electronic-structure codes for solving the electronic ground state, used as input to a Wannier engine, and with postprocessing codes that use the WFs from a Wannier engine to calculate advanced electronic properties. Wannier90 is an example of a Wannier engine, but it is not the only readily available one—another notable example is the Atomic Simulation Environment (ASE) (Larsen *et al.*, 2017), which also implements routines based on the minimization of the quadratic spread of the WFs but uses a different approach (Thygesen, Hansen, and Jacobsen, 2005; Fontana *et al.*, 2021) from the previously described one; see also Sec. II.D. In addition, the new Wannier.jl package (Qiao, Pizzi, and Marzari, 2023d) implements several Wannierization algorithms using manifold optimization techniques and brings the methodology of WFs to the Julia community (Bezanson *et al.*, 2017). In this review we focus on those codes that interface to the Wannier90 code. Nevertheless, we note that the other Wannier engines have often adopted the same file formats first defined by Wannier77 and Wannier90 (see the discussion in Sec. III.B), thus being fully compatible with the ecosystem.

B. The concept of a Wannier-function software ecosystem

To discuss the modular approach that has catalyzed the formation of a Wannier-function software ecosystem, we start with a general overview of modularization strategies in software programs. We also mention some related efforts on code modularization, discussing the aspects that apply to the Wannier ecosystem. Complex software can adopt a variety of architectural design approaches, often differing substantially in the level of modularity (or the lack thereof) of their components. Historically, most computer programs started as monolithic applications: self-contained and independent codes made of tightly coupled functions. This is a natural choice when writing new software from scratch, and it reduces the installation burden for users, who do not need to deal with the management of many dependencies. Over time, however, features and postprocessing tools tend to get added, making the code base large and complex. This results in serious challenges for development and maintenance, which become

critical when the code needs to be adapted and optimized for newer hardware architectures. Furthermore, this leads to reimplementations of common routines in each code, which could instead be written and optimized only once and then used as a library. The library approach is already common in the electronic-structure community for linear-algebra and diagonalization routines, where the code calls functions via standard interfaces defined by the `BLAS` (Blackford *et al.*, 2002) and `LAPACK` libraries (Anderson *et al.*, 1999), and the executables are linked to performance-optimized versions on high-performance computing clusters. While a similar approach is often used for other low-level routines, such as fast-Fourier-transform (FFT) computation (Frigo and Johnson, 2005) or to support file formats such as `NetCDF` (Rew and Davis, 1990) or `HDF5` (HDF Group, 2023), it was until recently far less common for higher-level materials-science-oriented routines.

To address the challenges of monolithic codes, many electronic-structure codes are being redesigned or rewritten using a more modular approach, where core modules are—when possible—generalized and separated into a library of reusable routines, then called by higher-level functions to execute complex tasks. Some of these codes have evolved into distributions, i.e., a set of relatively independent but interoperable executables reusing common core routines. However, even with this approach, the different modules can often operate only within the distribution, and the development of all modules needs to constantly be in sync.

Ultimate interoperability is obtained when code (such as core routines or full functionality) is reused by different independent software distributions that are maintained by nonoverlapping developer groups. A crucial challenge to enable such a level of interoperability is to design a clear application programming interface (API) defining which data need to be transferred between codes, and in which format. This requires discussions and coordination, which can be catalyzed via targeted coordination efforts.

We stress that most of the challenges related to code modularization and interoperability are not specific to materials simulations and have been discussed since the early days of scientific computing (Roberts, 1969). In the field of electronic structure, an example of note is the CECAM Electronic Structure Library project (CECAM ESL Collaboration, 2023). At an even higher level, one can address code interoperability by defining common interfaces (for example, input-output schemes) for workflows computing a quantity of interest, independent of the underlying simulation code, such as the common workflow interface of Huber *et al.* (2021) to perform crystal-structure relaxation and to compute equations of state. The workflow only requires as input, in a common format, the crystal structure and a few basic input parameters, and is then interfaced with 11 different DFT codes to run the actual simulations. Such universal interfaces make workflows accessible to a broader audience and codes fully interoperable, allowing researchers to switch between them without the need to learn from scratch the details of each one. In addition, they can be seamlessly applied to perform cross-code verification studies (Bosoni *et al.*, 2024).

When codes have to exchange data, the interfaces between them can be actual code APIs (for example, in `C` or `Fortran`), where the library is directly compiled and linked with the main code, but also simply files in a well-documented format, written by the first application and read by the second one; see the discussion of this approach in Sec. III.I. The actual choice depends on the interdependency between the algorithmic steps and on performance considerations. The use of files is typically favored when the corresponding simulation workflows imply a sequential execution of codes rather than interconnected loops between them, when the exchanged data are small (up to a few gigabytes) and the individual steps are computationally demanding, such that I/O overhead is only a small fraction of the total execution time. [In a few advanced cases, other interfaces such as network sockets have been used to keep the applications decoupled while still reducing the I/O overhead for simulations that are not too computationally demanding (Kapil *et al.*, 2019).] In addition, when intermediate results are written to files, the steps do not need to be combined in the same run but can instead be executed at different times (for example, days later) or by different researchers.

In this context WFs represent a noteworthy and elegant method to decouple the *ab initio* simulation of the electronic structure from the calculation of the physical properties. This is possible thanks to two core aspects of WFs. First, WFs are independent of the basis set used in the first-principles electronic-structure code: the MLWF algorithm requires the sole knowledge of a handful of vectors and matrices, such as the overlap matrices on a coarse grid of k points. Wave functions, which are typically stored in large files, are not required during Wannierization and are used optionally in only a few postprocessing steps, such as when representing the WFs on a real-space grid. Second, many physical quantities can be obtained efficiently once a WF basis is constructed, with the knowledge of relevant operators represented as small matrices directly in the Wannier basis, such as the Hamiltonian or the position operator. Indeed, while extended basis sets such as plane waves are particularly convenient for obtaining charge densities and wave functions of periodic systems, reciprocal-space integrals can be more efficiently calculated using a Fourier-interpolated basis set originating from a compact maximally localized representation in real space. From a computer-science perspective, these two aspects of the Wannierization process make it an effective data-compression encoding that avoids the need to transfer large wave functions between the *ab initio* codes and the property calculators while retaining an equivalent level of accuracy.

Thanks to the first aspect, i.e., basis-set independence, the `Wannier` code (Marzari and Vanderbilt, 1997) evolved from being a stand-alone code focused on the minimization procedure to one with a well-defined format for the input data (overlap and projection matrices), which also defined and documented the corresponding files (such as the overlap matrices in `.mmn` format and the projection matrices in `.amn` format). The calculation of the latter was delegated to specific interfaces implemented within the corresponding first-principles packages (Posternak *et al.*, 2002). This design persisted in the `Wannier90` code (Mostofi *et al.*, 2008; Pizzi *et al.*, 2020), and as a result the `Wannier90` engine can now be interfaced with virtually any electronic-structure code,

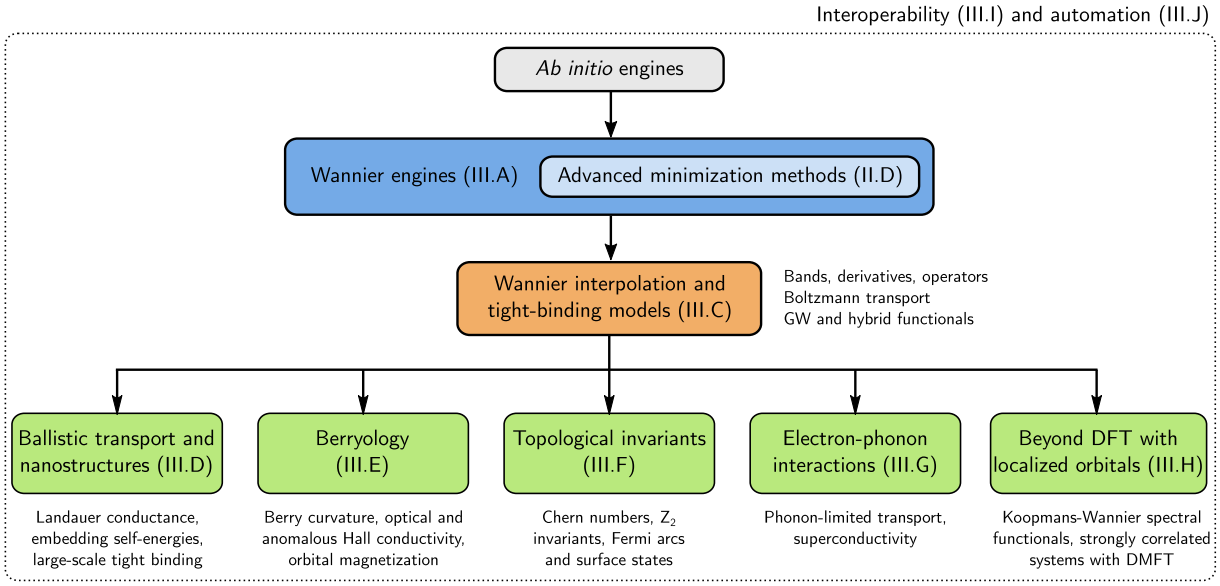

FIG. 6. Overall schematics of how different codes in the ecosystem interact that also serves as a type of table of contents for this review, where sections describing the relevant blocks are indicated here. At the top the *ab initio* engines (first row) generate the data that are transferred to a Wannier engine (second row) that might also implement the advanced methods discussed in Sec. II.D. Once WFs are obtained, they are typically used to generate a TB model and perform interpolation of the Hamiltonian and other operators (third row). Such interpolated quantities are used for a number of different applications; the ones that are discussed in more detail in this review are set in the green blocks (fourth row). As schematically indicated by the outer dotted rectangle, all the codes forming the Wannier ecosystem may be automated with workflow tools, which also coordinate data transfer between them.

as discussed in Sec. III.A, with interfaces currently available for many widespread codes, including `ABINIT` (Gonze *et al.*, 2020), `BigDFT` (Ratcliff *et al.*, 2020), `Elk` (Elk Collaboration, 2023), `FLEUR` (Wortmann *et al.*, 2023), `GPAW` (Enkovaara *et al.*, 2010), `Octopus` (Tancogne-Dejean *et al.*, 2020), `OpenMX` (Ozaki and Kino, 2005), `PySCF` (Sun *et al.*, 2018, 2020), `Quantum ESPRESSO` (Giannozzi *et al.*, 2009, 2017), `SIESTA` (Soler *et al.*, 2002), `VASP` (Kresse and Joubert, 1999), and `WIEN2k` (Blaha *et al.*, 2020).

Because of the second aspect, i.e., the possibility of efficiently obtaining many physical quantities in the Wannier basis, `Wannier90` started to include a large number of efficient postprocessing utilities for materials properties, ranging from simple band-structure interpolation to more complex properties such as the ordinary and anomalous Hall conductivities, Seebeck coefficients, orbital magnetization, and many more (Pizzi *et al.*, 2020). However, in the past decade the community has spontaneously moved toward a decentralized software ecosystem (as opposed to a centralized, albeit modular, Wannier distribution), where different packages interact through APIs and a common data format. The decentralized model was again facilitated by a clear and documented interface to generate data as input for the next steps (for example, the `_tb.dat` file containing the full TB model: WF centers, on-site energies, and hopping energies). The community has been rapidly growing, and several independent packages exploiting MLWFs now exist, targeting diverse properties such as TB models (see Sec. III.C), ballistic transport (see Sec. III.D), Berry-phase-related properties (see Sec. III.E), topological invariants (see Sec. III.F), electron-phonon coupling (see Sec. III.G), beyond-DFT methods (see Sec. III.H), high-throughput calculations (see Sec. III.J), etc.

This review describes such a community of symbiotic packages, forming a research and software ecosystem built upon the concept of MLWFs. We illustrate this schematically in Fig. 6. To make the codes of the ecosystem as easy to find as possible, we also started in 2024 the online Wannier Software Ecosystem Registry.[1] This registry lists software packages that form the ecosystem, and as of November 2024 it already included 53 entries. The repository provides key information including a short description, a domain tag (such as *ab initio* engines, tight binding, and Berryology and topology), and links to the code home page, documentation, and source code (if available). The registry is dynamic: developers and users can add new entries or modify existing ones by submitting a pull request through the corresponding GitHub repository,[2] which also includes detailed instructions for contribution.

C. Wannier-interpolation and tight-binding models

A common application of WFs is to evaluate various k-space quantities and BZ integrals by Wannier interpolation. This name has come to refer to a type of Slater-Koster interpolation where the required on-site and hopping integrals are explicitly calculated in the WF basis (Souza, Marzari, and Vanderbilt, 2001; Calzolari *et al.*, 2004; Lee, Nardelli, and

[1]The Wannier Software Ecosystem Registry is available at https://wannier-developers.github.io/wannier-ecosystem-registry/.

[2]The GitHub repository of the Wannier Software Ecosystem Registry is available at https://github.com/wannier-developers/wannier-ecosystem-registry.

Marzari, 2005; Yates *et al.*, 2007), as opposed to being treated as fitting parameters as in empirical TB theory. Here we review the basic procedure as it applies to energy bands and other simple quantities, leaving more sophisticated applications to later sections. Before proceeding, we mention that the Wannier-interpolation scheme has been adapted to work with nonorthogonal localized orbitals instead of (orthogonal) WFs (Buongiorno Nardelli *et al.*, 2018; Lee, Lee *et al.*, 2018; Wang, Zhao *et al.*, 2019; Jin, Zheng, and He, 2021).

1. Band interpolation

To interpolate the band structure, one needs the matrix elements of the KS Hamiltonian in the WF basis,

$$H^{\mathrm{W}}_{ij}(\mathbf{R}) = \langle \mathbf{0}i|\hat{H}|\mathbf{R}j\rangle, \tag{15}$$

where $H_{ii}(\mathbf{0})$ are on-site energies and the remaining matrix elements are hoppings. One way to evaluate these matrix elements is to start with Eq. (6a) for the WFs in terms of the KS Bloch eigenstates on the *ab initio* k grid. Inserting Eq. (6a) into Eq. (15) gives

$$H^{\mathrm{W}}_{ij}(\mathbf{R}) = \frac{1}{N}\sum_{\mathbf{k}} e^{-i\mathbf{k}\cdot\mathbf{R}} \sum_{n=1}^{\mathcal{J}_{\mathbf{k}}} V^{*}_{\mathbf{k},ni}\varepsilon_{n\mathbf{k}}V_{\mathbf{k},nj}. \tag{16}$$

This procedure is particularly convenient in the framework of the MV and SMV Wannierization schemes, which are formulated as postprocessing steps after a conventional *ab initio* calculation is carried out on a uniform $\{\mathbf{k}\}$ grid. Equation (16) involves only the $V_{\mathbf{k}}$ matrices generated by the Wannier engine starting with the *ab initio* overlap matrices and the energy eigenvalues themselves; see Sec. II.A. An alternative to Eq. (16) is to express the WFs in a real-space basis, for example, localized orbitals or a grid, and then evaluate Eq. (15) directly on that basis.

In view of the localized character of the WFs, $|H^{\mathrm{W}}_{ij}(\mathbf{R})|$ is expected to become negligibly small when the distance $|\mathbf{R}+\boldsymbol{\tau}_j-\boldsymbol{\tau}_i|$ between the centers of the two WFs becomes sufficiently large (here $\boldsymbol{\tau}_j = \langle \mathbf{0}j|\hat{\mathbf{r}}|\mathbf{0}j\rangle$). However, owing to the finite size N of the *ab initio* grid, the WFs obtained from Eq. (6a) are actually periodic over a real-space supercell of volume NV_{cell}. Accordingly, the matrix elements given by Eq. (16) are also supercell periodic, $H^{\mathrm{W}}_{ij}(\mathbf{R}+\mathbf{T}) = H^{\mathrm{W}}_{ij}(\mathbf{R})$, for any supercell lattice vector $\mathbf{T}$. To minimize spurious effects associated with this artificial periodicity, one should truncate the hopping matrix by setting $H^{\mathrm{W}}_{ij}(\mathbf{R}) = 0$ whenever the vector $\mathbf{R}+\mathbf{T}+\boldsymbol{\tau}_j$ lies outside the Wigner-Seitz (WS) supercell centered at the origin. Provided that this supercell is sufficiently large to ensure negligible overlap between a WF and its periodic images, the truncation error will be insignificant. This means that in practice one can achieve well-converged numerical results with a relatively coarse *ab initio* grid. Note, however, that the matrix elements do not decay exactly to zero for finite-size WS supercells. Therefore, when multiple $\mathbf{R}$ vectors lie on the boundary of the WS supercell and are connected by a supercell vector $\mathbf{T}$, it is better to consider all of the equivalent vectors with appropriate weights, rather than picking only one of them, which would introduce spurious symmetry breaking in the Hamiltonian. The details of this approach and its implementation in `Wannier90` were discussed by Pizzi *et al.* (2020).

Once the on-site energies and hoppings have been tabulated, the Hamiltonian matrix is interpolated onto an arbitrary BZ point $\mathbf{k}'$ by performing an inverse Fourier transform,

$$H^{\mathrm{W}}_{\mathbf{k}',ij} = \sum_{\mathbf{R}}^{\mathrm{WS}} \frac{1}{\mathcal{N}_{\mathbf{R},ij}} \sum_{l=1}^{\mathcal{N}_{\mathbf{R},ij}} e^{i\mathbf{k}'\cdot(\mathbf{R}+\mathbf{T}^{l}_{\mathbf{R},ij})} H^{\mathrm{W}}_{ij}(\mathbf{R}). \tag{17}$$

The summation runs over the lattice vectors $\mathbf{R}$ (which lie in the WS supercell centered at the origin, as discussed), with $\mathcal{N}_{\mathbf{R}} > 1$ whenever $\mathbf{R}+\mathbf{T}^{l}_{\mathbf{R},ij}+\boldsymbol{\tau}_j$ falls on the boundary of the WS supercell centered at $\boldsymbol{\tau}_i$. To improve the quality of the interpolation, for each combination of i, j, and $\mathbf{R}$, the supercell lattice vector $\mathbf{T}$ appearing in Eq. (17) is chosen as the one that minimizes $|\mathbf{R}+\mathbf{T}+\boldsymbol{\tau}_j-\boldsymbol{\tau}_i|$ (Pizzi *et al.*, 2020). Finally, the interpolated energy eigenvalues are obtained by diagonalizing the aforementioned matrix,

$$[\mathcal{U}^{\dagger}_{\mathbf{k}'}H^{\mathrm{W}}_{\mathbf{k}'}\mathcal{U}_{\mathbf{k}'}]_{mn} = \delta_{mn}\varepsilon^{\mathrm{H}}_{n\mathbf{k}'}, \tag{18}$$

so that the column vectors of the unitary matrix $\mathcal{U}_{\mathbf{k}'}$ are eigenvectors of $H^{\mathrm{W}}_{\mathbf{k}'}$.

Since the interpolation steps (17) and (18) only involve Fourier transforming and diagonalizing $J\times J$ matrices that are typically small, the overall procedure tends to be much less expensive than a direct DFT calculation at every interpolation point, especially when a dense interpolation grid $\{\mathbf{k}'\}$ is needed. The efficient evaluation of the Hamiltonian matrix and band derivatives (as later discussed) enables BZ integration methods beyond the standard equispaced scheme to be explored. These are of particular use when fine features in k space need to be resolved using adaptive integration methods (Assmann *et al.*, 2016; Kaye *et al.*, 2023; Van Muñoz *et al.*, 2024).

This interpolation scheme has been shown to accurately reproduce—within the frozen energy window—the energy eigenvalues obtained via a direct DFT calculation. We show in Fig. 7 details of the interpolated band structure of ferromagnetic bcc Fe along the H–Γ line (Yates *et al.*, 2007). The vertical gray lines indicate points on the $\{\mathbf{k}\}$ mesh used for constructing the WFs. For comparison we plot as plus symbols the *ab initio* dispersion around a weak spin-orbit-induced avoided crossing between two bands of opposite spin. It is apparent that the Wannier-interpolation procedure succeeds in resolving details on a scale much smaller than the spacing between those points. In particular, the correct band connectivity is obtained, so avoided crossings, no matter how weak, are not mistaken for actual crossings. This characteristic, which distinguishes Wannier interpolation from methods based on direct Fourier interpolation of the energy eigenvalues (Madsen and Singh, 2006; Madsen, Carrete, and Verstraete, 2018), makes it a powerful tool for studying topological properties (see Sec. III.F) and for evaluating BZ integrals involving quantities that change rapidly over small regions of k space, such as the Berry curvature (see Sec. III.E) and electron-phonon matrix elements (see Sec. III.G).

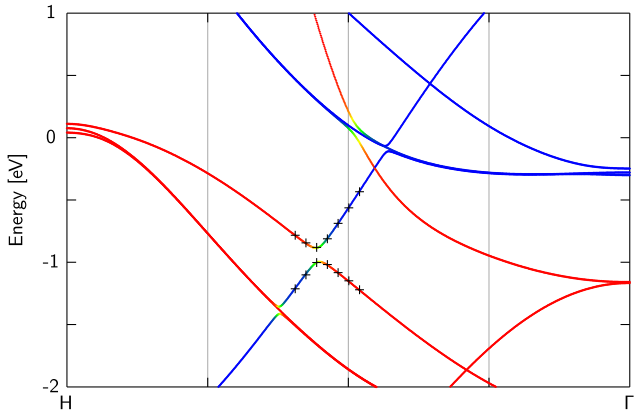

FIG. 7. Wannier-interpolated bands of bcc Fe along the H–Γ line. The bands are color coded according to the spin expectation value $\langle\psi_{n\mathbf{k}}|\hat{S}_z|\psi_{n\mathbf{k}}\rangle$: red for spin-up and blue for spin-down. The energies are given in eV, and the Fermi level is at 0 eV. The vertical gray lines indicate k points on the *ab initio* mesh used for constructing the WFs.

Wannier interpolation works for the same reason that empirical TB does: the short range of the real-space Hamiltonian matrix (16) ensures that its Fourier transform (17) is a smooth function in reciprocal space. This can also be seen by writing the left-hand side of Eq. (17) as

$$H^{\mathrm{W}}_{\mathbf{k}',ij} = \langle\psi^{\mathrm{W}}_{i\mathbf{k}'}|\hat{H}|\psi^{\mathrm{W}}_{j\mathbf{k}'}\rangle, \tag{19}$$

where

$$|\psi^{\mathrm{W}}_{j\mathbf{k}'}\rangle = \sum_{\mathbf{R}} e^{i\mathbf{k}'\cdot\mathbf{R}}|\mathbf{R}\,j\rangle \tag{20}$$

interpolates the smooth Bloch functions defined on the *ab initio* grid by Eq. (6b). We can also write the left-hand side of Eq. (18) as

$$H^{\mathrm{H}}_{\mathbf{k}',mn} = \langle\psi^{\mathrm{H}}_{m\mathbf{k}'}|\hat{H}|\psi^{\mathrm{H}}_{n\mathbf{k}'}\rangle, \tag{21}$$

where

$$|\psi^{\mathrm{H}}_{n\mathbf{k}'}\rangle = \sum_{j=1}^{J} |\psi^{\mathrm{W}}_{j\mathbf{k}'}\rangle\mathcal{U}_{\mathbf{k}',jn} \tag{22}$$

describes a unitary transformation from the Wannier gauge W to the Hamiltonian gauge H. Inside the frozen energy window, the states $|\psi^{\mathrm{H}}_{n\mathbf{k}'}\rangle$ interpolate—up to arbitrary phase factors—the *ab initio* eigenstates $|\psi_{n\mathbf{k}}\rangle$.

In summary, performing Fourier interpolation in the W gauge followed by a unitary transformation to the H gauge allows one to interpolate quantities—band energies, Bloch eigenstates, and matrix elements thereof (discussed later)—that can vary rapidly in k space, and even become nonanalytic at degeneracies. This strategy retains the accuracy of a full-blown *ab initio* calculation while benefiting from the efficiency of Slater-Koster interpolation.

2. Band derivatives and Boltzmann transport

The previously outlined interpolation procedure can be adapted to evaluate band velocities, inverse effective-mass tensors, and higher k derivatives of the energy eigenvalues (Yates *et al.*, 2007). As in the empirical TB method (Graf and Vogl, 1995), this is achieved without relying on finite-difference methods, which become problematic near band crossings and weak avoided crossings, where the band ordering can change from one grid point to the next.

Band derivatives are needed to evaluate transport coefficients such as the electrical conductivity σ, the Seebeck coefficient S, and the electronic contribution to the thermal conductivity K. Within the semiclassical Boltzmann transport equation (BTE) framework, one defines a scattering time $\tau_{n\mathbf{k}}$ for an electron on band n at wave vector $\mathbf{k}$ (the contributions from electron-phonon scattering to $\tau_{n\mathbf{k}}$ can be efficiently computed by exploiting Wannier functions; see Sec. III.G). Then the expressions for the transport tensors are given by (Ziman, 1972):

$$\sigma_{ab}(\mu,T) = e^2\int_{-\infty}^{+\infty} dE\left(-\frac{\partial f(E,\mu,T)}{\partial E}\right)\Sigma_{ab}(E), \tag{23}$$

$$[\sigma S]_{ab}(\mu,T) = \frac{e}{T}\int_{-\infty}^{+\infty} dE\left(-\frac{\partial f(E,\mu,T)}{\partial E}\right)(E-\mu)\Sigma_{ab}(E), \tag{24}$$

$$K_{ab}(\mu,T) = \frac{1}{T}\int_{-\infty}^{+\infty} dE\left(-\frac{\partial f(E,\mu,T)}{\partial E}\right)(E-\mu)^2\Sigma_{ab}(E), \tag{25}$$

where μ is the chemical potential, T is the temperature, a and b are Cartesian indices, σS denotes the matrix product of the two tensors, $\partial f/\partial E$ is the derivative of the Fermi-Dirac distribution function with respect to the energy, and $\Sigma_{ab}(E)$ is the transport distribution function. The last item is defined by

$$\Sigma_{ab}(E) = \frac{1}{V_{\mathrm{cell}}}\sum_{n\mathbf{k}} v^a_{n\mathbf{k}} v^b_{n\mathbf{k}}\tau_{n\mathbf{k}}\delta(E-E_{n\mathbf{k}}), \tag{26}$$

where the summation is over all bands n and over the entire BZ, $\varepsilon_{n\mathbf{k}}$ is the energy for band n at $\mathbf{k}$, and $v^a_{n\mathbf{k}}$ is the a component of the band velocity at $(n,\mathbf{k})$.

Obtaining converged quantities for Eqs. (23)–(25) therefore requires one to compute the band derivatives $\mathbf{v}_{n\mathbf{k}}$ while sampling the BZ over dense k-point grids (Schulz, Allen, and Trivedi, 1992; Uehara and Tse, 2000; Madsen and Singh, 2006) since the term $\partial f/\partial E$ is nonzero only in a narrow energy region (with a typical size k_BT, where k_B is the Boltzmann constant) around the chemical potential μ. Wannier interpolation allows this task to be carried out efficiently and accurately even when avoided crossings occur close to the Fermi level. Band derivatives at a given k point are obtained with an analytical expression without having to resort to finite-difference methods (Yates *et al.*, 2007). Moreover, computation on dense k-point grids is highly

efficient, as previously discussed for band interpolation. This WF-based Boltzmann transport methodology is implemented in `Wannier90` and used to compute transport tensors in its `BoltzWann` module (Pizzi *et al.*, 2014), as well as in other codes (see the electron-phonon discussion in Sec. III.G), and is also used for postprocessing calculations in many-body theory (see Sec. III.H.1).

Furthermore, many transport coefficients [such as linear and nonlinear anomalous Hall conductivities (AHCs) (Yao *et al.*, 2004; Sodemann and Fu, 2015), anomalous Nernst thermoelectric conductivity (Xiao *et al.*, 2006), magnetoresistance (Gao, Yang, and Niu, 2017), and magnetochiral anisotropy (Yokouchi *et al.*, 2023)] depend on the Berry curvature and other quantum-geometric quantities (Xiao, Chang, and Niu, 2010; Vanderbilt, 2018; Gao, 2019). As they involve k derivatives of the Bloch states themselves, these quantities cannot be obtained from the energy dispersions. Moreover, those quantities tend to become strongly enhanced when weak avoided crossings occur near the Fermi level; when that happens, dense k-point grids must be employed to converge the calculation (Yao *et al.*, 2004). Compared to band interpolation, the interpolation of Berry-type quantities is more involved because it requires setting up matrix elements of the position operator $\hat{\mathbf{r}}$, which is nonlocal in reciprocal space, i.e., not lattice periodic (Blount, 1962). We defer a discussion of that case to Sec. III.E, and we now describe how to interpolate the matrix elements of a generic lattice-periodic operator $\hat{X}$.

3. Interpolation of a generic lattice-periodic operator

Replacing $\hat{H} \to \hat{X}$ in Eq. (15) and using Eq. (6) yield

$$X^{\mathrm{W}}_{ij}(\mathbf{R}) = \frac{1}{N}\sum_{\mathbf{k}} e^{-i\mathbf{k}\cdot\mathbf{R}} \sum_{m,n=1}^{\mathcal{J}_{\mathbf{k}}} V^{*}_{\mathbf{k},mi} \langle \psi_{m\mathbf{k}}|\hat{X}|\psi_{n\mathbf{k}}\rangle V_{\mathbf{k},nj}, \tag{27}$$

which reduces to Eq. (16) for $\hat{X} = \hat{H}$. The considerations made earlier regarding the spatial decay and truncation of the $H^{\mathrm{W}}(\mathbf{R})$ matrix apply equally well to $X^{\mathrm{W}}(\mathbf{R})$. The Fourier-transform step is also analogous to Eq. (17),

$$X^{\mathrm{W}}_{\mathbf{k}',ij} = \sum_{\mathbf{R}} e^{i\mathbf{k}'\cdot\mathbf{R}} X^{\mathrm{W}}_{ij}(\mathbf{R}) = \langle \psi^{\mathrm{W}}_{i\mathbf{k}'}|\hat{X}|\psi^{\mathrm{W}}_{j\mathbf{k}'}\rangle, \tag{28}$$

and the final step is to apply to $X^{\mathrm{W}}_{\mathbf{k}'}$ the same unitary transformation that was used in Eq. (18) to diagonalize $H^{\mathrm{W}}_{\mathbf{k}'}$. Using Eq. (22), we find that

$$X^{\mathrm{H}}_{\mathbf{k}',mn} = (\mathcal{U}^{\dagger}_{\mathbf{k}'} X^{\mathrm{W}}_{\mathbf{k}'} \mathcal{U}_{\mathbf{k}'})_{mn} = \langle \psi^{\mathrm{H}}_{m\mathbf{k}'}|\hat{X}|\psi^{\mathrm{H}}_{n\mathbf{k}'}\rangle. \tag{29}$$

In particular, diagonal elements of $X^{\mathrm{H}}_{\mathbf{k}'}$ give the expectation values of $\hat{X}$ in the interpolated states. With $\hat{X} = \hat{\mathbf{S}}$ one obtains their spin polarization, which is how the color coding in Fig. 7 was generated.

Note that in addition to the overlap matrices and energy eigenvalues, interpolating a generic operator $\hat{X} \neq \hat{H}$ requires its matrix elements $\langle \psi_{m\mathbf{k}}|\hat{X}|\psi_{n\mathbf{k}}\rangle$ to be set up on the *ab initio* grid. This should be done via the same interface code that computes the overlap matrices.

4. Wannier-function perturbation theory

Several important materials properties can be calculated as the linear response of the system to an external perturbation $\hat{V}$. A common example is the calculation of phonon dispersions and electron-phonon coupling through density-functional perturbation theory (DFPT) (Baroni *et al.*, 2001); the latter case is discussed in Sec. III.G.

We follow Lihm and Park (2021) and write the Hamiltonian eigenstates of the perturbed system in terms of those of the unperturbed system plus the wave function perturbation,

$$|\psi_{n\mathbf{k}}\rangle = |\psi_{n\mathbf{k}}\rangle^{(0)} + \lambda|\psi_{n\mathbf{k}}\rangle^{(1)} + \mathcal{O}(\lambda^2), \tag{30}$$

where the wave function perturbation can be calculated with a sum over empty states,

$$|\psi_{n\mathbf{k}}\rangle^{(1)} = \sum_{n'\mathbf{k}'}{}' |\psi_{n'\mathbf{k}'}\rangle^{(0)} \frac{\langle \psi_{n'\mathbf{k}'}|\hat{V}|\psi_{n\mathbf{k}}\rangle^{(0)}}{\epsilon_{n\mathbf{k}} - \epsilon_{n'\mathbf{k}'}}. \tag{31}$$

The primed sum indicates that terms for which the denominator vanishes are excluded.

Alternatively, the wave function perturbation can be calculated without summing over high-energy states by solving the Sternheimer equation (Baroni *et al.*, 2001). Lihm and Park (2021) showed that this perturbation theory can be formulated in the Wannier representation, where the WFs of the perturbed system can be written as

$$|\mathbf{R}j\rangle = |\mathbf{R}j\rangle^{(0)} + \lambda|\mathbf{R}j\rangle^{(1)} + \mathcal{O}(\lambda^2). \tag{32}$$

The expression for $|\mathbf{R}j\rangle^{(1)}$, which was reported by Lihm and Park (2021), consists of two terms: the first can be calculated with the Sternheimer equation to obtain the states $|\psi_{n\mathbf{k}}\rangle^{(1)}$, while the second contains matrix elements of $\hat{V}$ and the projector over the WFs of the unperturbed system. Note that both terms require energies and matrix elements only within the Wannier outer window introduced in Sec. II.A.2. Thus, the Wannier-function perturbation can be calculated without making explicit use of the states outside that energy window.

For a monochromatic static perturbation with wave vector $\mathbf{q}$, the first-order wave function perturbation can be interpolated as (Lihm and Park, 2021)

$$|\psi^{\mathrm{H}}_{n\mathbf{k}',\mathbf{q}}\rangle^{(1)} = \frac{1}{\sqrt{N}}\sum_{j,\mathbf{R}} e^{i\mathbf{k}'\cdot\mathbf{R}} |\mathbf{R}_{\mathbf{q}}j\rangle^{(1)} \mathcal{U}_{\mathbf{k}',jn} + \sum_{m=1}^{N_W}{}' |\psi^{\mathrm{H}}_{m\mathbf{k}'+\mathbf{q}}\rangle^{(0)} \frac{\tilde{g}^{\mathrm{H}}_{mn\mathbf{k}',\mathbf{q}}}{\epsilon^{(0)}_{n\mathbf{k}'} - \epsilon^{(0)}_{m\mathbf{k}'+\mathbf{q}}}, \tag{33}$$

where the WF perturbations are expanded as a sum of monochromatic perturbations

$$|\mathbf{R}j\rangle^{(1)} = \sum_{\mathbf{q}} |\mathbf{R}_{\mathbf{q}}j\rangle^{(1)}, \tag{34}$$

while the superscript H marks the Hamiltonian gauge of the unperturbed (0) and perturbed (1) system, $\mathcal{U}_{\mathbf{k}'}$ is the unitary matrix that diagonalizes the unperturbed Hamiltonian according to Eq. (18), and $\tilde{g}^{\mathrm{H}}_{mn\mathbf{k},\mathbf{q}}$ is obtained by performing the Fourier transform of $\tilde{g}_{ij\mathbf{R},\mathbf{q}}$ and then rotating it to the Hamiltonian gauge using $\mathcal{U}_{\mathbf{k}'}$. The quantity $\tilde{g}_{ij\mathbf{R},\mathbf{q}}$ is related to the perturbation and is made of two terms ($\tilde{g}_{ij\mathbf{R},\mathbf{q}} = g_{ij\mathbf{R},\mathbf{q}} + \delta g_{ij\mathbf{R},\mathbf{q}}$). The first term accounts for the matrix elements of $\hat{V}$ between WFs of the unperturbed states

$$g_{ij\mathbf{R},\mathbf{q}} = \langle \mathbf{0}i^{(0)}|\hat{V}_{\mathbf{q}}|\mathbf{R}j^{(0)}\rangle, \tag{35}$$

while the second term is a correction stemming from the change of the WFs

$$\delta g_{ij\mathbf{R},\mathbf{q}} = \langle \mathbf{0}i^{(0)}|\hat{H}^{(0)}|\mathbf{R}_{\mathbf{q}}j^{(1)}\rangle + \langle \mathbf{0}_{-\mathbf{q}}i^{(1)}|\hat{H}^{(0)}|\mathbf{R}j^{(0)}\rangle. \tag{36}$$

The correction term $\delta g_{ij\mathbf{R},\mathbf{q}}$ is not required for the scattering matrix elements, but it is relevant for the perturbed wave functions. A key aspect is that Wannier-function perturbations are localized in real space, so the perturbed Hamiltonian and its eigenstates can be efficiently interpolated by considering coarse k-point grids. This permits the efficient interpolation of various matrix elements involving the wave function perturbation, as in the case of electron-phonon self-energies and Kubo formulas. Wannier-function perturbation theory (WFPT) has been applied to describe temperature-dependent electronic band structures and indirect optical absorption, shift spin currents, and spin Hall conductivities (Lihm and Park, 2021). WFPT was recently made available in the `EPW` code version 5.8 (Lee *et al.*, 2023).

5. Porting Wannier Hamiltonians to TB codes

In TB theory two phase conventions are commonly used to perform the Fourier transforms from real to reciprocal space (Vanderbilt, 2018): the one adopted in Eqs. (17), (20) and (28) (*original convention*), and the alternative one (*modified convention*), where the phase factors in those equations are modified as

$$e^{i\mathbf{k}'\cdot\mathbf{R}} \rightarrow e^{i\mathbf{k}'\cdot(\mathbf{R}+\boldsymbol{\tau}_j-\boldsymbol{\tau}_i)}. \tag{37}$$

Although the interpolated eigenvalues $\varepsilon^{\mathrm{H}}_{n\mathbf{k}'}$ and matrix elements $X^{\mathrm{H}}_{\mathbf{k}',mn}$ come out the same with both conventions (as they should), the modified convention is more natural for the purpose of evaluating quantities, such as Berry connections and curvatures, that are sensitive to the real-space embedding of the TB model via the position matrix elements $\langle \mathbf{0}i|\hat{\mathbf{r}}|\mathbf{R}j\rangle$; see Sec. III.E. This has to do with the fact that, with the original convention, TB eigenvectors (the column vectors of $\mathcal{U}_{\mathbf{k}'}$) behave like full Bloch eigenstates $|\psi_{n\mathbf{k}'}\rangle$, whereas with the modified convention they behave like their cell-periodic parts $|u_{n\mathbf{k}'}\rangle$ (Vanderbilt, 2018). It is in terms of the latter that Berry-type quantities are most naturally expressed.

The modified phase convention is the one adopted in the TB codes `PythTB` (PythTB Collaboration, 2023) and `TBmodels` (TBmodels Collaboration, 2023); both are able to import the Wannier Hamiltonian $H^{\mathrm{W}}_{ij}(\mathbf{R})$, along with the Wannier centers $\{\boldsymbol{\tau}_j\}$, from the `seedname_tb.dat` file written with `Wannier90`. `PythTB` was originally written for pedagogical purposes as part of a course on Berry phases in electronic-structure theory that was later turned into a textbook (Vanderbilt, 2018). It is feature rich but is not optimized for speed, as it was designed with TB toy models in mind [however, a high-performance implementation is available (Numba-PythTB Collaboration, 2023)]. Instead, `TBmodels` has fewer postprocessing functionalities, but it delivers critical speedup and improved scaling. Notable among the Wannier-TB codes is `WannierTools` (Wu *et al.*, 2018), which implements sparse Hamiltonians for large systems, band unfolding, and several other features related to Berry-type quantities; see Sec. III.E.

6. Wannier interpolation beyond density-functional theory

As discussed, one of the most powerful and effective applications of WFs is the interpolation of band structures and other electronic-structure properties. While this is already useful in the context of DFT calculations, it becomes even more compelling for beyond-DFT methods, such as hybrid functionals (Becke, 1988, 2014; Lee, Yang, and Parr, 1988; Perdew, Ernzerhof, and Burke, 1996; Heyd, Scuseria, and Ernzerhof, 2003; Kümmel and Kronik, 2008; Martin, 2020), many-body perturbation theory (MBPT) such as G_0W_0 (Golze, Dvorak, and Rinke, 2019), and nondiagrammatic approaches such as the Koopmans-compliant functionals (Dabo *et al.*, 2010; Borghi *et al.*, 2014; Colonna *et al.*, 2018, 2019, 2022; Elliott *et al.*, 2019; Zhou and Bernardi, 2019; De Gennaro *et al.*, 2022; Linscott *et al.*, 2023; Marrazzo and Colonna, 2024). In fact, in DFT the potential can always be recalculated with the sole knowledge of the ground-state electronic charge density; therefore, the corresponding KS Hamiltonian can be directly calculated at any arbitrary k point. Instead, for most beyond-DFT methods, this is no longer the case, and band-structure calculations on a high-symmetry path cannot be performed as a series of independent diagonalizations. For hybrid functionals and GW, the eigenvalues at a given k point require the knowledge of the wave functions and eigenenergies on all reciprocal-space points $\mathbf{k}+\mathbf{q}$, where the $\mathbf{q}$ points are defined on a uniform grid that has to be converged. In other words, reasonably dense sampling on high-symmetry paths can be obtained only with some form of interpolation.

While electronic-structure codes typically offer general-purpose interpolation methods, often based on Fourier series (Koelling and Wood, 1986; Pickett, Krakauer, and Allen, 1988), WFs provide two concrete advantages. First, they are a physically motivated basis set, which exhibits exponential convergence and is guaranteed to deliver the exact result for a sufficiently dense k-point grid, so the accuracy can be systematically increased simply by considering denser grids. If MLWFs are chosen, the efficiency is maximal and coarse grids are often sufficient to faithfully reproduce the entire band structure. Second, once a WF basis is constructed, it not only yields interpolated eigenvalues (such as the band structure) but also enables the Hamiltonian and many other operators to be described in a compact real-space representation. Once the relevant operators in a WF basis are available, one gets access to the full spectrum of theories and software packages that are

part of the Wannier ecosystem, which is capable of much more complex tasks than simply band interpolation. Notably, once a Wannierization is performed with hybrid functionals or at the G_0W_0 level, all other Wannier-interpolated quantities can be obtained at the same level of theory with no extra effort or cost. Finally, thanks to recent work in advanced minimization techniques (see Sec. II.D) and automation (see Sec. III.J), the Wannier interpolation does not require much more human intervention than other standard methods such as smooth Fourier interpolation. In the following we outline the motivation and the corresponding procedure to deploy Wannier interpolation for two of the most popular excited-state approaches: hybrid functionals and many-body perturbation theory at the G_0W_0 level.

a. Hybrid functionals

A popular approach to improve the accuracy of *ab initio* band structures is to combine explicit density-dependent functionals with Hartree-Fock terms, which leads to orbital-dependent functionals called hybrids (Becke, 1988, 2014; Lee, Yang, and Parr, 1988; Perdew, Ernzerhof, and Burke, 1996; Heyd, Scuseria, and Ernzerhof, 2003; Kümmel and Kronik, 2008; Martin, 2020). The procedure to obtain WFs is similar to that in vanilla DFT, except that non-self-consistent field (NSCF) calculations cannot be performed, as the potential is not a functional of the total density only but requires the knowledge of single-particle orbitals. Hence, only self-consistent field (SCF) calculations are performed with hybrid functionals, including some higher-energy empty states (if there are any) that might be needed to obtain Wannier functions through disentanglement (Souza, Marzari, and Vanderbilt, 2001). This is different with respect to DFT, where a SCF calculation is typically performed on the occupied states only (plus some lower-lying conduction bands in the case of metals) and a NSCF calculation is performed including higher-energy empty states, possibly on a different k-point grid. In addition, ground-state calculations are typically performed on the irreducible Brillouin zone (IBZ) by exploiting crystalline symmetries, while `Wannier90` requires a uniform grid on the full Brillouin zone (FBZ). As performing the self-consistent calculation on the FBZ is certainly possible but rather inefficient, the typical procedure involves unfolding the ground-state orbitals and band structure from the IBZ to the FBZ. This is done as a postprocessing step performed after the self-consistent calculation and before producing the overlap matrices and the other input required to obtain WFs. For example, in the `Quantum ESPRESSO` distribution (Giannozzi *et al.*, 2009, 2017), this is done through the `open_grid.x` code. Notably, WFs can be used to speed up the core hybrid-functional calculations, as they allow one to reduce the number of exchange integrals to be computed (Weinan, García-Cervera, and Lu, 2007; García-Cervera *et al.*, 2009; Wu, Selloni, and Car, 2009; DiStasio *et al.*, 2014; Mountjoy, Todd, and Mosey, 2017; Carnimeo, Baroni, and Giannozzi, 2019).

b. G_0W_0

Most of what has been discussed for hybrid functionals also holds for MBPT calculations in the G_0W_0 approximation, with two important remarks. First, G_0W_0 is a one-shot approach in the quasiparticle (QP) approximation that is typically performed on top of a DFT calculation. Thus, the orbitals remain at the KS level and only the energy eigenvalues are corrected, hence neglecting off-diagonal elements of the self-energy in the KS basis. Second, as only the energies are changed at the G_0W_0 level, the KS states might swap their band indices and no longer be ordered in energy. A typical case where this might manifest is topological insulator candidates (and systems with band inversions in general) such as monolayer TiNI (Marrazzo *et al.*, 2019), which is topological in DFT and trivial at the G_0W_0 level. The practicalities of obtaining G_0W_0 WFs and related quantities depend on whether the DFT and MBPT calculations are performed with the same distribution [for example, `VASP` (Kaltak, 2015)] or with two separate codes [as with `Quantum ESPRESSO` (Giannozzi *et al.*, 2009, 2017) and `Yambo` (Sangalli *et al.*, 2019)]. In general, G_0W_0 QP corrections $\Delta\epsilon_i^{\mathrm{QP}} = \epsilon_i^{G_0W_0} - \epsilon_i^{\mathrm{DFT}}$ need to be computed on a uniform grid in the FBZ, which can be made efficient by unfolding from the IBZ to the FBZ (in `Yambo`, this operation is carried out by the postprocessing utility `ypp`). While orbitals remain at the DFT-KS level, `Wannier90` requires the states to be ordered with ascending energy and, in addition, some input matrices (for example, the `uHu`) need to be updated with QP corrections. If this is not performed by the *ab initio* engine, it can be taken care by the `Wannier90` utility `gw2wannier90.py` if the DFT eigenvalues and QP corrections are provided in the standard format `seedname.eig`. After this step the Wannierization can proceed as usual, and it is available in both `Wannier90` (Pizzi *et al.*, 2020) and `WanT` (Ferretti *et al.*, 2012). Note that in G_0W_0 QP corrections need to be computed on a subset of the k-point grid required to calculate the self-energy. This can be exploited to speed up the calculation, especially for 2D materials, as discussed by Sangalli *et al.* (2019), because Wannierization typically requires relatively coarse k-point grids. Finally, we address beyond-G_0W_0 development of interest from a WF perspective. While Aguilera *et al.* (2013) showed that off-diagonal components of the self-energy—which are not included in standard perturbative approaches—are relevant in the case of band inversions (such as for topological insulators), Hamann and Vanderbilt (2009) found that differences between MLWFs obtained with the local-density approximation (LDA) and the quasiparticle self-consistent GW (QSGW) approximation are generally minimal.

c. Bethe-Salpeter equation

To address neutral excitations, as opposed to the charged excitations of GW, one needs to describe the bound state of an excited electron with the hole that has been created. This is accomplished either using time-dependent density-functional theory or Green's function methods (Onida, Reining, and Rubio, 2002). In the latter case the Bethe-Salpeter equation (BSE) is solved on top of the GW solutions. Within the Tamm-Dancoff approximation (Dancoff, 1950; Hirata and Head-Gordon, 1999; Onida, Reining, and Rubio, 2002), the BSE can be recast into an effective two-particle eigenvalue problem

(Rohlfing and Louie, 2000; Onida, Reining, and Rubio, 2002), which in the electron-hole (e-h) basis reads

$$\sum_{v'c'}[D_{vc,v'c'}+2K^{\mathrm{x}}_{vc,v'c'}-K^{\mathrm{d}}_{vc,v'c'}]A^{\lambda}_{v'c'}=E_{\lambda}A^{\lambda}_{vc}, \quad (38)$$

where the v, v' and c, c' indices run over valence and conduction states, E_λ are the neutral excitation energies (the poles of the density-density response function), and A^{λ}_{vc} are the coefficients of the excitonic wave functions that are related to oscillator strengths in the e-h basis. The effective two-particle Hamiltonian is made by (i) a diagonal term $D_{vc,v'c'}=(\varepsilon^{\mathrm{QP}}_c-\varepsilon^{\mathrm{QP}}_v)\delta_{vv'}\delta_{cc'}$ representing the "bare" e-h transitions (i.e., without accounting for the electron-hole interaction) from the QP theory, (ii) an exchangelike term

$$K^{\mathrm{x}}_{vc,v'c'}=\int d\mathbf{r}d\mathbf{r}'\,\phi^*_c(\mathbf{r})\phi_v(\mathbf{r})|\mathbf{r}-\mathbf{r}'|^{-1}\phi^*_{v'}(\mathbf{r}')\phi_{c'}(\mathbf{r}'), \quad (39)$$

and (iii) a direct screened Coulomb term

$$K^{\mathrm{d}}_{vc,v'c'}=\int d\mathbf{r}d\mathbf{r}'\,\phi^*_c(\mathbf{r})\phi_{c'}(\mathbf{r})W(\mathbf{r},\mathbf{r}')\phi^*_{v'}(\mathbf{r}')\phi_v(\mathbf{r}') \quad (40)$$

responsible for an effective attractive interaction between the electron and the hole. In Eqs. (39) and (40) $\{\phi_i\}$ and $\{\varepsilon^{\mathrm{QP}}_i\}$ are the QP wave functions and QP energies, respectively. The solution of Eq. (38) in the e-h basis would require the explicit computation of a significant number of empty states, which becomes in turn a critical convergence parameter. This can be avoided (Giustino, Cohen, and Louie, 2010; Rocca, Lu, and Galli, 2010; Umari *et al.*, 2011; Marsili *et al.*, 2017) resorting to well established techniques from DFPT (Baroni *et al.*, 2001) by introducing (i) the projector over the conduction manifold $\hat{Q}=\mathbb{1}-\hat{P}=\mathbb{1}-\sum_v|\phi_v\rangle\langle\phi_v|$ and (ii) a set of auxiliary functions $\xi_v(\mathbf{r})=\sum_c A_{cv}\phi_c(\mathbf{r})$, usually called a *batch* representation (Walker *et al.*, 2006; Rocca *et al.*, 2008). These are N_v (where N_v is the number of occupied states) auxiliary functions that live in the unperturbed empty-states manifold and provide an equivalent but more compact representation of the excitonic wave function $\Theta(\mathbf{r},\mathbf{r}')=\sum_{vc}A_{cv}\phi^*_v(\mathbf{r})\phi_c(\mathbf{r}')=\sum_v\phi^*_v(\mathbf{r})\xi_v(\mathbf{r}')$. In this representation the effective two-particle Hamiltonian is completely specified by its action on the components of the batch (Rocca, Lu, and Galli, 2010),

$$\sum_{v'}D_{vv'}|\xi_{v'}\rangle=\sum_{v'}(\hat{H}^{\mathrm{QP}}-\varepsilon_{v'}\mathbb{1})\delta_{vv'}|\xi_{v'}\rangle, \quad (41)$$

$$\sum_{v'}K^{\mathrm{x}}_{vv'}|\xi_{v'}\rangle=\sum_{v'}\hat{Q}\left(\int\frac{1}{|\mathbf{r}-\mathbf{r}'|}\phi^*_{v'}(\mathbf{r}')\xi_{v'}(\mathbf{r}')d\mathbf{r}'\right)|\phi_v\rangle, \quad (42)$$

$$\sum_{v'}K^{\mathrm{d}}_{vv'}|\xi_{v'}\rangle=\sum_{v'}\hat{Q}\left(\int W(\mathbf{r},\mathbf{r}')\phi^*_{v'}(\mathbf{r}')\phi_{v'}(\mathbf{r}')d\mathbf{r}'\right)|\xi_{v'}\rangle. \quad (43)$$

The advantage of this formulation is that there is no explicit reference to the empty states (hidden inside the projector $\hat{Q}$ and the batch representation), and only the N_v auxiliary functions $\{|\xi_v\rangle\}$ need to be determined by solving the BSE in the batch representation.

A further computational speedup [and an improvement on the overall scaling (Marsili *et al.*, 2017)] can be achieved by moving from the KS orbitals to MLWFs and by exploiting their localization to greatly reduce the number of operations needed to evaluate the action of the BSE Hamiltonian on a trial state $|\xi_v\rangle$. This is particularly relevant for the direct term [Eq. (43)], which represents the real bottleneck of the calculations. In the Wannier representation this becomes

$$\sum_{v'}K^{\mathrm{d}}_{vv'}|\tilde{\xi}_{v'}\rangle=\hat{Q}\left(\sum_{v'}\int W(\mathbf{r},\mathbf{r}')\omega^*_{v'}(\mathbf{r}')\omega_{v'}(\mathbf{r}')d\mathbf{r}'\right)|\tilde{\xi}_{v'}\rangle, \quad (44)$$

where $\{\omega_v(\mathbf{r})\}$ are the MLWFs and $\tilde{\xi}_v(\mathbf{r})$ is the batch component in the Wannier representation [simply obtained by rotating the original $\xi_v(\mathbf{r})$ with the unitary matrix rotation that transforms the manifold from the canonical to the MLWF representation]. Exploiting locality, one can define a threshold for which a given pair of MLWFs overlap. By excluding nonoverlapping pairs of MLWFs from the summation in Eq. (44), it becomes possible to lower the scaling of the evaluation of the action of the direct term on trial states from $\mathcal{O}(N^4)$ to $\mathcal{O}(N^3)$ (Marsili *et al.*, 2017), an approach that has been established and applied in the community (Umari *et al.*, 2011; Marsili *et al.*, 2017; Elliott *et al.*, 2019). Tight-binding and phenomenological models based on localized representation have also recently appeared (Peng *et al.*, 2019; Dias, Silveira, and Qu, 2023; Uría-Álvarez *et al.*, 2024).

The concept of MLWF can actually be extended to multiparticle Bloch states and has recently been applied to excitons, which are two-particle correlated e-h excitations, and where maximal localization can be defined with respect to an average e-h coordinate in real space (Haber *et al.*, 2023). The benefits of these maximally localized exciton Wannier functions (MLXWFs) for excitons are essentially the same as those of MLWFs for electrons, including provision of a compact basis for *ab initio* exciton TB models and interpolation of key quantities such as the excitonic bands, the exciton-phonon matrix elements, and Berry curvatures for the exciton wave function. They also provide physical insights on the nature of excitons (Haber *et al.*, 2023).

D. Ballistic transport and nanostructures

MLWFs can be used to build the electronic structure of large nanostructures (Lee, Nardelli, and Marzari, 2005; Lihm and Park, 2019) and to determine their ballistic transport when connected to semi-infinite leads (Calzolari *et al.*, 2004; Lee, Nardelli, and Marzari, 2005). In the latter case the formalism of Green's functions is used to embed a conductor into the surrounding environment. In all cases the building blocks are Hamiltonian matrix elements between the localized MLWFs that are used to construct, LEGO-like, either the desired non-self-consistent Hamiltonian of a much larger nanostructure or the self-energies embedding the conductor of interest into semi-infinite leads. Any solid or surface can be viewed as an

infinite (or semi-infinite, in the case of surfaces) stack of "principal layers" interacting only with neighboring layers (Lee and Joannopoulos, 1981a, 1981b). In this way the infinite-dimensional real-space Hamiltonian can be divided into finite-size Hamiltonian matrices. For a bulk system (i.e., infinite and periodic) the only independent components are H_{00} and H_{01}, where the former represents the interaction between MLWFs located in the same principal layer and the latter stands for the interaction between orbitals in one principal layer and the next.

As discussed by Buongiorno Nardelli (1999), one can consider a system composed of a conductor C connected to two semi-infinite leads R and L (C, R, and L are themselves composed of a finite or infinite number of principal layers). The conductance through C is related to the scattering properties of C itself via the Landauer formula (Landauer, 1970),

$$\mathcal{G}(E) = \frac{2e^2}{h}\mathcal{T}(E), \tag{45}$$

where $\mathcal{T}$ is the transmission function and $\mathcal{G}$ is the conductance. The transmission function represents the probability that an electron injected at one end of the conductor will transmit to the other end. This transmission function can be expressed in terms of the Green's functions of the conductors and of its coupling to the leads as (Lee and Joannopoulos, 1981a, 1981b)

$$\mathcal{T} = \mathrm{Tr}(\Gamma_L G_C^r \Gamma_R G_C^a), \tag{46}$$

where $G_C^{\{r,a\}}$ are the retarded and advanced Green's functions of the conductor, respectively, and $\Gamma_{\{L,R\}}$ are functions that describe the coupling of the conductor to the two leads. To compute the Green's function of the conductor, one starts with the equation for the Green's function of the entire system,

$$(\epsilon - H)G = \mathbb{1}, \tag{47}$$

where $\epsilon = E + i\eta$, with η arbitrarily small, and $\mathbb{1}$ is the identity matrix. The matrix representation of G in a WF basis can be partitioned as

$$\begin{pmatrix} G_L & G_{LC} & G_{LCR} \\ G_{CL} & G_C & G_{CR} \\ G_{LRC} & G_{RC} & G_R \end{pmatrix} = \begin{pmatrix} (\epsilon - H_L) & H_{LC} & 0 \\ H_{LC}^\dagger & (\epsilon - H_C) & H_{CR} \\ 0 & H_{CR}^\dagger & (\epsilon - H_R) \end{pmatrix}^{-1}. \tag{48}$$

We can then write the conductor Green's function as

$$G_C(E) = (\epsilon - H_C - \Sigma_L - \Sigma_R)^{-1}, \tag{49}$$

where the effect of the semi-infinite leads on the conductor is described by the self-energies $\Sigma_{L,R}$, and the coupling functions $\Gamma_{\{L,R\}}$ are obtained from the self-energies as

$$\Gamma_{\{L,R\}} = \mathrm{i}[\Sigma^r_{\{L,R\}} - \Sigma^a_{\{L,R\}}]; \tag{50}$$

In Eq. (50) the advanced self-energy is the Hermitian conjugate of the retarded one, and we solve for the latter. Given that the semi-infinite leads are also made of principal layers, one can construct the self-energies as (Buongiorno Nardelli, 1999)

$$\begin{aligned} \Sigma_L &= H_{LC}^\dagger [\epsilon - H_{00}^L - (H_{01}^L)^\dagger \bar{T}_L]^{-1} H_{LC}, \\ \Sigma_R &= H_{CR} (\epsilon - H_{00}^R - H_{01}^R T_R)^{-1} H_{CR}^\dagger, \end{aligned} \tag{51}$$

where H_{00} describes the intralayer interactions and H_{01} represents the interlayer couplings. The transfer matrices $\bar{T}_{L,R}$ and $T_{L,R}$, defined such that $G_{10} = TG_{00}$ and $G_{00} = \bar{T}G_{10}$, are calculated following the iterative procedure by Sancho, Lopez Sancho, and Rubio (1984). The only inputs are the matrix elements of the Hamiltonian H_{mn} in a localized representation. The accuracy of the results depends on having principal layers that do not couple beyond next neighbors, i.e., having a well-localized basis. The knowledge of the conductor Green's function G_C also gives direct information on the

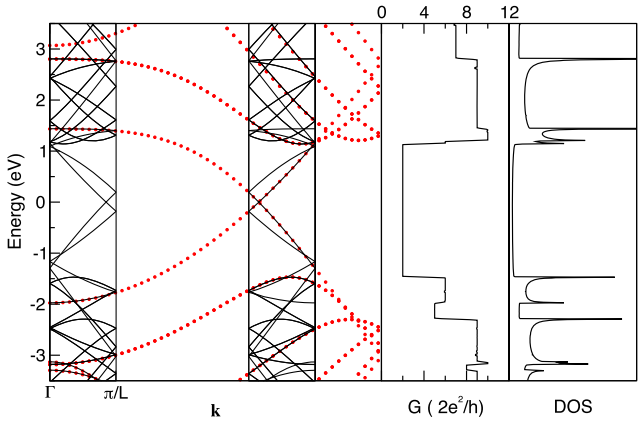

FIG. 8. Left panel: comparison of the band structure for a $(5,5)$ single-wall carbon nanotube. It is calculated in the 20-atom primitive cell with a self-consistent Hamiltonian using five k points along the one-dimensional Brillouin zone ($k = n\pi/L, n = 0, 1, \ldots, 4$) and then diagonalized non-self-consistently everywhere (red dots) or calculated in a supercell 5 times longer. In the latter case the Brillouin zone is 5 times shorter, 5 times more bands are displayed, and the Hamiltonian is consistently obtained using Γ sampling only. While a pseudogap of more than 2 eV is present at Γ, non-self-consistent diagonalization everywhere (solid thin lines) faithfully captures the metallic character of the nanotube. Folding the original bands (red dots) into the smaller Brillouin zone of the supercell also shows perfect agreement between the calculations. These results highlight how disentanglement in the supercell recovers from the empty states at Γ what is needed to capture the character of filled and empty states away from Γ. The center and right panels reinforce this point, showing the ballistic conductance and density of states obtained from the Green's functions calculated using the supercell Wannier functions. Notably, the Van Hove singularities and conductance steps are captured with great accuracy even when the bands edges are at arbitrary points, which highlights the role of MLWFs as effective interpolators and building blocks for the non-self-consistent electronic structure of large-scale nanostructures; see also Lee, Nardelli, and Marzari (2005).

electronic spectrum via the spectral density of the electronic states: $N_C(E) = -(1/\pi)\mathrm{Im}[\mathrm{Tr}G_C(E)]$.

As an example, we take a $(5,5)$ single-wall carbon nanotube described with a supercell containing 100 carbon atoms (5 times the primitive cell); the disentanglement and Wannierization procedure results in 150 sp^2 orbitals and 100 p_z orbitals. This supercell size is large enough to allow for Γ-sampling only in the BZ, and to have negligible overlap with the MLWFs belonging to the next but one supercell. We show in Fig. 8 the results for the band structure, quantum conductance, and density of states as adapted from Lee, Nardelli, and Marzari (2005). The metallic nanotube, notwithstanding its ∼2 eV pseudogap at Γ, shows a band structure in perfect agreement with that obtained from a fine sampling of the BZ and perfect agreement between the steps in conductance and the peaks in the Van Hove singularities, with the maxima and the minima of the band dispersions at arbitrary points in the BZ. While these methodologies based on WFs have been implemented either as an extension of `Wannier90` (Shelley *et al.*, 2011) or as a stand-alone in the WF-based `WanT` code (Ferretti *et al.*, 2012), analogous techniques have been developed for other types of localized orbitals and implemented in simulation codes such as `TranSIESTA` `Atomistix ToolKit` (Brandbyge *et al.*, 2002), `SMEAGOL` (Rocha *et al.*, 2006), `OpenMX` (Ozaki, Nishio, and Kino, 2010), `NEMO5` (Fonseca *et al.*, 2013; Wang *et al.*, 2017, 2021; Sarangapani, Charles, and Kubis, 2022), `nextnano` (Birner *et al.*, 2007), `NanoTCAD ViDES` (Fiori and Iannaccone, 2007; Bruzzone *et al.*, 2014), and `Kwant` (Groth *et al.*, 2014), some of which also provide an interface with the Wannier ecosystem. In addition, we emphasize that different kinds of WFs can be adopted as bases for *ab initio* quantum transport calculations, such as the POWFs (Thygesen, Hansen, and Jacobsen, 2005; Fontana *et al.*, 2021) discussed in Sec. II.D, which have been used at both the DFT (Thygesen and Jacobsen, 2005) and *GW* levels (Thygesen and Rubio, 2008).

E. Berryology

1. Motivation

Berry phases and related quantities are central to the description of the electronic properties of crystals (Xiao, Chang, and Niu, 2010; Vanderbilt, 2018). Here are some representative examples.[3]

(1) The electronic contribution to the electric polarization of an insulator is given by

$$\mathbf{P}_{\mathrm{el}} = -e\sum_{n}^{\mathrm{occ}}\int_{\mathrm{BZ}}\frac{d\mathbf{k}}{(2\pi)^3}\mathbf{A}_{\mathbf{k},nn}, \tag{52}$$

where $-e$ is the electron charge and $\mathbf{A}_{\mathbf{k},nn}$ are diagonal elements of the Berry connection matrix,

$$\mathbf{A}_{\mathbf{k},mn} = i\langle u_{m\mathbf{k}}|\nabla_{\mathbf{k}}u_{n\mathbf{k}}\rangle. \tag{53}$$

(2) The off-diagonal elements of $\mathbf{A}_{\mathbf{k}}$ describe electric-dipole transition moments, allowing the interband optical conductivity to be expressed as

$$\sigma_{ab}(\omega) = \frac{ie^2}{\hbar}\sum_{m,n}\int_{\mathrm{BZ}}\frac{d\mathbf{k}}{(2\pi)^3}(f_{m\mathbf{k}} - f_{n\mathbf{k}}) \times \frac{\varepsilon_{m\mathbf{k}} - \varepsilon_{n\mathbf{k}}}{\varepsilon_{m\mathbf{k}} - \varepsilon_{n\mathbf{k}} - \hbar(\omega + i0^+)}A^a_{\mathbf{k},nm}A^b_{\mathbf{k},mn}, \tag{54}$$

where $f_{n\mathbf{k}}$ is the Fermi-Dirac occupation factor.

(3) The Berry curvature is defined as the curl of the Berry connection

$$\boldsymbol{\Omega}_{n\mathbf{k}} = \nabla_{\mathbf{k}} \times \mathbf{A}_{\mathbf{k},nn} = -\mathrm{Im}\langle\nabla_{\mathbf{k}}u_{n\mathbf{k}}| \times |\nabla_{\mathbf{k}}u_{n\mathbf{k}}\rangle, \tag{55}$$

and its integral over the occupied states gives the intrinsic AHC

$$\sigma_{yx} = \frac{e^2}{\hbar}\int_{\mathrm{BZ}}\frac{d\mathbf{k}}{(2\pi)^3}\sum_n f_{n\mathbf{k}}\Omega^z_{n\mathbf{k}}. \tag{56}$$

(4) The ground-state orbital magnetization reads

$$\mathbf{M}_{\mathrm{orb}} = \int_{\mathrm{BZ}}\frac{d\mathbf{k}}{(2\pi)^3}\sum_n f_{n\mathbf{k}}\left[\mathbf{m}^{\mathrm{orb}}_{n\mathbf{k}} + \frac{e}{\hbar}(\varepsilon_{\mathrm{F}} - \varepsilon_{n\mathbf{k}})\boldsymbol{\Omega}_{n\mathbf{k}}\right], \tag{57}$$

with ε_{F} the Fermi energy and

$$\mathbf{m}^{\mathrm{orb}}_{n\mathbf{k}} = \frac{e}{2\hbar}\mathrm{Im}\langle\nabla_{\mathbf{k}}u_{n\mathbf{k}}| \times (\hat{H}_{\mathbf{k}} - \varepsilon_{n\mathbf{k}})|\nabla_{\mathbf{k}}u_{n\mathbf{k}}\rangle \tag{58}$$

the intrinsic orbital moment of a Bloch state.

(5) To first order in the applied fields $\mathbf{E}$ and $\mathbf{B}$, the semiclassical equations of motion for a wave packet in a Bloch band read

$$\dot{\mathbf{r}} = \frac{1}{\hbar}\nabla_{\mathbf{k}}\tilde{\varepsilon}_{n\mathbf{k}} - \dot{\mathbf{k}} \times \boldsymbol{\Omega}_{n\mathbf{k}}, \tag{59a}$$

$$\dot{\mathbf{k}} = -\frac{e}{\hbar}\mathbf{E} - \frac{e}{\hbar}\dot{\mathbf{r}} \times \mathbf{B}, \tag{59b}$$

where

$$\tilde{\varepsilon}_{n\mathbf{k}} = \varepsilon_{n\mathbf{k}} - (\mathbf{m}^{\mathrm{spin}}_{n\mathbf{k}} + \mathbf{m}^{\mathrm{orb}}_{n\mathbf{k}}) \cdot \mathbf{B} \tag{60}$$

is the Zeeman-shifted band energy.

The motivation to apply Wannier interpolation to Berry-type quantities came from pioneering *ab initio* calculations of the AHC in the ferromagnets $SrRuO_3$ (Fang *et al.*, 2003) and bcc Fe (Yao *et al.*, 2004), which revealed the integrand of Eq. (56) to be strongly peaked near avoided crossings between occupied and empty bands, resulting in the need to sample the BZ over millions of k points to reach convergence. An efficient Wannier-interpolation scheme for evaluating the AHC was developed by Wang *et al.* (2006). The methodology has since been applied to many other properties.

[3]All formulas are given for spinor bands so that each band carries one electron per k point.

Wannier interpolation of Berry-type quantities was introduced in version 2 of `Wannier90` as part of its postprocessing code `postw90` (Mostofi *et al.*, 2014), with the ability to compute AHC (Wang *et al.*, 2006), interband optical conductivity (Yates *et al.*, 2007), and orbital magnetization (Lopez *et al.*, 2012). The list of available properties has since grown considerably, and more recently the `WannierBerri` code package (Tsirkin, 2021) introduced several methodological improvements, including "pruned FFT" (a combination of fast and slow Fourier transforms) (Markel, 1971; Sorensen and Burrus, 1993) and the use of symmetries and the tetrahedron method for BZ integrals. Other codes also compute Berry-type quantities in different contexts, such as `dynamics-w90` for time-dependent dynamics (dynamics-w90 Collaboration, 2023). We note that some codes, including `WannierTools` (Wu *et al.*, 2018) and `linres` (Železný, 2023), implement some functionalities, but with additional approximations; see the forthcoming discussion of Eq. (66). Consult the documentation of the codes for an up-to-date description of their capabilities.

In the following we outline the basic interpolation strategy for Berry-type quantities, using the off-diagonal Berry connection as an example (the diagonal Berry connection that enters the Berry phase requires a separate treatment; see Sec. III.F). For discussion purposes we adopt the modified phase convention for Bloch sums indicated in Eq. (37).

2. Wannier interpolation of the interband Berry connection

We now evaluate off-diagonal elements of the Berry connection matrix in the Hamiltonian gauge. Inserting Eq. (22), the relation between interpolated Bloch states in the Hamiltonian and Wannier gauges, into Eq. (53), we obtain

$$\mathbf{A}^{\mathrm{H}}_{\mathbf{k}'} = i\mathcal{U}^{\dagger}_{\mathbf{k}'}\boldsymbol{\nabla}_{\mathbf{k}'}\mathcal{U}_{\mathbf{k}'} + \mathcal{U}^{\dagger}_{\mathbf{k}'}\mathbf{A}^{\mathrm{W}}_{\mathbf{k}}\mathcal{U}_{\mathbf{k}'}. \tag{61}$$

Note the extra (first) term compared to the gauge-transformation rule [Eq. (29)] for a lattice-periodic matrix object. Recalling from Eq. (18) that the columns of $\mathcal{U}_{\mathbf{k}'}$ are eigenvectors of $H^{\mathrm{W}}_{\mathbf{k}'}$, the off-diagonal matrix elements of that term can be evaluated from nondegenerate perturbation theory as

$$(\mathcal{U}^{\dagger}_{\mathbf{k}'}\boldsymbol{\nabla}_{\mathbf{k}'}\mathcal{U}_{\mathbf{k}'})_{mn} = \frac{[\mathcal{U}^{\dagger}_{\mathbf{k}'}(\boldsymbol{\nabla}_{\mathbf{k}'}H^{\mathrm{W}}_{\mathbf{k}'})\mathcal{U}_{\mathbf{k}'}]_{mn}}{\varepsilon^{\mathrm{H}}_{n\mathbf{k}'} - \varepsilon^{\mathrm{H}}_{m\mathbf{k}'}}. \tag{62}$$

All quantities on the right-hand side of Eq. (62) can be obtained from Eqs. (17) and (18) starting with $\langle \mathbf{0}i|\hat{H}|\mathbf{R}j\rangle$ and $\boldsymbol{\tau}_j = \langle \mathbf{0}j|\hat{\mathbf{r}}|\mathbf{0}j\rangle$ [the latter appears in the modified phase factors in Eq. (37)]. For the second term in Eq. (61), we also need

$$\mathbf{A}^{\mathrm{W}}_{\mathbf{k}',ij} = \sum_{\mathbf{R}} e^{i\mathbf{k}'\cdot(\mathbf{R}+\boldsymbol{\tau}_j-\boldsymbol{\tau}_i)}\mathbf{d}_{ij}(\mathbf{R}), \tag{63}$$

which follows from inserting the Bloch sum [Eq. (20)] with the modified phase factors into Eq. (53). In Eq. (63) $\mathbf{d}_{ij}(\mathbf{R})$ are the off-diagonal matrix elements of $\hat{\mathbf{r}}$ in the Wannier basis, that is,

$$\langle \mathbf{0}i|\hat{\mathbf{r}}|\mathbf{R}j\rangle = \delta_{\mathbf{R},\mathbf{0}}\delta_{ij}\boldsymbol{\tau}_j + \mathbf{d}_{ij}(\mathbf{R}). \tag{64}$$

The matrix elements $\langle \mathbf{0}i|\hat{H}|\mathbf{R}j\rangle$ are evaluated using Eq. (16), and the corresponding procedure for $\langle \mathbf{0}i|\hat{\mathbf{r}}|\mathbf{R}j\rangle$ is as follows. To begin, we can use Eq. (6a) to write $\langle \mathbf{0}i|\hat{\mathbf{r}}|\mathbf{R}j\rangle$ as $(1/N)\sum_{\mathbf{k}} e^{-i\mathbf{k}\cdot\mathbf{R}}A^{\mathrm{W}}_{\mathbf{k},ij}$. Since the Bloch functions are smooth in the Wannier gauge, $\mathbf{A}^{\mathrm{W}}_{\mathbf{k},ij}$ can be evaluated on the *ab initio* grid by discretizing the k derivative appearing in Eq. (53). Adopting the finite-difference scheme described by Marzari and Vanderbilt (1997) and Mostofi *et al.* (2008), we obtain

$$\langle \mathbf{0}i|\hat{\mathbf{r}}|\mathbf{R}j\rangle = \frac{i}{N}\sum_{\mathbf{k}} e^{-i\mathbf{k}\cdot\mathbf{R}}\sum_{\mathbf{b}} w_b\mathbf{b}\sum_{m,n} V^{*}_{\mathbf{k},mi}M^{(\mathbf{k},\mathbf{b})}_{mn}V_{\mathbf{k}+\mathbf{b},nj}, \tag{65}$$

where $\mathbf{b}$ are vectors connecting neighboring grid points, w_b are appropriately chosen weights, $M^{(\mathbf{k},\mathbf{b})}$ are the overlap matrices defined by Eq. (12), and $V_{\mathbf{k}}$ are the Wannierization matrices in Eq. (6b). Since the overlap matrices were computed in preparation of the WF construction procedure and the Wannierization matrices were obtained at the end of that procedure, both are readily available.

Once $\langle \mathbf{0}i|\hat{H}|\mathbf{R}j\rangle$ and $\langle \mathbf{0}i|\hat{\mathbf{r}}|\mathbf{R}j\rangle$ have been tabulated, the interband Berry connection can be evaluated using Eqs. (61)–(63), with the matrices $\mathcal{U}_{\mathbf{k}'}$ therein (along with the interpolated energy eigenvalues) given by Eq. (18). Finally, the Berry connection and energy eigenvalues are inserted into Eq. (54) to obtain the interband optical conductivity (Yates *et al.*, 2007).

Equation (65) entails a numerical error of the order of $(\Delta k)^2$, where Δk is the *ab initio* mesh spacing (Marzari and Vanderbilt, 1997; Mostofi *et al.*, 2008). The direct real-space mesh integration method mentioned after Eq. (16) should be free of such errors, but it is not as practical in the context of k-space Wannierization schemes. It is therefore desirable to develop improved discretized k-space formulas for $\langle \mathbf{0}i|\hat{\mathbf{r}}|\mathbf{R}j\rangle$ and the related matrix elements. A higher-order generalization of the discretization scheme of Marzari and Vanderbilt (1997) and Mostofi *et al.* (2008) was recently introduced (Cistaro *et al.*, 2023), and further improvements are currently under way (Ghim, 2022; Lihm, 2022).

In empirical tight binding, it is customary to approximate the position matrix elements by dropping the second term in Eq. (64) (Foreman, 2002; Vanderbilt, 2018),

$$\langle \mathbf{0}i|\hat{\mathbf{r}}|\mathbf{R}j\rangle \approx \delta_{\mathbf{R},\mathbf{0}}\delta_{ij}\boldsymbol{\tau}_j. \tag{66}$$

In Eq. (66) and when the modified phase convention [Eq. (37)] is used, the matrix $\mathbf{A}^{\mathrm{W}}_{\mathbf{k}'}$ in Eq. (63) vanishes. Equation (61) for $\mathbf{A}^{\mathrm{H}}_{\mathbf{k}'}$ then reduces to its first term, which can be interpreted as the "internal" Berry connection of the tight-binding eigenvectors. This is how tight-binding codes such as `PythTB` evaluate Berry phases and curvatures (Yusufaly, Vanderbilt, and Coh, 2023), which is natural in the context of toy-model calculations.

The aforementioned approximation is more difficult to justify when one uses *ab initio* WFs given that the discarded $\mathbf{d}_{ij}(\mathbf{R})$ matrix elements are readily available, as mentioned; even so, that approximation is made by some codes, including `WannierTools` (Wu *et al.*, 2018) and `linres` (Železný, 2023). The role of intra-atomic $\mathbf{d}_{ij}(\mathbf{R})$ matrix elements in

TABLE I. *Ab initio* matrix elements that are used explicitly in setting up the WF matrix elements needed to perform common interpolation tasks. SHC stands for spin Hall conductivity, an asterisk denotes the seedname specified in the input file of `Wannier90`, QE represents `Quantum ESPRESSO`, $\mathbf{A}_\mathbf{k}$ is the Berry connection or electric-dipole matrix [Eq. (53)], $\mathbf{\Omega}_\mathbf{k}$ is the Berry curvature [Eq. (55)], $\mathbf{m}_\mathbf{k}^{\mathrm{orb}}$ is the intrinsic orbital magnetic dipole [Eq. (58)], and $q_\mathbf{k}^{ab}$ is the intrinsic electric quadrupole [for the matrix definitions of $\mathbf{m}_\mathbf{k}^{\mathrm{orb}}$ and $q_\mathbf{k}^{ab}$, see Pozo Ocaña and Souza (2023)]. The optical conductivity [Eq. (54)] in the electric-dipole approximation involves $\varepsilon_{n\mathbf{k}}$ and $\mathbf{A}_\mathbf{k}$, the AHC [Eq. (56)] involves $\varepsilon_{n\mathbf{k}}$ and $\mathbf{\Omega}_\mathbf{k}$, and the orbital magnetization [Eq. (57)] involves $\varepsilon_{n\mathbf{k}}$, $\mathbf{\Omega}_\mathbf{k}$, and $\mathbf{m}_\mathbf{k}^{\mathrm{orb}}$. Spatially dispersive responses such as natural optical activity depend on $\varepsilon_{n\mathbf{k}}$, $\mathbf{A}_\mathbf{k}$, $\mathbf{m}_\mathbf{k}^{\mathrm{orb}}$, $\mathbf{m}_\mathbf{k}^{\mathrm{spin}}$, and $q_\mathbf{k}^{ab}$ (Pozo Ocaña and Souza, 2023). The `mmn` and `eig` matrix elements are needed for constructing the (disentangled) WFs, and hence they are used implicitly when interpolating any physical quantity.

Matrix element	`Wannier90` file	Needed for	Implemented in	Computed via `mmn2uHu` from
$\langle u_{m\mathbf{k}}\lvert\hat{H}_\mathbf{k}\rvert u_{n\mathbf{k}}\rangle = \varepsilon_{n\mathbf{k}}\delta_{mn}$	`*.eig`	Transport, optics, $\mathbf{m}_\mathbf{k}^{\mathrm{orb}}$	All	
$\langle u_{m\mathbf{k}}\lvert\hat{\boldsymbol{\sigma}}\rvert u_{n\mathbf{k}}\rangle$	`*.spn`	$\mathbf{m}_\mathbf{k}^{\mathrm{spin}}$	QE, `VASP`	
$\langle u_{m\mathbf{k}}\lvert u_{n\mathbf{k}+\mathbf{b}}\rangle$	`*.mmn`	$\mathbf{A}_\mathbf{k}$, $\mathbf{\Omega}_\mathbf{k}$, $\mathbf{m}_\mathbf{k}^{\mathrm{orb}}$, $q_\mathbf{k}^{ab}$, SHC	All	
$\langle u_{m\mathbf{k}+\mathbf{b}_1}\lvert\hat{H}_\mathbf{k}\rvert u_{n\mathbf{k}+\mathbf{b}_2}\rangle$	`*.uHu`	$\mathbf{m}_\mathbf{k}^{\mathrm{orb}}$	QE	`*.eig`, `*.mmn`
$\langle u_{m\mathbf{k}+\mathbf{b}_1}\lvert u_{n\mathbf{k}+\mathbf{b}_2}\rangle$	`*.uIu`	$q_\mathbf{k}^{ab}$	QE	`*.mmn`
$\langle u_{m\mathbf{k}}\lvert\hat{\boldsymbol{\sigma}}\hat{H}_\mathbf{k}\rvert u_{n\mathbf{k}+\mathbf{b}}\rangle$	`*.sHu`	SHC in Ryoo, Park, and Souza (2019)	QE	`*.eig`, `*.mmn`, `*.spn`
$\langle u_{m\mathbf{k}}\lvert\boldsymbol{\sigma}\rvert u_{n\mathbf{k}+\mathbf{b}}\rangle$	`*.sIu`		QE	`*.mmn`, `*.spn`

tight-binding calculations of the linear dielectric function was studied by Pedersen, Pedersen, and Kriestensen (2001). Ibañez-Azpiroz, Juan, and Souza (2022) extended that analysis to interatomic matrix elements and nonlinear optical responses using Wannier interpolation. The importance of the $\mathbf{d}_{ij}(\mathbf{R})$ off-diagonal elements for gauge invariance has also been discussed in the context of time-dependent dynamics (Schüler *et al.*, 2021).

3. Other Berry-type quantities

The interpolation of the Berry curvature $\mathbf{\Omega}_\mathbf{k}$ proceeds along similar lines, allowing the computation of AHC from Eq. (56) (Wang *et al.*, 2006), and the procedure can be extended to spin Hall conductivity (SHC) (Qiao *et al.*, 2018; Ryoo, Park, and Souza, 2019) and nonlinear responses. For example, nonlinear optical responses and AHCs involve k derivatives of $\mathbf{A}_\mathbf{k}$ and $\mathbf{\Omega}_\mathbf{k}$, respectively (Aversa and Sipe, 1995; Sodemann and Fu, 2015). In the same way as band derivatives (see Sec. III.C.2), both are conveniently evaluated by Wannier interpolation (Wang, Liu *et al.*, 2017; Ibañez-Azpiroz, Tsirkin, and Souza, 2018; Liu, Tsirkin, and Souza, 2023). To interpolate $\mathbf{A}_\mathbf{k}$, $\mathbf{\Omega}_\mathbf{k}$, and their k derivatives, one needs only $\langle\mathbf{0}i\lvert\hat{H}\rvert\mathbf{R}j\rangle$ and $\langle\mathbf{0}i\lvert\hat{\mathbf{r}}\rvert\mathbf{R}j\rangle$, but other quantities require additional matrix elements.[4] For example, the orbital moment in Eq. (58) requires $\langle\mathbf{0}i\lvert\hat{H}(\hat{\mathbf{r}}-\mathbf{R})\rvert\mathbf{R}j\rangle$ and $\langle\mathbf{0}i\lvert\hat{r}_a\hat{H}(\hat{r}-R)_b\rvert\mathbf{R}j\rangle$ (Lopez *et al.*, 2012). While the former can be evaluated on the *ab initio* grid using the same ingredients entering Eqs. (16) and (65) for $\langle\mathbf{0}i\lvert\hat{H}\rvert\mathbf{R}j\rangle$ and $\langle\mathbf{0}i\lvert\hat{\mathbf{r}}\rvert\mathbf{R}j\rangle$, the latter also requires $\langle u_{m\mathbf{k}+\mathbf{b}_1}\lvert\hat{H}_\mathbf{k}\rvert u_{n\mathbf{k}+\mathbf{b}_2}\rangle$, which must be calculated separately (Lopez *et al.*, 2012). As in the case of Eq. (61) for $\mathbf{A}_{\mathbf{k}'}$, the resulting interpolation formula contains an internal term analogous to Eq. (58) itself but expressed in terms of the TB eigenvectors and Hamiltonian. That term can be evaluated from $\langle\mathbf{0}i\lvert\hat{H}\rvert\mathbf{R}j\rangle$ and $\boldsymbol{\tau}_j$ alone, but it leaves out important atomiclike contributions that are encoded in the other matrix elements needed for a full calculation (Lopez *et al.*, 2012; Nikolaev and Solovyev, 2014).

The *ab initio* matrix elements needed for various interpolation tasks are listed in Table I. The files `*.eig` and `*.mmn` are already required for constructing the WFs, and therefore they are provided by the interface code of every *ab initio* code that is compatible with `Wannier90`. The file `*.spn` is provided by the interface of both `Quantum ESPRESSO` and `VASP`. As for the other matrix elements listed in Table I, at present they are implemented only in `pw2wannier90.x`, the interface of `Quantum ESPRESSO`.

As a work-around for obtaining these quantities from the output of other *ab initio* engines, one can resort to a sum-over-states procedure. For example, the `uHu` matrix elements may be expressed as

$$\langle u_{m\mathbf{k}+\mathbf{b}_1}\lvert\hat{H}_\mathbf{k}\rvert u_{n\mathbf{k}+\mathbf{b}_2}\rangle \approx \sum_{l}^{l_{\max}}\langle u_{m\mathbf{k}+\mathbf{b}_1}\lvert u_{l\mathbf{k}}\rangle\varepsilon_{l\mathbf{k}}\langle u_{l\mathbf{k}}\lvert u_{n\mathbf{k}+\mathbf{b}_2}\rangle \quad (67)$$

in terms of the energy eigenvalues and overlap matrices, and the relevant matrices for spin Hall conductivity can be similarly obtained (Qiao *et al.*, 2018). Since the summation is done before Wannierization, the number of states $l_{\max}$ included in the non-self-consistent *ab initio* calculation can be systematically increased until the desired level of convergence is reached.

The aforementioned procedure is implemented for `uHu`, `uIu`, `sHu`, and `sIu` in the utility[5] `mmn2uHu` provided with the `WannierBerri` code package (Tsirkin, 2021). Besides its use as a work-around, it can serve as a benchmark for testing future implementations of those matrix elements in various interface codes between *ab initio* and Wannier engines.

[4]By explicitly plugging the Bloch sum of Eq. (20) into the rhs of Eq. (55), one may think that a matrix element $\langle\mathbf{0}i\lvert\hat{r}_a\hat{r}_b\rvert\mathbf{R}j\rangle$ is needed. However, this term is symmetric under the exchange of a and b; therefore, it does not contribute to the cross product, as shown by Wang *et al.* (2007).

[5]The implementation is described in the `WannierBerri` documentation, which is available at https://docs.wannier-berri.org/en/master/docs/mmn2uHu.html.

F. Topological invariants and related properties

The topological aspects of band theory have been intensively studied over the past two decades (Hasan and Kane, 2010; Vanderbilt, 2018), and *ab initio* calculations have been central to that effort (Wang and Zhang, 2017). They are used to indentify topological materials candidates, to determine topological invariants, and to calculate surface bands that can be compared with angle-resolved photoemission measurements.

WFs feature prominently in topological band theory. For example, quantum anomalous Hall insulators (also known as Chern insulators) (Haldane, 1988) can be defined as 2D systems where it is not possible[6] to construct a set of exponentially localized WFs (Thonhauser and Vanderbilt, 2006; Brouder *et al.*, 2007; Vanderbilt, 2018); this is known as a topological obstruction. More generally, symmetry-protected topological insulators can typically be defined as insulators for which it is not possible to construct a set of WFs spanning the valence bands without breaking the protecting symmetry in the choice of gauge (Soluyanov and Vanderbilt, 2011a; Bradlyn *et al.*, 2017). Prominent examples include 2D quantum spin Hall insulators (Kane and Mele, 2005a, 2005b; Bernevig and Zhang, 2006) and 3D $\mathbb{Z}_2$ topological insulators (Fu, Kane, and Mele, 2007), where the protecting symmetry is time reversal, and topological crystalline insulators, which are instead protected by crystalline symmetries (Fu, 2011).

A second example is the "Wannier spectrum" defined by the centers of hybrid (also known as hermaphrodite) orbitals (Sgiarovello, Peressi, and Resta, 2001) that are Wannier-like along $\hat{\mathbf{z}}$ and Bloch-like along $\hat{\mathbf{x}}$ and $\hat{\mathbf{y}}$; see Fig. 9. The surface energy spectrum $\epsilon_n(k_x, k_y)$ can be continuously deformed into the bulk Wannier spectrum $z_n(k_x, k_y)$ obtained by Wannierizing along the surface normal (Fidkowski, Jackson, and Klich, 2011; Neupert and Schindler, 2018), allowing the topological flow of the surface energy bands to be inferred from that of the bulk Wannier bands (Taherinejad, Garrity, and Vanderbilt, 2014). In some cases the topological indices can be deduced from the Wannier band structure (Gresch *et al.*, 2017; Varnava, Souza, and Vanderbilt, 2020).

WFs also play a more practical role in the study of topological materials, as several of the electronic-structure packages that are commonly used to characterize them rely on a Wannier-TB representation [despite the aforementioned obstruction (Soluyanov and Vanderbilt, 2011a; Bradlyn *et al.*, 2017), topological insulators still afford a Wannier representation provided that the WFs span a few low-lying conduction states along with the valence bands].

In particular, both `PythTB` (PythTB Collaboration, 2023) and `WannierTools` (Wu *et al.*, 2018) work with orthogonal TB models and have the option of importing TB Hamiltonians generated by a Wannier engine using either the `*_hr.dat` or the `*_tb.dat` file format (as mentioned, the latter also includes the matrix elements of the position operator in the Wannier basis and the coordinates of the lattice vectors). The key point is that the Wannierized Hamiltonian preserves the topological features of the original first-principles electronic structure. The identification and characterization of those features can therefore be carried out entirely in the Wannier representation, which is often more convenient and/or more efficient than proceeding directly from the *ab initio* Bloch states.

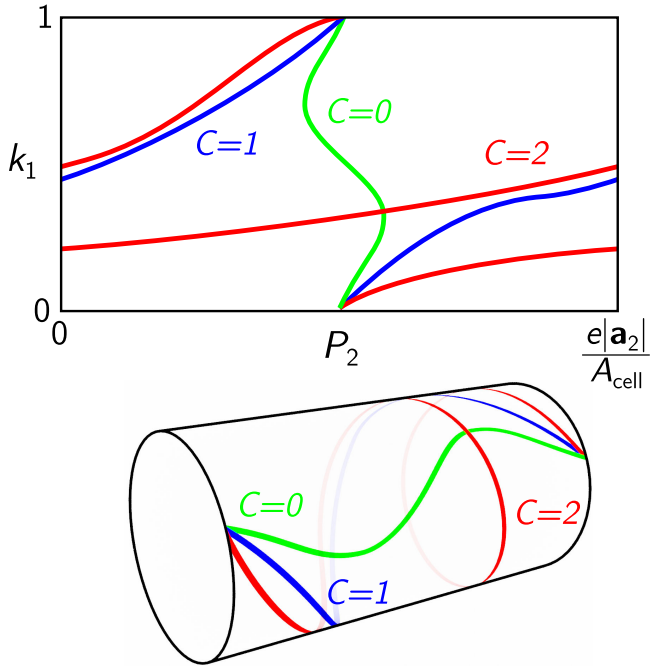

FIG. 9. Sketch of some possible evolutions of hybrid polarization $P_2(k_1)$, i.e., the sum of hybrid Wannier charge centers, across the BZ. The Chern numbers C correspond to different winding numbers. See Gresch *et al.* (2017) for further discussion.

The simplest example of a topological band-structure feature is an isolated touching between a pair of bands, known as a Weyl point (Armitage, Mele, and Vishwanath, 2018; Vanderbilt, 2018). Weyl points are fundamentally different from weak avoided crossings, but most band-interpolation schemes are unable to tell them apart; Wannier interpolation correctly distinguishes between the two. The distinction is rooted in the fact that a Weyl node acts as a monopole source or sink of Berry curvature in k space, allowing it to be associated with a topological invariant known as the chiral charge.

The chiral charge χ [typically ± 1, but sometimes ± 2 or ± 3 (Fang *et al.*, 2012; Tsirkin, Souza, and Vanderbilt, 2017)] can be determined in two different ways: (i) from the quantized Berry-curvature flux through a small surface $\mathcal{S}$ enclosing the Weyl point (Gosálbez-Martínez, Souza, and Vanderbilt, 2015; Vanderbilt, 2018),

$$\int_{\mathcal{S}} \mathbf{\Omega}_{n\mathbf{k}} \cdot \hat{\mathbf{n}} = -2\pi\chi, \tag{68}$$

where $\hat{\mathbf{n}}$ is a unit vector in the direction of $\boldsymbol{\nabla}_{\mathbf{k}} \varepsilon_{n\mathbf{k}}$, and (ii) by evaluating the Berry phase

$$\phi_n(\mathcal{C}) = \oint_{\mathcal{C}} \mathbf{A}_{nn\mathbf{k}} \cdot d\mathbf{k} \tag{69}$$

[6]Recent work (Gunawardana, Turner, and Barnett, 2024) suggested that it might be possible to construct optimally localized WFs even in the presence of nonvanishing Chern numbers, at least for the simple case of one isolated band.

around contours $\mathcal{C}$ at a fixed latitude on an enclosing spherical surface, and then tracking its evolution from zero at the south pole to $2\pi\chi$ at the north pole (Gresch *et al.*, 2017).

The latter procedure is implemented in both `Z2Pack` (Z2Pack Collaboration, 2023) and `WannierTools`. All that is required is the TB Hamiltonian $\langle \mathbf{0}i|\hat{H}|\mathbf{R}j\rangle$, from which one obtains the eigenvectors on a discrete mesh $\{\mathbf{k}_j\}$ of points along each contour. The Berry phase is then evaluated by finite differences from the overlaps between TB eigenvectors on consecutive points along $\mathcal{C}$ as follows (Vanderbilt, 2018):

$$\phi_n^{\mathrm{int}}(\mathcal{C}) = -\mathrm{Im}\,\ln \Pi_j \langle\!\langle u_{n\mathbf{k}_j} \| u_{n\mathbf{k}_{j+1}} \rangle\!\rangle, \tag{70}$$

where $\|u_{n\mathbf{k}_j}\rangle\!\rangle$ denotes a column vector of the matrix $\mathcal{U}_{\mathbf{k}_j}$ defined by Eq. (18). Equation (70) corresponds, in the language of Sec. III.E, to the internal part of the Berry phase [Eq. (69)], which also contains an external part

$$\phi_n^{\mathrm{ext}}(\mathcal{C}) = \sum_j \langle\!\langle u_{n\mathbf{k}_j} \| \mathbf{A}_{\mathbf{k}}^{\mathrm{W}} \| u_{n\mathbf{k}_j} \rangle\!\rangle \cdot \Delta\mathbf{k}, \tag{71}$$

where $\Delta\mathbf{k} = (\mathbf{k}_{j+1} - \mathbf{k}_{j-1})/2$ (Wang *et al.*, 2007). The two parts arise from discretizing the integral along $\mathcal{C}$ of the two terms in Eq. (61) for the interpolated Berry connection. The internal term depends only on $\langle \mathbf{0}i|\hat{H}|\mathbf{R}j\rangle$, while the external one also requires $\langle \mathbf{0}i|\hat{\mathbf{r}}|\mathbf{R}j\rangle$. The 2π indeterminacy in the Berry phase comes from the former, while the latter is single valued and hence does not contribute to the quantized change in the Berry phase from the south to the north pole of a spherical surface. This is why χ can be determined from the TB Hamiltonian alone.

Weyl crossings can occur at arbitrary points in the BZ, which makes it difficult to spot them in the band structure. By allowing energy eigenvalues and band velocities to be quickly evaluated at arbitrary k points, Wannier interpolation provides a practical solution to this problem (Gosálbez-Martínez, Souza, and Vanderbilt, 2015): to locate the degeneracies between bands n and $n+1$, to define a gap function $\varepsilon_{n+1\mathbf{k}} - \varepsilon_{n\mathbf{k}}$, and to search for its minima using a minimization approach such as the conjugate-gradient method starting from a sufficiently dense grid of k points. After discarding local minima where the gap function is above some numerical threshold, one is left with candidate degeneracies that can be further characterized. They include not only point nodes such as Weyl and Dirac nodes (Armitage, Mele, and Vishwanath, 2018) but also nodal lines (Fang *et al.*, 2016; Yang *et al.*, 2018). This procedure is implemented in `WannierTools`.

Topological materials feature characteristic boundary modes that reflect the bulk topology (Hasan and Kane, 2010; Vanderbilt, 2018). In the case of Weyl semimetals, those modes take the form of "Fermi arcs" connecting the projections of bulk Weyl nodes of opposite chirality onto the BZ surface (Armitage, Mele, and Vishwanath, 2018; Vanderbilt, 2018). `PythTB` and `WannierTools` allow a bulk TB model to be terminated along specified directions, thereby creating ribbons or slabs whose boundary modes can then be inspected by plotting the energy bands. `WannierTools` also provides the option of obtaining a surface spectral function from the Green's function calculated for a semi-infinite system. In general, these methods yield boundaries that are the result of a truncation of the Wannier Hamiltonian, where the on-site energies and hoppings between surface (edge) atoms are left unchanged from their bulk value. More broadly, these methods completely neglect any relaxation, charge redistribution, or reconstruction of the surface (edge). Hence, these are crude and unrealistic approximations, and the corresponding calculations do not provide a first-principles description of the boundary electronic structure, even if they derive from a bulk Wannier Hamiltonian that was calculated with first-principles methods. Nevertheless, they provide valuable insights for the prediction of purely topological properties, particularly the existence of topologically protected surface (edge) states such as chiral or helical edge states, surface Dirac cones, and Fermi arcs. While these calculations can support the existence of these boundary states, their precise band dispersion requires the boundary electronic structure to be treated more explicitly, typically through supercell slab (ribbon) simulations with structural optimization.

As mentioned, another useful tool for diagnosing topological behavior is a hybrid representation of the electronic structure in terms of orbitals that are localized in one spatial direction only, remaining extended in the others (Sgiarovello, Peressi, and Resta, 2001). To define these hybrid Wannier functions (HWFs) for lattices of arbitrary symmetry, it is convenient to work in reduced coordinates. Consider a 2D crystal, let $\mathbf{k} = k_1\mathbf{b}_1 + k_2\mathbf{b}_2$, and let $\hat{\mathbf{r}} = \hat{x}_1\mathbf{a}_1 + \hat{x}_2\mathbf{a}_2$. Choosing $\mathbf{b}_2$ as the localization direction, the HWFs are defined as

$$|h_{k_1 ln}\rangle = \frac{1}{N_2}\sum_{k_2} e^{-i2\pi k_2 l}|\psi_{n\mathbf{k}}\rangle, \tag{72}$$

where N_2 is the number of distinct values of k_2 in the BZ and l labels cells along $\mathbf{a}_2$. The topological indices can be determined from the winding of the HWF centers

$$x_{2,k_1 ln} = \langle h_{k_1 ln}|\hat{x}_2|h_{k_1 ln}\rangle. \tag{73}$$

Figure 9 shows possible ways in which the hybrid polarization $P_2(k_1) = -(e|\mathbf{a}_2|/A_{\mathrm{cell}})\sum_n x_{2,k_1 0n}$ (where A_{cell} is the area of the unit cell) can wind across the BZ. For bulk materials the analysis is carried out on high-symmetry BZ planes.

A different physical perspective on HWF centers is provided by the Wilson loop, which is calculated over a closed curve $\mathcal{C}$ in k space, is discretized in L points as

$$\mathcal{W}(\mathcal{C}) = \prod_{i=0}^{L-1} P_{\mathbf{k}_i}^{\mathrm{occ}}, \tag{74}$$

and is a $J \times J$ matrix (Yu *et al.*, 2011) obtained from the product of ground-state projectors $P_{\mathbf{k}_i}^{\mathrm{occ}}$. The Wilson-loop approach was first developed for time-reversal-symmetric systems and later generalized to other topological phases (Alexandradinata, Dai, and Bernevig, 2014; Alexandradinata *et al.*, 2014; Taherinejad, Garrity, and Vanderbilt, 2014; Alexandradinata and Bernevig, 2016).

The two approaches are essentially equivalent (Gresch *et al.*, 2017): the logarithm of the eigenvalues of the Wilson loop at a given k point corresponds to a gauge-invariant set of HWF

centers, which coincide with those obtained from maximal localization (Soluyanov and Vanderbilt, 2011b). Indeed, while the original implementation based on HWFs enforced parallel transport by performing singular value decomposition on each overlap matrix along the line in k space, in the Wilson-loop formalism the full gauge-invariant loop $\mathcal{W}$ is diagonalized. The second approach has been found to converge slightly faster and allows the expectation value of the Wilson-loop eigenstates over symmetry operators to be studied (Gresch *et al.*, 2017; Z2Pack Collaboration, 2023).

This hybrid Wannier (or "Wilson-loop") scheme is implemented in `Z2Pack`; a detailed description of the methodology was given by Gresch *et al.* (2017). In `Z2Pack` the hybrid Wannier centers [Eq. (73)] are obtained from a parallel-transport construction, starting with the overlap matrices [Eq. (12)] (Taherinejad, Garrity, and Vanderbilt, 2014). The same procedure is implemented in `PythTB` and `WannierTools` for Wannier and TB Hamiltonians. The required overlaps are then taken between TB eigenstates, as in Eq. (70) (`Z2Pack` can also operate in this mode). `Z2Pack` (Gresch *et al.*, 2017) works with both Wannier and TB Hamiltonians and acts directly with first-principles engines such as `Quantum ESPRESSO` and `VASP`.

In closing, we bear in mind the different design philosophies of the three packages surveyed in this section. As mentioned in Sec. III.C, `PythTB` (PythTB Collaboration, 2023) was designed with TB "toy models" in mind and was to be used as a pedagogical tool. It enables several geometric and topological quantities to be computed (Berry phases and curvatures, Chern numbers, and hybrid Wannier centers) and allows one to generate ribbons and slabs to expose their boundary modes. Although `PythTB` can also import large Wannier models (which can be truncated internally), the code is not optimized for speed; however, a high-performance `Numba` (Lam, Pitrou, and Seibert, 2015) implementation of `PythTB` better suited for that purpose is available (Numba-PythTB Collaboration, 2023). `WannierTools` (Wu *et al.*, 2018), conversely, is designed primarily to work with large Wannier models and is parallelized using the message passing interface (MPI). Its distinctive features include searching for band degeneracies and plotting surface spectral functions. Finally, `Z2Pack` is focused on the HWF scheme. It is not primarily a "post-Wannier" code, since it can circumvent the need to use a Wannier engine by directly reading the *ab initio* overlap matrices, which can help streamline high-throughput calculations (Marrazzo *et al.*, 2019; Grassano *et al.*, 2023).

While topological invariants are generally introduced for crystalline periodic systems in PBCs, there are a few scenarios that require either the use of open boundary conditions or the adoption of large supercells with Γ-only sampling. In both cases, standard approaches are of no avail. Relevant examples include the study of Anderson (Groth *et al.*, 2009; Jiang *et al.*, 2009; Li *et al.*, 2009) and amorphous topological insulators (Corbae *et al.*, 2023), heterogeneous systems such as trivial and topological junctions (Bianco and Resta, 2011), molecular dynamics simulations, and any other use case that does not fit a small primitive cell with BZ sampling. Among many other approaches [see Corbae *et al.* (2023) for a dedicated overview], single-point sampling (Ceresoli and Resta, 2007; Favata and Marrazzo, 2023) and local markers (Bianco and Resta, 2011; Baù and Marrazzo, 2024a, 2024b) have been introduced to study topology for noncrystalline systems.

Thanks to the use of WFs as a basis set, these techniques can be seamlessly implemented in the same framework for both TB models [like the Haldane (Haldane, 1988) and Kane-Mele models (Kane and Mele, 2005a, 2005b)] and *ab initio* TB models, where the latter are obtained by constructing WFs on top of any electronic-structure calculation including DFT, *GW*, and DMFT (as discussed in Sec. III.C). This strategy has been adopted with the `StraWBerryPy` code (Favata and Marrazzo, 2023; StraWBerryPy Collaboration, 2023; Baù and Marrazzo, 2024a, 2024b), where model or *ab initio* TB Hamiltonians are read and manipulated either through `PythTB` or `TBmodels`. `StraWBerryPy` can then be used to calculate a few single-point and local topological invariants such as the Chern number and the $\mathbb{Z}_2$ invariant, as well as other quantum-geometrical quantities of the electronic structure that are relevant for topological materials.

G. Electron-phonon interactions

1. Methodology

In the past decade we have witnessed a community-wide effort to develop advanced computational approaches and simulation tools for atomistic modeling of function-defining properties of materials. A primary focus of this ongoing research has been the accurate description of electron-phonon (e-ph) interactions from first principles (Giustino, 2017), as they determine many materials properties of technological interest, such as electrical and thermal transport (Li, 2015; Gunst *et al.*, 2016; Lee, Zhou *et al.*, 2018; Macheda and Bonini, 2018; Poncé, Margine, and Giustino, 2018; Brunin *et al.*, 2020a, 2020b; Chaves *et al.*, 2020; Cheng, Zhang, and Liu, 2020; Park *et al.*, 2020; Poncé *et al.*, 2020, 2021; Protik and Broido, 2020; Protik and Kozinsky, 2020; Maliyov, Park, and Bernardi, 2021; Zhou, Park, Timrov *et al.*, 2021; Macheda, Barone, and Mauri, 2022; Poncé, Royo, Gibertini *et al.*, 2023), phonon-assisted light absorption (Noffsinger *et al.*, 2012; Zhang *et al.*, 2022; Bushick and Kioupakis, 2023), phonon-mediated superconductivity (Calandra, Profeta, and Mauri, 2010; Margine and Giustino, 2013; Errea *et al.*, 2020; Lafuente-Bartolome, Gurtubay, and Eiguren, 2020a; Lilia *et al.*, 2022; Lucrezi *et al.*, 2024; Mori *et al.*, 2024; Tomassetti *et al.*, 2024), polaron formation (Sio *et al.*, 2019; Zhou and Bernardi, 2019; Lee *et al.*, 2021; Falletta and Pasquarello, 2022; Lafuente-Bartolome *et al.*, 2022; Sio and Giustino, 2023), and excitonic effects (Chen, Sangalli, and Bernardi, 2020; Antonius and Louie, 2022; Paleari and Marini, 2022; Haber *et al.*, 2023; Dai *et al.*, 2024a, 2024b). This list of references is not exhaustive and is intended to serve only as a starting point for the respective topics.

A comprehensive review of the theory of e-ph interactions in solids from the point of view of *ab initio* calculations was given by Giustino (2017). An important contribution to the e-ph problem was recently made by Stefanucci, Leeuwen, and Perfetto (2023), who developed an *ab initio* many-body quantum theory of electrons and phonons in and out of equilibrium.

There is a well established formalism for computing the *e*-ph matrix elements from first principles using DFPT (Baroni, Giannozzi, and Testa, 1987; Savrasov, 1992; Gonze, 1997; Baroni *et al.*, 2001). Furthermore, a linear-response approach employing the *GW* method, named *GW* perturbation theory (GWPT), was recently proposed to improve the accuracy of the DFPT *e*-ph matrix elements (Li *et al.*, 2019; Li *et al.*, 2024). However, all of the aforementioned materials properties are difficult to evaluate with the desired accuracy using DFPT or GWPT calculations directly due to the prohibitive computational cost. For one to achieve numerical convergence, the *e*-ph matrix elements need to be computed on ultradense electron (k) and phonon (q) BZ grids with 10^6–10^7 points.

Specialized numerical techniques based on Fourier interpolation of the perturbed potential (Eiguren and Ambrosch-Draxl, 2008; Gonze *et al.*, 2020), linear interpolation (Li, 2015), Wannier interpolation (Giustino, Cohen, and Louie, 2007; Giustino *et al.*, 2007; Calandra, Profeta, and Mauri, 2010; Agapito and Bernardi, 2018) or atomic orbital interpolation (Gunst *et al.*, 2016; Agapito and Bernardi, 2018) of the *e*-ph matrix elements, and a Fermi-surface harmonics representation of the *e*-ph matrix elements (Allen, 1976; Eiguren and Gurtubay, 2014; Lafuente-Bartolome, Gurtubay, and Eiguren, 2020b) have been developed to address this convergence problem. In particular, the interpolation of the *e*-ph matrix elements using MLWFs (Marzari *et al.*, 2012) introduced by Giustino, Cohen, and Louie (2007) has proven to be successful for enabling highly accurate and efficient calculations of *e*-ph interactions, and the approach has been implemented within a number of codes (Noffsinger *et al.*, 2010; Poncé *et al.*, 2016; Zhou, Park, Lu *et al.*, 2021; Cepellotti *et al.*, 2022; Lee *et al.*, 2023; Marini *et al.*, 2024). WFs have also been used in the context of downfolding methods to calculate the Coulomb interaction via the constrained random phase approximation (cRPA) (Aryasetiawan *et al.*, 2004) and the *e*-ph interaction via constrained DFPT (Giovannetti *et al.*, 2014; Nomura *et al.*, 2015; Berges *et al.*, 2023), respectively.

We note that an alternative to the computation of the *e*-ph interaction with DFPT is offered by the finite displacement scheme in real space (Gunst *et al.*, 2016; Chaput, Togo, and Tanaka, 2019; Engel *et al.*, 2020, 2022). While this approach requires large supercells to reach convergence and is adiabatic in nature (Poncé *et al.*, 2015; Chaput, Togo, and Tanaka, 2019; Engel *et al.*, 2020, 2022), it has the advantage of being universally applicable to any functional, including hybrid or meta–generalized gradient approximation (meta-GGA) functionals, as well as more complicated exchange-correlation potentials, where higher-order derivatives of the functional are not readily available.

Here we focus on the DFPT approach and outline the interpolation procedure to compute the *e*-ph matrix elements on ultradense meshes using WFs. One first determines the *e*-ph matrix elements in the Bloch representation using the electronic states computed with DFT on the irreducible wedge of a coarse k-point grid and the deformation potentials computed with DFPT on a coarse q-point grid. The *e*-ph matrix element is defined as

$$g_{mn\nu}(\mathbf{k},\mathbf{q}) = \langle \psi_{m\mathbf{k}+\mathbf{q}} | \Delta_{\mathbf{q}\nu} V^{\mathrm{KS}} | \psi_{n\mathbf{k}} \rangle, \tag{75}$$

where $\psi_{n\mathbf{k}}$ and $\psi_{m\mathbf{k}+\mathbf{q}}$ are the KS wave functions of the initial and final Bloch states (with $\mathbf{k}$ the electron wave vector and n the band index), and $\Delta_{\mathbf{q}\nu} V^{\mathrm{KS}}$ is the derivative of the self-consistent potential associated with a phonon with momentum $\mathbf{q}$ and branch index ν. The last quantity can be obtained as

$$\Delta_{\mathbf{q}\nu} V^{\mathrm{KS}} = \sum_{\kappa\alpha p} \left(\frac{\hbar}{2M_\kappa \omega_{\mathbf{q}\nu}} \right)^{1/2} e^{i\mathbf{q}\cdot\mathbf{R}_p} \frac{\partial V^{\mathrm{KS}}}{\partial \tau_{\kappa\alpha p}} e_{\kappa\alpha,\mathbf{q}\nu}, \tag{76}$$

where $\mathbf{R}_p$ is the lattice vector identifying the unit cell p, $\tau_{\kappa\alpha p}$ is the position of atom κ in unit cell p in the Cartesian direction α, M_κ is the mass of atom κ, $\omega_{\mathbf{q}\nu}$ is the phonon frequency, and $e_{\kappa\alpha,\mathbf{q}\nu}$ is the eigendisplacement vector corresponding to atom κ in the Cartesian direction α for a collective phonon mode $\mathbf{q}\nu$.

Then one finds the *e*-ph matrix elements in the Wannier representation,

$$g_{ij\kappa\alpha}(\mathbf{R}_e,\mathbf{R}_p) = \left\langle \mathbf{0}_e i \left| \frac{\partial V^{\mathrm{KS}}}{\partial \tau_{\kappa\alpha p}} \right| \mathbf{R}_e j \right\rangle, \tag{77}$$

where $\mathbf{R}_e$ and $\mathbf{R}_p$ are the Bravais lattice vectors associated with the electron and phonon WS supercells, and $|\mathbf{R}_e j\rangle$ are the MLWFs with index j centered in the cell at $\mathbf{R}_e$. This is done by transforming the *e*-ph matrix elements from the coarse BZ $(\mathbf{k},\mathbf{q})$ grids into the corresponding real-space supercells $(\mathbf{R}_e,\mathbf{R}_p)$ as

$$g_{ij\kappa\alpha}(\mathbf{R}_e,\mathbf{R}_p) = \frac{1}{N_e N_p} \sum_{\mathbf{k},\mathbf{q}} e^{-i(\mathbf{k}\cdot\mathbf{R}_e+\mathbf{q}\cdot\mathbf{R}_p)} \sum_{mn\nu} \left(\frac{\hbar}{2M_\kappa \omega_{\mathbf{q}\nu}} \right)^{1/2} \times V^{\dagger}_{\mathbf{k}+\mathbf{q},im} g_{mn\nu}(\mathbf{k},\mathbf{q}) V_{\mathbf{k},nj} e^{*}_{\kappa\alpha,\mathbf{q}\nu}. \tag{78}$$

In Eq. (78) N_e and N_p are the number of unit cells in the periodic BvK supercells corresponding to the number of k and q points on the coarse electron and phonon grids, respectively, and $V_{\mathbf{k}}$ is the Wannierization matrix introduced in Eq. (6). That matrix is provided by the Wannier engine, while $e_{\kappa\alpha,\mathbf{q}\nu}$ and $\omega_{\mathbf{q}\nu}$ are obtained by diagonalizing the dynamical matrix at wave vector $\mathbf{q}$. In the same spirit as the interpolation of the Hamiltonian discussed in Sec. III.C.1, a WS construction can be used for the interpolation of the electron-phonon matrix elements (Poncé *et al.*, 2021). In this case, the construction is based on three quantities (two Wannier centers and one atomic position).

Finally, when one performs the inverse Fourier transform of Eq. (78), the *e*-ph matrix elements on fine $(\mathbf{k}',\mathbf{q}')$ BZ grids are given by

$$g_{mn\nu}(\mathbf{k}',\mathbf{q}') = \sum_{ep} e^{i(\mathbf{k}'\cdot\mathbf{R}_e+\mathbf{q}'\cdot\mathbf{R}_p)} \sum_{ij\kappa\alpha} \left(\frac{\hbar}{2M_\kappa \omega_{\mathbf{q}'\nu}} \right) \times \mathcal{U}^{\dagger}_{\mathbf{k}'+\mathbf{q}',mi} g_{ij\kappa\alpha}(\mathbf{R}_e,\mathbf{R}_p) \mathcal{U}_{\mathbf{k}',jn} e_{\kappa\alpha,\mathbf{q}'\nu}. \tag{79}$$

In this step it is assumed that the *e*-ph matrix elements outside of the WS supercells defined by the initial coarse grids can be neglected. Prior to computing Eq. (79), one

must find the transformation matrices $\mathcal{U}_{\mathbf{k}',nj}$ given by Eq. (18) and the phonon eigenvectors $e_{\kappa\alpha,\mathbf{q}'\nu}$ and eigenfrequencies $\omega_{\mathbf{q}'\nu}$ for the new set of points $(\mathbf{k}',\mathbf{q}')$, as described by Giustino, Cohen, and Louie (2007).

The accuracy of the Wannier-Fourier interpolation approach depends on the spatial localization of the $g_{ij\kappa\alpha}(\mathbf{R}_e,\mathbf{R}_p)$ matrix elements. Equation (77) can be seen as a hopping integral between two localized WFs, one at $\mathbf{0}_e$ and one at $\mathbf{R}_e$, due to a perturbation caused by the displacement of the atom at $\boldsymbol{\tau}_{\kappa p}$. If the e-ph interactions are short-range in real space, the quantity $g_{ij\kappa\alpha}(\mathbf{R}_e,\mathbf{R}_p)$ decays rapidly with $|\mathbf{R}_e|$ and $|\mathbf{R}_p|$, and it is sufficient to compute the matrix elements on only a small set of $(\mathbf{R}_e,\mathbf{R}_p)$ lattice vectors to fully capture the coupling between electrons and phonons. As discussed by Giustino, Cohen, and Louie (2007) and Giustino (2017), the spatial decay is bound by the limiting cases $g_{ij\kappa\alpha}(\mathbf{R}_e,\mathbf{0}_p)$ and $g_{ij\kappa\alpha}(\mathbf{0}_e,\mathbf{R}_p)$. In the first case the matrix element decays in the variable $\mathbf{R}_e$ at least as fast as the MLWFs. In the second case the matrix element decays with the variable $\mathbf{R}_p$ at the same rate as the screened Coulomb potential generated by the atomic displacements. Thus, the localization of $g_{ij\kappa\alpha}(\mathbf{R}_e,\mathbf{R}_p)$ strongly depends on the dielectric properties of the system. In metals and nonpolar semiconductors and insulators, the screening properties are dictated by Friedel oscillations $|\mathbf{R}_p|^{-4}$ (Fetter and Walecka, 2003) and quadrupole behavior $|\mathbf{R}_p|^{-3}$ (Pick, Cohen, and Martin, 1970), respectively. In polar materials (i.e., materials exhibiting nonzero Born effective charges), the dominant contribution to the potential is the dipole Fröhlich term (Vogl, 1976), which is long-range and decays as $|\mathbf{R}_p|^{-2}$. Therefore, in the case of semiconductors and insulators, the long-range electrostatic fields arising from the nonanalytic behavior of the Coulomb potential in the long-wavelength limit ($\mathbf{q}\to 0$) and the e-ph matrix elements cannot be directly interpolated from a coarse to a fine grid using the Wannier-based interpolation approach.

To address this problem, one separates the e-ph matrix elements into short- ($\mathcal{S}$) and long- ($\mathcal{L}$) range contributions as follows:

$$g_{mn\nu}(\mathbf{k},\mathbf{q}) = g^{\mathcal{S}}_{mn\nu}(\mathbf{k},\mathbf{q}) + g^{\mathcal{L},D}_{mn\nu}(\mathbf{k},\mathbf{q}) + g^{\mathcal{L},Q}_{mn\nu}(\mathbf{k},\mathbf{q}), \tag{80}$$

where the terms on the right-hand side are the short-range, dipole, and quadrupole components. This strategy allows the short-range component to be treated using the previously described Wannier-Fourier interpolation approach once the long-range components have been subtracted from the total matrix elements $g_{mn\nu}(\mathbf{k},\mathbf{q})$. A data-driven compression technique based on a singular value decomposition of the short-range e-ph matrix elements in the Wannier basis was recently developed and was shown to significantly accelerate e-ph calculations while preserving quantitative accuracy (Luo *et al.*, 2024).

Sjakste *et al.* (2015) and Verdi and Giustino (2015) derived the analytic expression for the dipole e-ph matrix, which takes the form

$$\begin{aligned} g^{\mathcal{L},D}_{mn\nu}(\mathbf{k},\mathbf{q}) = i\frac{4\pi}{V_{\text{cell}}}\frac{e^2}{4\pi\epsilon_0}\sum_{\kappa}\left(\frac{\hbar}{2M_\kappa\omega_{\mathbf{q}\nu}}\right)^{1/2} \\ \times\sum_{\mathbf{G}\neq-\mathbf{q}} e^{-i(\mathbf{q}+\mathbf{G})\cdot\boldsymbol{\tau}_\kappa}\frac{(\mathbf{q}+\mathbf{G})\cdot\mathbf{Z}^*_\kappa\cdot\mathbf{e}_{\kappa,\mathbf{q}\nu}}{(\mathbf{q}+\mathbf{G})\cdot\boldsymbol{\epsilon}^\infty\cdot(\mathbf{q}+\mathbf{G})} \\ \times\sum_i V_{\mathbf{k}+\mathbf{q}+\mathbf{G},mi}V^\dagger_{\mathbf{k},in}. \end{aligned} \tag{81}$$

This term is of the order of $1/\mathbf{q}$ and diverges as $\mathbf{q}$ approaches the zone center. In Eq. (81) ϵ_0 is the vacuum permittivity, $\boldsymbol{\epsilon}^\infty$ is the high-frequency dielectric tensor of the material, $\mathbf{G}$ is a reciprocal lattice vector, and $\mathbf{Z}^*_\kappa$ is the Born effective charge tensor of the atom κ. The unitary matrix $V_\mathbf{k}$ is the Wannierization matrix introduced in Eq. (6) and comes from the overlap integral between the KS wave functions $\langle\psi_{m\mathbf{k}+\mathbf{q}}|e^{i\mathbf{q}\cdot\mathbf{r}}|\psi_{n\mathbf{k}}\rangle = \sum_i V_{\mathbf{k}+\mathbf{q},mi}V^\dagger_{\mathbf{k},in}$ in the $\mathbf{q}+\mathbf{G}\to 0$ limit.

The quadrupole contribution is of the order of $|\mathbf{q}|^0$, and the corresponding $g^{\mathcal{L},Q}_{mn\nu}(\mathbf{k},\mathbf{q})$ expression was derived by Brunin *et al.* (2020a, 2020b), Jhalani *et al.* (2020), Park *et al.* (2020), and Poncé, Royo, Stengel *et al.* (2023). In the maximally localized Wannier gauge, $g^{\mathcal{L},Q}_{mn\nu}(\mathbf{k},\mathbf{q})$ can be written as

$$\begin{aligned} g^{\mathcal{L},Q}_{mn\nu}(\mathbf{k},\mathbf{q}) = \frac{4\pi}{V_{\text{cell}}}\frac{e^2}{4\pi\epsilon_0}\sum_{\kappa\alpha}\left(\frac{\hbar}{2M_\kappa\omega_{\mathbf{q}\nu}}\right)^{1/2}\sum_{\mathbf{G}\neq-\mathbf{q}}\frac{e^{-i(\mathbf{q}+\mathbf{G})\cdot\boldsymbol{\tau}_\kappa}e_{\kappa\alpha,\mathbf{q}\nu}}{(\mathbf{q}+\mathbf{G})\cdot\boldsymbol{\epsilon}^\infty\cdot(\mathbf{q}+\mathbf{G})} \\ \times\sum_{\beta\gamma}\left[\frac{1}{2}Q_{\kappa,\alpha\beta\gamma}(q_\beta+G_\beta)(q_\gamma+G_\gamma)\sum_i V_{\mathbf{k}+\mathbf{q}+\mathbf{G},mi}V^\dagger_{\mathbf{k},in}\right. \\ \left. - Z^*_{\kappa,\alpha\beta}(q_\beta+G_\beta)\sum_{ij}V_{\mathbf{k}+\mathbf{q}+\mathbf{G},mi}(q_\gamma+G_\gamma)\left(A^{W,\gamma}_{\mathbf{k},ij}+\langle u^{\text{W}}_{i\mathbf{k}}|V^{\text{Hxc},\mathcal{E}_\gamma}|u^{\text{W}}_{j\mathbf{k}}\rangle\right)V^\dagger_{\mathbf{k},jn}\right], \end{aligned} \tag{82}$$

where $\mathbf{Q}_\kappa$ is the dynamical quadrupole tensor that can be computed using DFPT (Royo and Stengel, 2019), $V^{\text{Hxc},\mathcal{E}_\gamma}(\mathbf{r})$ is the self-consistent potential induced by a uniform electric field $\mathcal{E}_\gamma$ along the Cartesian direction γ (Brunin *et al.*, 2020a; Poncé, Royo, Stengel *et al.*, 2023), $\mathbf{A}^{\text{W}}_{\mathbf{k},ij}$ is the Berry connection introduced in Eq. (63), and $u^{\text{W}}_{j\mathbf{k}}$ is the smooth cell-periodic part of the Bloch wave function in the Wannier gauge ($|u^{\text{W}}_{j\mathbf{k}}\rangle = \sum_n V_{\mathbf{k},jn}|u_{n\mathbf{k}}\rangle$) (Poncé, Royo, Stengel *et al.*, 2023).

Equations (81) and (82) are for the long-range dipole and quadrupole components of the e-ph matrix elements in 3D bulk crystals. Over the past few years, several formalisms have been proposed to treat the long-range contributions in 2D materials (Sohier, Calandra, and Mauri, 2016; Deng *et al.*,

2021; Sio and Giustino, 2022; Zhang and Liu, 2022; Poncé, Royo, Gibertini *et al.*, 2023; Poncé, Royo, Stengel *et al.*, 2023; Sio and Giustino, 2023). For example, a unified description of polar *e*-ph interactions that allows a smooth transition from three to two dimensions was developed by Sio and Giustino (2022). Their formalism reduces to the 3D approach of Sjakste *et al.* (2015) and Verdi and Giustino (2015), and to the 2D approach of Sohier, Calandra, and Mauri (2016) and Deng *et al.* (2021). Another strategy was followed by Zhang and Liu (2022), Poncé, Royo, Gibertini *et al.* (2023), and Poncé, Royo, Stengel *et al.* (2023), who built on the general formalism for treating long-range electrostatic interactions in 2D crystals developed by Royo and Stengel (2021). Poncé, Royo, Gibertini *et al.* (2023) and Poncé, Royo, Stengel *et al.* (2023) showed that the long-range *e*-ph matrix elements have a spurious dependence on the Wannier gauge that can be eliminated by including the contribution associated with the Berry connection in Eq. (82). Therefore, to restore the gauge covariance in the long-wavelength limit, any beyond-Fröhlich Wannier approach should incorporate this term. The contribution from $V^{\mathrm{Hxc},\mathcal{E}}$ term, however, was found to represent less that 0.1% of the total quadrupole correction (Brunin *et al.*, 2020a; Poncé, Royo, Stengel *et al.*, 2023).

2. Codes

`EPW` (Noffsinger *et al.*, 2010; Poncé *et al.*, 2016; EPW Collaboration, 2023; Lee *et al.*, 2023), the first open-source code for the study of *e*-ph interaction using MLWFs, was publicly released in 2010 and has been distributed within the `Quantum ESPRESSO` suite since 2016 (Giannozzi *et al.*, 2017; Quantum ESPRESSO Collaboration, 2023). Several Wannier-based open-source codes exist today to compute physical properties related to *e*-ph interactions such as `PERTURBO` (Zhou, Park, Lu *et al.*, 2021; PERTURBO Collaboration, 2023), `Phoebe` (Cepellotti *et al.*, 2022; Phoebe Collaboration, 2023), `elphbolt` (Protik *et al.*, 2022; Elphbolt Collaboration, 2023), and `EPIq` (EPIq Collaboration, 2023; Marini *et al.*, 2024). At present `EPW`, `PERTURBO`, `Phoebe`, and `EPIq` are all interfaced with `Quantum ESPRESSO` (Giannozzi *et al.*, 2017) to generate the relevant first-principles input data and use `Wannier90` (Pizzi *et al.*, 2020) in stand-alone or library mode to compute the required quantities in the Wannier representation. `elphbolt`, however, relies on `EPW` to generate the required Wannier space information. All codes follow a largely similar workflow to compute *e*-ph matrix elements on fine grids, as now outlined and as summarized in Fig. 10.

(1) The initial step is to perform DFT calculations with `Quantum ESPRESSO` on a full uniform coarse electronic k grid centered at Γ to obtain the band energies and Bloch wave functions. In addition, DFPT calculations with `Quantum ESPRESSO` are carried out on an irreducible coarse q grid to obtain the dynamical matrices and the derivatives of the self-consistent potential with respect to the phonon perturbations. When choosing the electron and phonon grids in Eq. (75), it is necessary that the q-point grid for phonons is commensurate with and smaller than (or equal to) the k-point grid for electrons in order for the wave functions $\psi_{m\mathbf{k}+\mathbf{q}}$ to be mapped onto $\psi_{m\mathbf{k}''+\mathbf{G}}$, where $\mathbf{k}''$ is on the coarse k grid and $\mathbf{G}$ is a reciprocal lattice vector. `Phoebe` and `EPIq` require that the *e*-ph matrix elements on the coarse electron and phonon grids are also computed with `Quantum ESPRESSO` since these quantities are later passed to the two codes. `EPW` and `PERTURBO`, however, compute the *e*-ph matrix elements on the coarse k and q grids internally by reading the files generated from the DFT and DFPT calculations.

(2) Then one must perform a precise Wannierization of the system using `Wannier90` in stand-alone mode with

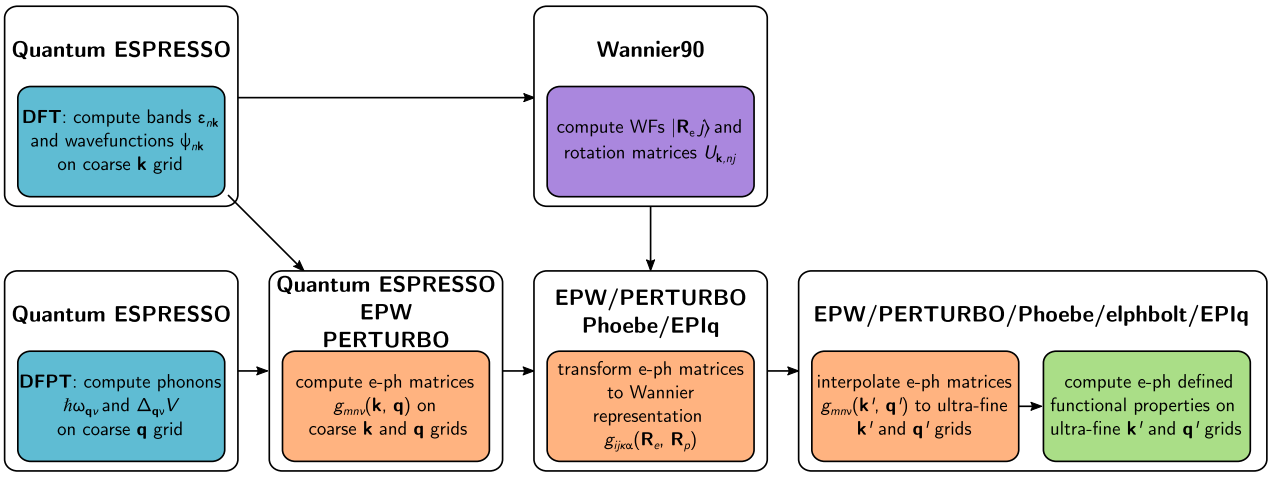

FIG. 10. Workflow to compute *e*-ph interactions on ultrafine grids using WFs. The user performs DFT and DFPT calculations on coarse k- and q-point grids with `Quantum ESPRESSO`. Then the user computes the *e*-ph matrix elements on the coarse grids and transforms them in a localized Wannier basis using the rotation matrices obtained with `Wannier90`. Note that `Phoebe` and `EPIq` read the *e*-ph matrix elements on coarse grids computed with `Quantum ESPRESSO`, while `EPW` and `PERTURBO` compute them internally. Finally, `EPW`, `PERTURBO`, `Phoebe`, and `EPIq` interpolate the band structure, phonon dispersion, and *e*-ph matrix elements on ultrafine k'- and q'-point grids and perform calculations of various materials properties.

PERTURBO, Phoebe, and EPIq or in library mode with EPW. This step produces the MLWFs and the Wannierization matrices $V_{\mathbf{k}}$ that transform the DFT Bloch wave functions into MLWFs.

(3) The next step is to compute the *e*-ph matrix elements on the coarse k and q grids in the Bloch representation and transform them, along with the electronic Hamiltonian and the dynamical matrix, from the Bloch to the Wannier representation. As noted in point 2, Phoebe and EPIq use the *e*-ph matrix elements on the coarse electron and phonon grids computed directly with Quantum ESPRESSO.

(4) The final step is to perform an inverse Fourier transform of the electronic Hamiltonian, dynamical matrix, and *e*-ph matrix elements from the Wannier to the Bloch representation. At this stage, the electronic eigenvalues, phonon frequencies, and *e*-ph matrix elements can be efficiently computed on ultradense k' and q' grids and can be further used to carry out calculations of various materials properties.

To extend the Wannier-based interpolation scheme to systems with long-range *e*-ph contributions, the strategy is as follows. First, the total matrix elements $g_{mn\nu}(\mathbf{k},\mathbf{q})$ are calculated on the coarse k and q grids. Second, the long-range contributions $g^{\mathcal{L},D}_{mn\nu}(\mathbf{k},\mathbf{q})$ and $g^{\mathcal{L},Q}_{mn\nu}(\mathbf{k},\mathbf{q})$ are evaluated on the same coarse grids using Eqs. (81) and (82) and subtracted from $g_{mn\nu}(\mathbf{k},\mathbf{q})$, with the short-range component $g^{\mathcal{S}}_{mn\nu}(\mathbf{k},\mathbf{q})$ left out. Third, the short-range *e*-ph matrix elements are interpolated to ultradense k' and q' grids using the standard approach based on MLWFs. Fourth, the long-range contributions are computed using Eqs. (81) and (82) on the fine k' and q' grids and added back to the short-range component to recover the total $g_{mn\nu}(\mathbf{k}',\mathbf{q}')$ matrix elements. In this last step the rotation matrix $V_{\mathbf{k}}$ given by Eq. (6) is replaced by the transformation matrix $\mathcal{U}^{\dagger}_{\mathbf{k}'}$ given by Eq. (18) in Eqs. (81) and (82).

A wide range of properties can currently be computed with EPW, PERTURBO, Phoebe, elphbolt, and EPIq. A full list of the capabilities for the released version of each code can be found on its website. In particular, EPW computes charge carrier mobility under electric and magnetic fields using the BTE, phonon-mediated superconductivity using the anisotropic Migdal-Eliashberg formalism, phonon-assisted direct and indirect optical absorption using quasidegenerate perturbation theory, small and large polarons without supercells, and zero-point renormalization and temperature dependence of band structures using WFPT (EPW Collaboration, 2023; Lee *et al.*, 2023). EPW also comes with the ZG toolkit for calculations of band-structure renormalization, temperature-dependent optical spectra, temperature-dependent anharmonic phonon dispersions, and anharmonic *e*-ph couplings via the special displacement method (Zacharias and Giustino, 2016, 2020; Zacharias *et al.*, 2023a, 2023b). PERTURBO calculates phonon-limited transport properties using the BTE, ultrafast carrier dynamics, magneto-transport, and high-field electron transport (Zhou, Park, Lu *et al.*, 2021; PERTURBO Collaboration, 2023). PERTURBO is interfaced with the TDEP package (TDEP Collaboration, 2023) that computes temperature-dependent anharmonic phonons. Phoebe provides various tools to predict electron and phonon transport properties at different levels of theory and accuracy, including full scattering matrix BTE solutions such as the relaxons method and models based on the Wigner distribution (Cepellotti *et al.*, 2022; Phoebe Collaboration, 2023). elphbolt solves the coupled electron and phonon BTEs, and the effect of the mutual *e*-ph drag on the electrical and thermal transport coefficients (Protik *et al.*, 2022; Elphbolt Collaboration, 2023). EPIq computes phonon-mediated superconducting properties based on the Migdal-Eliashberg formalism, adiabatic and nonadiabatic phonon frequencies, double-resonant Raman intensities, and excited carrier lifetimes (EPIq Collaboration, 2023; Marini *et al.*, 2024). EPIq is interfaced with the stochastic self-consistent harmonic approximation (SSCHA) (Errea, Calandra, and Mauri, 2013, 2014; Monacelli *et al.*, 2021; SSCHA Collaboration, 2023) in order to calculate *e*-ph interactions in the presence of strong quantum anharmonicity.

H. Beyond-DFT schemes with localized orbitals

While in most cases DFT is the method of choice for electronic ground-state calculations, certain excited-state properties, and even the ground-state properties of certain materials, may require a "beyond-DFT" treatment for accurate first-principles predictions. Two examples are finite-temperature and spectroscopic properties, as observed in direct and inverse photoemission experiments, which cannot be addressed adequately within conventional DFT. Similarly, the complex physics arising from strong local Coulomb interactions in partially filled orbitals is beyond the scope of a single-particle picture, which can manifest itself in an inaccurate description of the material. In such cases more advanced methods are needed. One class of approaches is based on diagrammatic many-body perturbation theory: examples include the *GW* approximation or DMFT; see Sec. III.H.1. Since such methods are often computationally costly and complex, it may be necessary to extract accurate low-energy effective Hamiltonians that are treated using these methods in a postprocessing step. An efficient alternative is to retain the functional character of DFT and apply physically motivated corrections, as in hybrid or Koopmans-compliant functionals; see Sec. III.H.2. In this case the theory is no longer based on a pure functional of the density, but the orbitals themselves or their orbital densities become the key variables. Common to both approaches is the importance of improving the description of local, orbital-dependent physics. This is where WFs come in, providing a useful basis for such applications and supporting the physical understanding with chemical intuition.

1. Dynamical mean-field theory and embedding

Strongly correlated electron systems host a wide variety of physical phenomena, ranging from Mott physics to high-temperature superconductivity to exotic ordered phases (Tokura, Kawasaki, and Nagaosa, 2017). Fundamental to these phenomena is the competition of itinerant versus localized character of electrons, which requires computational methods beyond the single-particle picture. While the representation of electronic states in reciprocal space can be beneficial, the theory of strong local correlations is most naturally formulated in a

real-space basis. A key aspect of many beyond-DFT schemes is therefore the combination of itinerant Bloch states with localized molecular orbitals, which can be elegantly formalized with WFs (Lechermann *et al.*, 2006).

Beyond-DFT schemes are typically computationally demanding and require a compromise in terms of the number of orbitals that can be treated. Starting with an *ab initio* description of a large number of bands, it is common practice to select a subset of correlated orbitals, such as those describing electronic states in the vicinity of the Fermi level, using projector functions. The result is a so-called downfolded model, which contains only the relevant degrees of freedom (Kotliar *et al.*, 2006). It divides the total system into a subspace of localized orbitals, for which a higher-level method is used, and the remaining KS states, for which the single-particle description within DFT accurately reflects the physics. The embedding ansatz is further justified by the observation that correlated physics phenomena typically occur on energy scales of meV to a few eV (Chen *et al.*, 2022). For the remainder of this section we focus on DMFT as the higher-level method to solve the downfolded many-body problem, but the concepts can be similarly applied to its extensions (as briefly discussed later) and conceptual other approaches; see Zgid and Gull (2017), Eskridge, Krakauer, and Zhang (2019), Muechler *et al.* (2022), and Sheng *et al.* (2022).

While the multiband Hubbard model studied with DMFT is directly related to TB models, a rigorous formalism based on energy functionals allows the combined approach with *ab initio* methods, as in DFT + DMFT (Kotliar *et al.*, 2006). The development of DFT + DMFT methods and software for strongly correlated materials has seen a large surge in the past few decades (Held, 2007; Pavarini *et al.*, 2011; Paul and Birol, 2019). Routine calculations allow one to compute single-particle spectra (Pavarini *et al.*, 2004; Anisimov *et al.*, 2005; Nekrasov *et al.*, 2006), optical conductivity (Haule *et al.*, 2005; Wissgott *et al.*, 2012), transport (Oudovenko *et al.*, 2006; Zingl *et al.*, 2019) and thermoelectric properties (Arita *et al.*, 2008; Wissgott *et al.*, 2010; Tomczak, Haule, and Kotliar, 2012), electronic Raman scattering (Blesio *et al.*, 2024), and two-particle correlation functions (susceptibilities) (Boehnke *et al.*, 2011; Kuneš, 2011; Park, Haule, and Kotliar, 2011). Recent advances include interactions with core holes as in x-ray absorption and photoemission spectroscopy, as well as resonant inelastic x-ray scattering (Haverkort, Zwierzycki, and Andersen, 2012; Hariki, Uozumi, and Kuneš, 2017; Lüder *et al.*, 2017; Hariki, Winder, and Kuneš, 2018). Furthermore, routines for lattice optimization (Leonov, Anisimov, and Vollhardt, 2014; Haule and Pascut, 2016; Plekhanov, Bonini, and Weber, 2021) and for computing phonon spectra (Koçer *et al.*, 2020) have been formalized. This list of references is by no means exhaustive but is intended to serve as a starting point for the respective topics.

In beyond-DFT methods it is convenient to describe the total system of interacting electrons in a periodic solid in terms of the momentum- and frequency-dependent retarded single-particle Green's function

$$\hat{G}(\mathbf{k},\omega) = [(\omega+\mu)\mathbb{1} - \hat{H}(\mathbf{k}) - \hat{\Sigma}(\mathbf{k},\omega) + i\eta]^{-1}, \tag{83}$$

where μ is the chemical potential and $\hat{H}(\mathbf{k})$ represents the noninteracting Hamiltonian. The frequency- and momentum-dependent electron self-energy is given by $\hat{\Sigma}(\mathbf{k},\omega)$, and η is an infinitesimal positive parameter to ensure physical correctness. For clarity we have omitted the double-counting correction here; see Karolak *et al.* (2010) for an overview. Starting with a DFT-derived downfolded Hamiltonian, the challenge is to compute the corresponding self-energy correction that accounts for dynamical interaction effects. Various approaches can be formalized, but for the purpose of this review we outline the workflow of single-site DMFT (Georges *et al.*, 1996). In DMFT the self-energy becomes a site-local quantity for a given atomic site $\mathcal{R}$ within the unit cell when it is expressed in a localized orbital basis. This approximation is conceptually similar to the DFT + U formalism (Anisimov, Aryasetiawan, and Lichtenstein, 1997), but in DMFT the full frequency dependence of the interaction is taken into account. Following this approach, in the DMFT self-consistency cycle, the local lattice self-energy $\Sigma^{\mathcal{R}}(\omega)$ is approximated by that of an auxiliary quantum impurity problem. The most computationally challenging step of the DMFT loop is typically to find the solution to the impurity problem, which allows a user to infer the impurity self-energy via the Dyson equation. The self-energy is embedded in the Hilbert space of the effective Hamiltonian as

$$\Sigma_{mn}(\mathbf{k},\omega) = \sum_{\mathcal{R},ij} P^{\mathcal{R}*}_{mi}(\mathbf{k})\Sigma^{\mathcal{R}}_{ij}(\omega)P^{\mathcal{R}}_{jn}(\mathbf{k}). \tag{84}$$

Approximating the lattice self-energy in Eq. (83) by the upfolded impurity self-energy becomes exact for infinite connectivity of the lattice (Metzner and Vollhardt, 1989; Georges and Kotliar, 1992). The projector functions $P^{\mathcal{R}}_{jn}(\mathbf{k})$ in Eq. (84) encode the basis transformation from band to orbital basis, i.e., from $|\psi_{n\mathbf{k}}\rangle$, with the band index n and the wave vector $\mathbf{k}$, to $|\psi^{\mathrm{W}}_{\mathcal{R}_j\mathbf{k}}\rangle$, with the orbital index j at site $\mathcal{R}$ (i.e., j is an intrasite index here),

$$P^{\mathcal{R}}_{jn}(\mathbf{k}) = \langle \psi^{\mathrm{W}}_{\mathcal{R}_j\mathbf{k}} | \psi_{n\mathbf{k}} \rangle. \tag{85}$$

The local Green's function is then computed as $G^{\mathrm{loc},\mathcal{R}}_{ij}(\omega) = \frac{1}{N}\sum_{\mathbf{k},mn} P^{\mathcal{R}}_{im}(\mathbf{k})G_{mn}(\mathbf{k},\omega)P^{\mathcal{R}*}_{nj}(\mathbf{k})$, where N is the total number of k points of the grid. To determine a suitable localized basis set, some DFT + DMFT codes use projections on atomic orbitals, whereas others rely on `Wannier90` directly for a simple and user-friendly interface. While the two approaches are conceptually similar [for a more detailed overview, see Chen *et al.* (2022)], the choice of projectors may affect the results and therefore needs to be carefully analyzed (Karp, Hampel, and Millis, 2021). Note that Eq. (85) assumes that the DFT + DMFT calculation is performed in the band basis in a charge self-consistent mode [i.e., $P(\mathbf{k})$ corresponds to $V_{\mathbf{k}}$ in Eq. (6b)]. However, for one-shot calculations the equations simplify (Beck *et al.*, 2022). Wannier interpolation can be used in the DMFT self-consistent loop for an isolated set of bands or at the TB

level, which is crucial for accurately resolving low-energy physics (Kaye *et al.*, 2023).

Multiple schemes go beyond standard DMFT, but the previous discussion carries over directly to these extensions. Examples include cluster-DMFT approaches (in either real or reciprocal space) (Kotliar *et al.*, 2006) and diagrammatic extensions of the self-energy (Rohringer *et al.*, 2018), as well as nonequilibrium DMFT (Aoki *et al.*, 2014). To improve on some of the shortcomings of the DFT + DMFT method, a better starting point than DFT may be *GW*. The combination of *GW* with DMFT provides a route to including nonlocal effects beyond DFT as well as to formalizing the double-counting correction term (Biermann, 2014).

a. DFT + DMFT *codes*

Based on what was just discussed, we know that a fully integrated DFT + DMFT software suite requires three main components: (1) a DFT implementation (*ab initio* engine) and a routine to construct the localized basis set (for example, a Wannier engine), (2) a Green's function formalism to implement the DMFT equations, and (3) an impurity solver. At present there are several open-source implementations that meet these requirements to a varying degree. On the side of more monolithic, publicly available beyond-DFT codes, there are implementations in, for example, `CASTEP` (Plekhanov *et al.*, 2018), `ABINIT` (Romero *et al.*, 2020), `RSPt` (Grechnev *et al.*, 2007; Di Marco *et al.*, 2009; Thunström *et al.*, 2009), `AMULET` (AMULET Collaboration, 2023), and `eDMFT` (Haule, Yee, and Kim, 2010), which include an implementation of DFT and a downfolding routine, as well as choices of internal and externally linked impurity solvers. `ComDMFT` (Choi *et al.*, 2019), however, interfaces directly with `Wannier90` for the downfolding procedure. All codes support charge self-consistency.

An alternative philosophy is a more modular library approach that focuses on providing the framework for performing DMFT calculations based on input from a DFT calculation. For this purpose most codes directly rely on `Wannier90` to benefit from a generic, robust, and flexible interface independent of the flavor of DFT. Examples include `w2dynamics` (Wallerberger *et al.*, 2019) and `DCore` (Shinaoka *et al.*, 2021), as well as `EDIpack` (Amaricci *et al.*, 2022), `DMFTwDFT` (Singh *et al.*, 2021), and `TRIQS` (Parcollet *et al.*, 2015; Aichhorn *et al.*, 2016; Merkel *et al.*, 2022), with only the last two packages currently supporting charge self-consistency (Schüler *et al.*, 2018; James *et al.*, 2021; Singh *et al.*, 2021; Beck *et al.*, 2022). All packages contain a number of internal and external impurity solvers. A list of all currently available impurity solvers is beyond the scope of this review but can be found on the respective websites.

b. Interaction-parameters codes

As in the DFT + U formalism, the local interaction parameters that enter the Hubbard model in DFT + DMFT calculations must be chosen appropriately. Starting with a local basis set, the Coulomb integrals can be evaluated, ideally taking into account screening processes and the symmetries of the system to simplify the parametrization of the interaction Hamiltonian (Chen *et al.*, 2022). The most widely used approach is the cRPA (Aryasetiawan *et al.*, 2004). Currently, the method is implemented in `ABINIT` (Amadon, Applencourt, and Bruneval, 2014), `SPEX` (Friedrich, Blügel, and Schindlmayr, 2010), `VASP` (Kaltak, 2015), and `RESPACK` (Nakamura *et al.*, 2021). The last three offer the possibility of using WFs, which are constructed either using an internal Wannier engine or via an interface to `Wannier90` (`wan2respack` (Kurita *et al.*, 2023) in the case of `RESPACK`). The usage of WFs in the cRPA method has several benefits, such as a simplified interpretation of the resulting interactions in terms of orbitals, a more compact representation, and the possibility of utilizing Wannier interpolation on the Coulomb kernel; see Rösner *et al.* (2015). The cRPA method calculates the Coulomb interaction as a frequency-dependent response function that can be treated in extended DMFT (Werner and Casula, 2016), and that can also be combined with the frequency-dependent e-ph interaction (Nomura *et al.*, 2015). Alternatively, the interaction parameters are treated as free parameters that must be adjusted to match experimental observables.

c. Postprocessing

Once the solution to the DFT + DMFT scheme is found (charge) self-consistently (see Fig. 11), converged DMFT quantities such as the self-energy, the local Green's function, and the hybridization function allow several physical observables to be computed in postprocessing applications. Depending on the frequency domain in which the impurity solver operates, it may be necessary to use analytic continuation to obtain the self-energy in the real frequency domain (Gubernatis *et al.*, 1991; Wang *et al.*, 2009). Such programs are often included in the respective software packages. Since the postprocessing step is performed only once after convergence, and therefore does not significantly contribute to the overall computational cost, Wannier interpolation (see Sec. III.C) is particularly beneficial at this stage. A standard observable is the lattice or impurity spectral function, which is directly related to photoemission and absorption spectra. Most software packages provide tools for users to compute such quantities routinely. Transport tensors based on

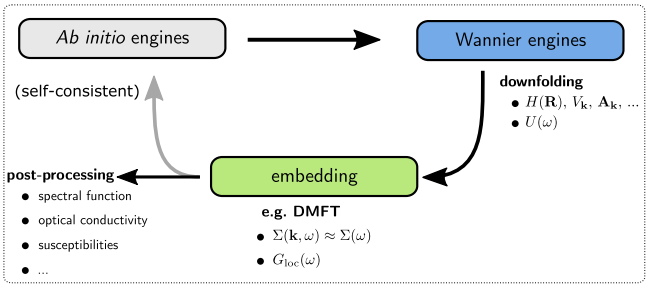

FIG. 11. Typical workflow of the embedding formalism. To begin, the user performs an *ab initio* calculation from which a downfolded model is derived in the basis of localized orbitals. The downfolded model is solved using an appropriate many-body method such as DMFT (depicted). Physical observables can be computed in a postprocessing step. For full self-consistency the cycle is iterated until convergence.

Kubo's linear-response theory (Kubo, 1957), such as optical and thermal conductivities as well as Hall and Seebeck coefficients, can be computed using various software packages, including `eDMFT` (Haule, Yee, and Kim, 2010), `TRIQS/DFTTools` (Aichhorn *et al.*, 2016), `woptic` (Assmann *et al.*, 2016), and `AutoBZ.jl` (Van Muñoz, Beck, and Kaye, 2024). Another option is `LinReTraCe` (Pickem, Maggio, and Tomczak, 2023), which relies on a semi-analytical approach that is valid when a linear expansion of the self-energy is adequate. Tools to evaluate core-level spectroscopies within different levels of approximations are available, for example, in `Quanty` (Haverkort, 2016) and `EDRIXS` (Wang, Fabbris *et al.*, 2019).

2. Koopmans functionals

Koopmans-compliant (KC) functionals (Dabo *et al.*, 2010; Borghi *et al.*, 2014; Colonna *et al.*, 2018, 2019, 2022; Elliott *et al.*, 2019; Zhou and Bernardi, 2019; De Gennaro *et al.*, 2022; Linscott *et al.*, 2023; Marrazzo and Colonna, 2024) are orbital-dependent functionals capable of delivering accurate spectral properties for molecular and extended systems at low computational cost. Note that the KC approach maintains a simple functional formulation while being more accurate than G_0W_0 and comparable to quasiparticle self-consistent GW with vertex correction (Nguyen *et al.*, 2018; Colonna *et al.*, 2019, 2022; Marrazzo and Colonna, 2024), at a cost that is broadly comparable to standard DFT. The simplicity and accuracy of the KC framework rests on three fundamental concepts: linearization, screening, and localization. First, a generalized linearization condition is imposed on each charged excitation: the energy of any orbital must be independent of the occupation of the orbital itself. This implies that the KC total-energy functional is piecewise linear with respect to fractional occupations and essentially implements a generalized definition of the self-interaction-free orbital. Second, electronic screening and orbital relaxation (due to the electron addition-removal process) are taken into account with orbital-dependent screening coefficients, which can be calculated via finite-difference (Nguyen *et al.*, 2018) and linear-response approaches (Colonna *et al.*, 2018, 2022). Finally, the Koopmans compliance condition is imposed on those variational orbitals—i.e., those minimizing the KC energy functional—which are localized. For periodic systems these variational orbitals resemble MLWFs (Colonna *et al.*, 2018, 2019, 2022; Nguyen *et al.*, 2018).

Using WFs as a proxy for variational orbitals has allowed for the development of a Wannier interpolation and unfolding scheme to calculate the band structure from a supercell Koopmans-functional calculation (De Gennaro *et al.*, 2022). In addition, WFs have fostered the development of a Koopmans formulation that operates fully under PBCs and is based on explicit BZ sampling and DFPT (Colonna *et al.*, 2022; Linscott *et al.*, 2023). This Koopmans-Wannier implementation, which goes under the name of `KCW`, is available in the `Quantum ESPRESSO` distribution. It delivers improved scaling with system size and makes band-structure calculations with Koopmans functionals straightforward (Colonna *et al.*, 2022; Linscott *et al.*, 2023; Marrazzo and Colonna, 2024). KC functionals resonate with other efforts aimed at calculating excitation energies where WFs and localized orbitals are often a key ingredient (Anisimov and Kozhevnikov, 2005; Anisimov *et al.*, 2007; Kraisler and Kronik, 2013; Skone, Govoni, and Galli, 2014; Li *et al.*, 2015, 2018; Ma and Wang, 2016; Wing *et al.*, 2021).

I. Interoperability between codes in the ecosystem

1. Library mode for the Wannier engines

When combining two or more codes, various approaches are possible. While the most common approach has been to compile the Wannier engine into a different executable than the *ab initio* code, with data being transferred via files with standardized formats, an alternative approach is to expose the Wannier routines via a library interface, as schematically depicted in Fig. 12. In this second approach a single executable is created, and the main *ab initio* code is responsible for calling the appropriate routines from the Wannier-engine library.

Making sure that the library interface both is easily usable and covers all possible use cases, however, is a nontrivial task. In the specific case of `Wannier90`, for instance, its first release contained a simple interface to allow it to be called a library from another `Fortran` program, with the necessary data being passed by the calling program rather than by file. Over time, however, it became apparent that this original library interface did not provide the full functionality needed by an ecosystem of codes, presenting three main issues. First, the interface was not fully compatible with parallel calling codes, because there was no means to distribute the data and make use of `Wannier90`'s internal parallelism. Second, the use of global module variables meant that `Wannier90` was not thread safe; i.e., a calling program could not call more than one instance of `Wannier90`. Third, there is an issue concerning error handling. Upon detecting an error `Wannier90`

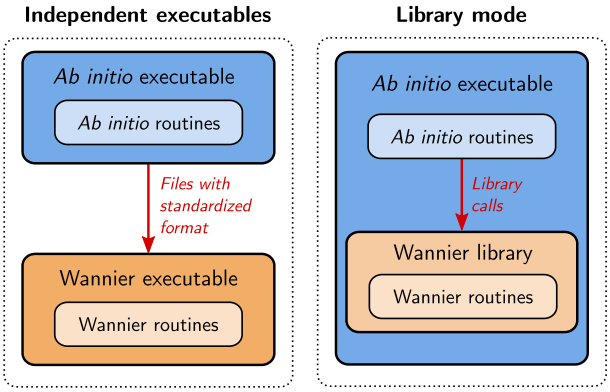

FIG. 12. Different approaches for interaction of the *ab initio* codes with the library routines. Left panel: the *ab initio* codes and the Wannier engine are compiled independently in two different executables. Data exchange happens via files with standardized formats; see also the discussions in Secs. III.B and III.I.2. Right panel: the Wannier engine provides a library mode. The *ab initio* code is linked at compile time to the Wannier library, and a single executable is created. The *ab initio* routines directly call the routines from the Wannier engine via library calls.

would abort, causing the calling program to crash. The desired behavior would instead be to return an error code, allowing the calling program to decide how to handle it (for instance, exiting gracefully or retrying with different parameters). Work to address all three of these issues has been carried out by a team at the Scientific Computing Department of STFC at Daresbury Laboratory, England, in collaboration with Arash A. Mostofi, Jonathan R. Yates, and Giovanni Pizzi. A development version is available in the `Wannier90` GitHub repository and will be merged into a future `Wannier90` release.

2. File I/O generation and parsing

In the first of the previously mentioned approaches, intermediate files (as listed in Table I) are used to decouple the first-principles calculations from the Wannierization step. As discussed, the formats defined by `Wannier90` became the *de facto* standards for the codes in the Wannier-function software ecosystem. For instance, many TB codes can read the so-called `_tb.dat` or `_hr.dat` files (as mentioned, these contain on-site energies, hopping terms, etc.) to further process the Wannier Hamiltonian. In the past few years, many software packages have thus started to implement their own parsers for these I/O files, often focusing only on a specific subset of the file formats relevant for their own use case. However, this leads to a duplication of efforts, keeping in mind that maintaining robust and feature-complete parsers is a nontrivial task. As many of these codes use `Python` as the programming language of choice, such as `TBmodels` (TBmodels Collaboration, 2023), `PythTB` (PythTB Collaboration, 2023), `WannierBerri` (Tsirkin, 2021), and `AiiDA` (Pizzi *et al.*, 2016; Huber *et al.*, 2020; Uhrin *et al.*, 2021), a community effort has been initiated by Jamal I. Mustafa and others to implement a centralized reference set of parsers for the `Wannier90` input-output files[7] in `Python`. The goal of this project is not only to provide a parser library for developers but also to provide a package directly for users, allowing them to easily load and manipulate the `Wannier90` input-output files for their own use case. In addition, we note that part of the `Wannier90` code base already outputs `Python` scripts for postprocessing; one example is the `berry` module, which outputs scripts using the `Matplotlib` library (Hunter, 2007) to plot the Berry curvature. However, these scripts are hard coded into the `Wannier90` codebase as a series of `Fortran write` statements that output `Python` code, which makes them difficult to update and maintain. The aforementioned `Python` library will also facilitate future efforts on moving these postprocessing functions into a dedicated `Python` package, in the hope of smoothening the development experience, as well as allowing users to easily postprocess and visualize the calculation results.

The choice to support and push developments in the `Python` language is driven mostly by its current prevalence and adoption in the field. Indeed, for the goal of interoperability, the choice of programming language is not crucial, while it is essential to have well-defined APIs or file formats. Nevertheless, providing reference implementations avoids duplication efforts in writing file writers and parsers, while aiming to obtain a robust library that can be easily reused and maintained and where bugs can be quickly resolved. To efficiently address this goal, it is useful to select a popular language such as `Python`; this can also facilitate external contributions. Nevertheless, we stress that the concept of a common parsing library is not limited to the `Python` language but rather can be applied to other emerging languages. For example, the `Julia` package `WannierIO.jl` (Qiao, Pizzi, and Marzari, 2023c) provides functions to read and write `Wannier90` file formats and is used by the `Wannier.jl` (Qiao, Pizzi, and Marzari, 2023d) and `DFTK.jl` packages (Herbst, Levitt, and Cancés, 2023) as their I/O backend.

[7]These files are hosted at https://github.com/wannier-developers/wannier90io-python/.

J. Automation, workflows, and high throughput

The diversity of the software ecosystem demonstrates the effectiveness of WFs. However, all methods depend on a robust Wannierization procedure. In the past this was not a straightforward process, since it involves a series of DFT calculations and construction of WFs, and more importantly it also strongly depends on various input parameters (number of WFs, initial projections for MLWFs, energy windows, k-point sampling, etc.). Their selection has often required experience and chemical intuition and has often been a major challenge not only for beginners but also for experienced researchers. Fully automated Wannierizations would make the procedure straightforward and, as a consequence, would allow any researcher to easily use all capabilities of the entire ecosystem while also enabling high-throughput studies for accelerated materials discovery. To this end it became urgent and necessary to perform algorithmic developments on the Wannierization itself, and to implement robust workflows combining multiple software packages in the ecosystem. On the algorithmic side Wannierization should provide well-localized WFs without user input (for initial projections or energy windows, for instance). On the workflow side one wants to orchestrate all of the steps, from the initial DFT calculations to the Wannier-engine executions to the post-processing steps, while dynamically parsing the outputs and generating new inputs. Moreover, the workflow engine should provide a set of well-tested convergence parameters, and it should be able to handle common errors and to automatically restart failed calculations. In addition, an automated Wannierization workflow should ideally be modular and composable to allow better integration with the entire ecosystem. For instance, this has been exploited in the context of automated *GW* calculations with Wannier-interpolated band structures (Bonacci *et al.*, 2023).

Recent development of novel algorithms have largely solved the Wannierization challenge, starting with the SCDM algorithms (Damle, Lin, and Ying, 2015, 2017; Damle and Lin, 2018), which generate initial projections by decomposing the density matrix, to the PDWF (Qiao, Pizzi, and Marzari, 2023b), which uses projectability thresholds on atomic orbitals, rather than energy windows, to select which states to drop, keep frozen, or throw in the disentanglement algorithm. Together with the MRWF (Qiao, Pizzi, and Marzari, 2023a), which uses parallel transport (Gontier,

Levitt, and Siraj-dine, 2019) to automatically construct MLWFs for valence or conduction bands, these approaches remove what had previously been a critical stumbling block.

On the workflow-engine side, several software packages are able to automate the electronic-structure calculations, such as `pymatgen` (Ong *et al.*, 2013), `FireWorks` (Jain *et al.*, 2015), AFLOWπ (Supka *et al.*, 2017), `mkite` (Schwalbe-Koda, 2023), `ASE` (Larsen *et al.*, 2017), `ASR` (Gjerding *et al.*, 2021), and `AiiDA` (Pizzi *et al.*, 2016; Huber *et al.*, 2020; Uhrin *et al.*, 2021). Some of them, such as `ASE` and `AiiDA`, also provide functionalities or workflows to compute WFs. Equipped with automated Wannierization algorithms and robust workflow engines, one can now create workflows for automated Wannierizations. For instance, Gresch *et al.* (2018) implemented `AiiDA` workflows and gathered Wannier-TB models for a group of III-V semiconductor materials. Vitale *et al.* (2020) used the SCDM algorithm together with `AiiDA` workflows, carefully tested convergence parameters, and benchmarked Wannier-interpolation accuracy on a set of 200 structures for entangled bands and a set of 81 structures for isolated bands. Sakai *et al.* (2020) Wannierized 1419 ferromagnetic materials with spin-orbit coupling and computed anomalous Hall and Nernst conductivities to identify high-performance transverse-thermoelectric-conversion materials. Garrity and Choudhary (2021) created a database of Wannier Hamiltonians for 1771 materials. Fontana *et al.* (2021) implemented workflows in `ASE` and Wannierized 30 inorganic monolayer materials using an automated protocol. Finally, Qiao, Pizzi, and Marzari (2023b) used the PDWF to automate the Wannierization, obtaining over 1.3×10^6 MLWFs for more than 20 000 3D inorganics from the Materials Cloud MC3D database (Talirz *et al.*, 2020). They also separately Wannierized these back into the valence and conduction bands of 77 insulators using manifold remixing (Qiao, Pizzi, and Marzari, 2023a). These high-throughput studies not only can expedite materials discoveries but also can help identify challenging cases for the Wannierization algorithm and promote further development of robust and automated Wannierization approaches.

IV. CONCLUSIONS AND PERSPECTIVES

The Wannier-function software ecosystem represents a positive model for interoperability and decentralized code development in electronic-structure simulations; a similar spirit is found in CECAM's Electronic Structure Library (Oliveira *et al.*, 2020). This was made possible both by the nature of the scientific problem and physical quantities involved and by the design choices originally made in `Wannier77` and `Wannier90`, planned early on as Wannierization engines decoupled from the *ab initio* codes used to compute the electronic structure. The availability of a well-documented, well-maintained, and modular open-source Wannier engine has pushed researchers to extend `Wannier90`'s functionalities or, when deemed more practical or efficient, to develop novel packages targeting specific materials properties. The growing availability of postprocessing features ignited a positive loop that further attracted developers from different electronic-structure domains to work and use WFs, thereby strengthening interest in WF-related methods and resulting in the current ecosystem of interoperable software. The ecosystem has been reinforced by the organization of coding weeks and developer workshops, which have proven to be crucial in keeping the community engaged and synced, avoiding a duplication of efforts, and collaborating on code maintenance.

While we could not cover here all the existing applications and codes leveraging WFs—notably, we did not discuss their use in the calculation of magnetic interaction parameters (Nomoto, Koretsune, and Arita, 2020; Yoon *et al.*, 2020; He *et al.*, 2021; Ponet, 2023)—we have outlined some of the most popular applications and summarized how they can be implemented in software packages and workflows to calculate advanced materials properties.

Looking forward, we expect the ongoing efforts in the redesigned `Wannier90`'s library mode to be instrumental in smoothly integrating automated Wannierization procedures within *ab initio* and postprocessing codes, with the benefit of reduced file I/O and code maintenance. As Wannierization becomes increasingly automated, we expect researchers to focus on calculations of complex properties, either through high-level programming of simulation workflows or through the development and extension of postprocessing packages. As a result, even more materials properties will become computationally accessible thanks to WFs and available to the community through the release of dedicated functionalities in either existing or new packages of the ecosystem.

Finally, we comment on two crucial features of an ecosystem, be it biological or software: biodiversity and resilience. A certain level of biodiversity within a software ecosystem, i.e., the existence of multiple software packages with partially overlapping functionalities, can increase its robustness. First, it enables cross verification of different implementations, in the process increasing the reliability of the results and facilitating a rapid identification of bugs. Second, it can ensure that the ecosystem capabilities are not lost if a package goes unmaintained or disappears. This aspect is connected to resilience, i.e., the capability of the ecosystem to deliver functionalities—such as the calculation of materials properties—under the loss of some of its components. This is an especially relevant issue in a scientific community where developers might not be able to guarantee long-term support for their code. We highlight the fact that a software ecosystem might display the same dynamics that can be seen in biological settings, including competition and extinction. While a certain level of competition can result in code improvements regarding feature coverage, efficiency, and robustness, we caution that extreme competition might undermine biodiversity. It is thus important to sustain the work of individual developers who contribute to the progress and maintenance of an active, heterogeneous, and efficient ecosystem, thus encouraging measures to ensure proper scientific recognition. More broadly, the challenge will be to support software development work, which is crucial for the long-term maintenance and integration of heterogeneous software packages. We believe that a diverse, resilient, and open Wannier-function software ecosystem is a major asset for the electronic-structure community in its quest to understand, discover, and design materials.

ACKNOWLEDGMENTS

The authors especially acknowledge the generous and crucial support of CCP9, CECAM, E-CAM, ICTP, IYBSSD, MaX, NCCR MARVEL, Psi-k, SISSA, STFC, and the University of Trieste in the organization of summer schools and developer workshops related to the Wannier-function software ecosystem. Pivotal to the move to the present community model were the 2016 San Sebastián Workshop, which was funded by E-CAM, NCCR MARVEL, and the CECAM JCMaxwell node, and the 2022 ICTP Trieste Wannier Developers Meeting and Wannier Summer School, which was funded by CECAM, ICTP, IYBSSD, MaX, NCCR MARVEL, Psi-k, SISSA, and the University of Trieste, where this work was conceived and organized. A. M. acknowledges support from the ICSC—Centro Nazionale di Ricerca in High Performance Computing, Big Data and Quantum Computing, which was funded by the European Union: NextGenerationEU (CUP Grant No. J93C22000540006, PNRR Investimento No. M4.C2.1.4). S. B. acknowledges the Flatiron Institute, a division of the Simons Foundation. E. R. M. acknowledges support from the U.S. National Science Foundation under Grants No. DMR-2035518 and No. OAC-2103991. N. M. acknowledges early support from the National Science Foundation under Grant No. ASC-96-25885. N. M., G. P., and J. Q. acknowledge support from NCCR MARVEL (a National Centre of Competence in Research, funded by Swiss National Science Foundation Grant No. 205602). A. A. M. acknowledges the European Science Foundation INTELBIOMAT program and the Thomas Young Centre (Grant No. TYC-101) for their support. The work of I. S. and S. S. T. was supported by Grant No. PID2021-129035NB-I00, funded by MCIN/AEI/10.13039/501100011033, and by the IKUR Strategy under the collaboration agreement between the Ikerbasque Foundation and the Material Physics Center on behalf of the Department of Education of the Basque Government. S. S. T. acknowledges support funded by the European Union through the MSCA COFUND program (Grant No. H2020-MSCA-COFUND-2020-101034228-WOLFRAM2). G. P. acknowledges support from Swiss National Science Foundation (SNSF) project funding (Grant No. 200021E_206190 "FISH4DIET"), and from the Open Research Data Program of the ETH Board (project "PREMISE": Open and Reproducible Materials Science Research). The views and opinions expressed here are solely those of the authors and do not necessarily reflect those of the European Union, nor can the European Union be held responsible for them.

REFERENCES

Agapito, Luis A., and Marco Bernardi, 2018, "*Ab initio* electron-phonon interactions using atomic orbital wave functions," Phys. Rev. B **97**, 235146.

Agapito, Luis A., Andrea Ferretti, Arrigo Calzolari, Stefano Curtarolo, and Marco Buongiorno Nardelli, 2013, "Effective and accurate representation of extended Bloch states on finite Hilbert spaces," Phys. Rev. B **88**, 165127.

Aguilera, Irene, Christoph Friedrich, Gustav Bihlmayer, and Stefan Blügel, 2013, "*GW* study of topological insulators Bi_2Se_3, Bi_2Te_3, and Sb_2Te_3: Beyond the perturbative one-shot approach," Phys. Rev. B **88**, 045206.

Aichhorn, Markus, *et al.*, 2016, "TRIQS/DFTTools: A TRIQS application for *ab initio* calculations of correlated materials," Comput. Phys. Commun. **204**, 200–208.

Alexandradinata, A., and B. Andrei Bernevig, 2016, "Berry-phase description of topological crystalline insulators," Phys. Rev. B **93**, 205104.

Alexandradinata, A., Xi Dai, and B. Andrei Bernevig, 2014, "Wilson-loop characterization of inversion-symmetric topological insulators," Phys. Rev. B **89**, 155114.

Alexandradinata, A., Chen Fang, Matthew J. Gilbert, and B. Andrei Bernevig, 2014, "Spin-Orbit-Free Topological Insulators without Time-Reversal Symmetry," Phys. Rev. Lett. **113**, 116403.

Allen, Philip B., 1976, "Fermi-surface harmonics: A general method for nonspherical problems. Application to Boltzmann and Eliashberg equations," Phys. Rev. B **13**, 1416–1427.

Amadon, Bernard, Thomas Applencourt, and Fabien Bruneval, 2014, "Screened Coulomb interaction calculations: cRPA implementation and applications to dynamical screening and self-consistency in uranium dioxide and cerium," Phys. Rev. B **89**, 125110.

Amaricci, A., L. Crippa, A. Scazzola, F. Petocchi, G. Mazza, L. de Medici, and M. Capone, 2022, "EDIpack: A parallel exact diagonalization package for quantum impurity problems," Comput. Phys. Commun. **273**, 108261.

AMULET Collaboration, 2023, computer code AMULET, http://amulet-code.org (accessed on December 17, 2023).

Anderson, E., *et al.*, 1999, *LAPACK Users' Guide*, 3rd ed. (Society for Industrial and Applied Mathematics, Philadelphia).

Anderson, P. W., 1972, "More is different," Science **177**, 393–396.

Anisimov, V. I., F. Aryasetiawan, and A. I. Lichtenstein, 1997, "First-principles calculations of the electronic structure and spectra of strongly correlated systems: The LDA + U method," J. Phys. Condens. Matter **9**, 767–808.

Anisimov, V. I., and A. V. Kozhevnikov, 2005, "Transition state method and Wannier functions," Phys. Rev. B **72**, 075125.

Anisimov, V. I., A. V. Kozhevnikov, M. A. Korotin, A. V. Lukoyanov, and D. A. Khafizullin, 2007, "Orbital density functional as a means to restore the discontinuities in the total-energy derivative and the exchange-correlation potential," J. Phys. Condens. Matter **19**, 106206.

Anisimov, V. I., *et al.*, 2005, "Full orbital calculation scheme for materials with strongly correlated electrons," Phys. Rev. B **71**, 125119.

Antonius, Gabriel, and Steven G. Louie, 2022, "Theory of exciton-phonon coupling," Phys. Rev. B **105**, 085111.

Aoki, Hideo, Naoto Tsuji, Martin Eckstein, Marcus Kollar, Takashi Oka, and Philipp Werner, 2014, "Nonequilibrium dynamical mean-field theory and its applications," Rev. Mod. Phys. **86**, 779–837.

Arita, R., K. Kuroki, K. Held, A. V. Lukoyanov, S. Skornyakov, and V. I. Anisimov, 2008, "Origin of large thermopower in $LiRh_2O_4$: Calculation of the Seebeck coefficient by the combination of local density approximation and dynamical mean-field theory," Phys. Rev. B **78**, 115121.

Armitage, N. P., E. J. Mele, and Ashvin Vishwanath, 2018, "Weyl and Dirac semimetals in three-dimensional solids," Rev. Mod. Phys. **90**, 015001.

Aryasetiawan, F., M. Imada, A. Georges, G. Kotliar, S. Biermann, and A. I. Lichtenstein, 2004, "Frequency-dependent local interactions and low-energy effective models from electronic structure calculations," Phys. Rev. B **70**, 195104.

Assmann, E., P. Wissgott, J. Kuneš, A. Toschi, P. Blaha, and K. Held, 2016, "woptic: Optical conductivity with Wannier functions

and adaptive *k*-mesh refinement," Comput. Phys. Commun. **202**, 1–11.

Aversa, Claudio, and J. E. Sipe, 1995, "Nonlinear optical susceptibilities of semiconductors: Results with a length-gauge analysis," Phys. Rev. B **52**, 14636.

Baroni, S., S. de Gironcoli, A. Dal Corso, and P. Giannozzi, 2001, "Phonons and related properties of extended systems from density-functional perturbation theory," Rev. Mod. Phys. **73**, 515.

Baroni, Stefano, Paolo Giannozzi, and Andrea Testa, 1987, "Green's-Function Approach to Linear Response in Solids," Phys. Rev. Lett. **58**, 1861–1864.

Baù, Nicolas, and Antimo Marrazzo, 2024a, "Theory of local $\mathbb{Z}_2$ topological markers for finite and periodic two-dimensional systems," Phys. Rev. B **110**, 054203.

Baù, Nicolas, and Antimo Marrazzo, 2024b, "Local Chern marker for periodic systems," Phys. Rev. B **109**, 014206.

Beck, Sophie, Alexander Hampel, Olivier Parcollet, Claude Ederer, and Antoine Georges, 2022, "Charge self-consistent electronic structure calculations with dynamical mean-field theory using `Quantum ESPRESSO`, `Wannier90` and `TRIQS`," J. Phys. Condens. Matter **34**, 235601.

Becke, A. D., 1988, "Density-functional exchange-energy approximation with correct asymptotic behavior," Phys. Rev. A **38**, 3098–3100.

Becke, Axel D., 2014, "Perspective: Fifty years of density-functional theory in chemical physics," J. Chem. Phys. **140**, 18A301.

Berges, Jan, Nina Girotto, Tim Wehling, Nicola Marzari, and Samuel Poncé, 2023, "Phonon Self-Energy Corrections: To Screen, or Not to Screen," Phys. Rev. X **13**, 041009.

Berghold, Gerd, Christopher J. Mundy, Aldo H. Romero, Jürg Hutter, and Michele Parrinello, 2000, "General and efficient algorithms for obtaining maximally localized Wannier functions," Phys. Rev. B **61**, 10040–10048.

Bernevig, B. A., and T. L. Hughes, 2013, *Topological Insulators and Topological Superconductors* (Princeton University Press, Princeton, NJ).

Bernevig, B. Andrei, and Shou-Cheng Zhang, 2006, "Quantum Spin Hall Effect," Phys. Rev. Lett. **96**, 106802.

Bezanson, Jeff, Alan Edelman, Stefan Karpinski, and Viral B. Shah, 2017, "`Julia`: A fresh approach to numerical computing," SIAM Rev. **59**, 65–98.

Bianco, Raffaello, and Raffaele Resta, 2011, "Mapping topological order in coordinate space," Phys. Rev. B **84**, 241106.

Bianco, Raffaello, and Raffaele Resta, 2013, "Orbital Magnetization as a Local Property," Phys. Rev. Lett. **110**, 087202.

Biermann, Silke, 2014, "Dynamical screening effects in correlated electron materials—A progress report on combined many-body perturbation and dynamical mean field theory: 'GW + DMFT,'" J. Phys. Condens. Matter **26**, 173202.

Birner, Stefan, Tobias Zibold, Till Andlauer, Tillmann Kubis, Matthias Sabathil, Alex Trellakis, and Peter Vogl, 2007, "`nextnano`: General purpose 3-D simulations," IEEE Trans. Electron Devices **54**, 2137–2142.

Blackford, L. Susan, *et al.*, 2002, "An updated set of basic linear algebra subprograms (`BLAS`)," ACM Trans. Math. Software **28**, 135–151.

Blaha, Peter, Karlheinz Schwarz, Fabien Tran, Robert Laskowski, Georg K. H. Madsen, and Laurence D. Marks, 2020, "`WIEN2k`: An APW + lo program for calculating the properties of solids," J. Chem. Phys. **152**, 074101.

Blesio, Germán, Sophie Beck, Olivier Gingras, Antoine Georges, and Jernej Mravlje, 2024, "Signatures of Hund metal and finite-frequency nesting in Sr_2RuO_4 revealed by electronic Raman scattering," Phys. Rev. Res. **6**, 023124.

Bloch, F., 1929, "Über die Quantenmechanik der Elektronen in Kristallgittern [On the quantum mechanics of electrons in crystal lattices]," Z. Phys. **52**, 555.

Blount, E. I., 1962, "Formalisms of band theory," in *Solid State Physics*, Vol. 13, edited by F. Seitz and D. Turnbull (Elsevier, New York), pp. 305–373.

Boehnke, Lewin, Hartmut Hafermann, Michel Ferrero, Frank Lechermann, and Olivier Parcollet, 2011, "Orthogonal polynomial representation of imaginary-time Green's functions," Phys. Rev. B **84**, 075145.

Bonacci, Miki, Junfeng Qiao, Nicola Spallanzani, Antimo Marrazzo, Giovanni Pizzi, Elisa Molinari, Daniele Varsano, Andrea Ferretti, and Deborah Prezzi, 2023, "Towards high-throughput many-body perturbation theory: Efficient algorithms and automated workflows," npj Comput. Mater. **9**, 74.

Borghi, Giovanni, Andrea Ferretti, Ngoc Linh Nguyen, Ismaila Dabo, and Nicola Marzari, 2014, "Koopmans-compliant functionals and their performance against reference molecular data," Phys. Rev. B **90**, 075135.

Bosoni, Emanuele, *et al.*, 2024, "How to verify the precision of density-functional-theory implementations via reproducible and universal workflows," Nat. Rev. Phys. **6**, 45–58.

Boys, S. F., 1966, "Localized orbitals and localized adjustment functions," in *Quantum Theory of Atoms, Molecules, and the Solid State*, edited by P.-O. Löwdin (Academic Press, New York).

Bradlyn, B., L. Elcoro, J. Cano, M. G. Vergniory, Z. Wang, C. Felser, M. I. Aroyo, and B. A. Bernevig, 2017, "Topological quantum chemistry," Nature (London) **547**, 298.

Brandbyge, Mads, José-Luis Mozos, Pablo Ordejón, Jeremy Taylor, and Kurt Stokbro, 2002, "Density-functional method for nonequilibrium electron transport," Phys. Rev. B **65**, 165401.

Brouder, Christian, Gianluca Panati, Matteo Calandra, Christophe Mourougane, and Nicola Marzari, 2007, "Exponential Localization of Wannier Functions in Insulators," Phys. Rev. Lett. **98**, 046402.

Brunin, Guillaume, Henrique Pereira Coutada Miranda, Matteo Giantomassi, Miquel Royo, Massimiliano Stengel, Matthieu J. Verstraete, Xavier Gonze, Gian-Marco Rignanese, and Geoffroy Hautier, 2020a, "Electron-Phonon beyond Fröhlich: Dynamical Quadrupoles in Polar and Covalent Solids," Phys. Rev. Lett. **125**, 136601.

Brunin, Guillaume, Henrique Pereira Coutada Miranda, Matteo Giantomassi, Miquel Royo, Massimiliano Stengel, Matthieu J. Verstraete, Xavier Gonze, Gian-Marco Rignanese, and Geoffroy Hautier, 2020b, "Phonon-limited electron mobility in Si, GaAs, and GaP with exact treatment of dynamical quadrupoles," Phys. Rev. B **102**, 094308.

Bruzzone, Samantha, Giuseppe Iannaccone, Nicola Marzari, and Gianluca Fiori, 2014, "An open-source multiscale framework for the simulation of nanoscale devices," IEEE Trans. Electron Devices **61**, 48–53.

Buongiorno Nardelli, Marco, 1999, "Electronic transport in extended systems: Application to carbon nanotubes," Phys. Rev. B **60**, 7828–7833.

Buongiorno Nardelli, Marco, Frank T. Cerasoli, Marcio Costa, Stefano Curtarolo, Riccardo De Gennaro, Marco Fornari, Laalitha Liyanage, Andrew R. Supka, and Haihang Wang, 2018, "`PAOFLOW`: A utility to construct and operate on *ab initio* Hamiltonians from the projections of electronic wavefunctions on atomic orbital bases, including characterization of topological materials," Comput. Mater. Sci. **143**, 462–472.

Bushick, Kyle, and Emmanouil Kioupakis, 2023, "Phonon-Assisted Auger-Meitner Recombination in Silicon from First Principles," Phys. Rev. Lett. **131**, 076902.

Calandra, Matteo, Gianni Profeta, and Francesco Mauri, 2010, "Adiabatic and nonadiabatic phonon dispersion in a Wannier function approach," Phys. Rev. B **82**, 165111.

Callaway, Joseph, and A. James Hughes, 1967, "Localized defects in semiconductors," Phys. Rev. **156**, 860–876.

Calzolari, Arrigo, Nicola Marzari, Ivo Souza, and Marco Buongiorno Nardelli, 2004, "*Ab initio* transport properties of nanostructures from maximally localized Wannier functions," Phys. Rev. B **69**, 035108.

Cancès, Éric, Antoine Levitt, Gianluca Panati, and Gabriel Stoltz, 2017, "Robust determination of maximally localized Wannier functions," Phys. Rev. B **95**, 075114.

Cano, Jennifer, Barry Bradlyn, Zhijun Wang, L. Elcoro, M. G. Vergniory, C. Felser, M. I. Aroyo, and B. Andrei Bernevig, 2018, "Building blocks of topological quantum chemistry: Elementary band representations," Phys. Rev. B **97**, 035139.

Carnimeo, Ivan, Stefano Baroni, and Paolo Giannozzi, 2019, "Fast hybrid density-functional computations using plane-wave basis sets," Electron. Struct. **1**, 015009.

CECAM ESL Collaboration, 2023, "The CECAM Electronic Structure Library (ESL)," https://esl.cecam.org (accessed on December 14, 2023).

Cepellotti, Andrea, Jennifer Coulter, Anders Johansson, Natalya S. Fedorova, and Boris Kozinsky, 2022, "`Phoebe`: A high-performance framework for solving phonon and electron Boltzmann transport equations," J. Phys. Mater. **5**, 035003.

Ceresoli, Davide, and Raffaele Resta, 2007, "Orbital magnetization and Chern number in a supercell framework: Single **k**-point formula," Phys. Rev. B **76**, 012405.

Chaput, L., Atsushi Togo, and Isao Tanaka, 2019, "Finite-displacement computation of the electron-phonon interaction within the projector augmented-wave method," Phys. Rev. B **100**, 174304.

Chaves, Anderson S., Alex Antonelli, Daniel T. Larson, and Efthimios Kaxiras, 2020, "Boosting the efficiency of *ab initio* electron-phonon coupling calculations through dual interpolation," Phys. Rev. B **102**, 125116.

Chen, Hanghui, Alexander Hampel, Jonathan Karp, Frank Lechermann, and Andrew J. Millis, 2022, "Dynamical mean field studies of infinite layer nickelates: Physics results and methodological implications," Front. Phys. **10**, 835942.

Chen, Hsiao-Yi, Davide Sangalli, and Marco Bernardi, 2020, "Exciton-Phonon Interaction and Relaxation Times from First Principles," Phys. Rev. Lett. **125**, 107401.

Cheng, Long, Chenmu Zhang, and Yuanyue Liu, 2020, "Why Two-Dimensional Semiconductors Generally Have Low Electron Mobility," Phys. Rev. Lett. **125**, 177701.

Choi, Sangkook, Patrick Semon, Byungkyun Kang, Andrey Kutepov, and Gabriel Kotliar, 2019, "`ComDMFT`: A massively parallel computer package for the electronic structure of correlated-electron systems," Comput. Phys. Commun. **244**, 277–294.

Cistaro, Giovanni, Mikhail Malakhov, Juan José Esteve-Paredes, Alejandro José Uría-Álvarez, Rui E. F. Silva, Fernando Martín, Juan José Palacios, and Antonio Picón, 2023, "Theoretical approach for electron dynamics and ultrafast spectroscopy (EDUS)," J. Chem. Theory Comput. **19**, 333.

Clark, S. J., M. D. Segall, C. J. Pickard, P. J. Hasnip, M. J. Probert, K. Refson, and M. C. Payne, 2005, "First principles methods using `CASTEP`," Z. Kristallogr. **220**, 567–570.

Clausius, R., 1879, *Die Mechanische Behandlung der Electricität* (Vieweg+Teubner Verlag, Berlin).

Clement, Marjory C., Xiao Wang, and Edward F. Valeev, 2021, "Robust Pipek-Mezey orbital localization in periodic solids," J. Chem. Theory Comput. **17**, 7406–7415.

Colonna, Nicola, Riccardo De Gennaro, Edward Linscott, and Nicola Marzari, 2022, "Koopmans spectral functionals in periodic boundary conditions," J. Chem. Theory Comput. **18**, 5435–5448.

Colonna, Nicola, Ngoc Linh Nguyen, Andrea Ferretti, and Nicola Marzari, 2018, "Screening in orbital-density-dependent functionals," J. Chem. Theory Comput. **14**, 2549–2557.

Colonna, Nicola, Ngoc Linh Nguyen, Andrea Ferretti, and Nicola Marzari, 2019, "Koopmans-compliant functionals and potentials and their application to the GW100 test set," J. Chem. Theory Comput. **15**, 1905–1914.

Corbae, Paul, Julia D. Hannukainen, Quentin Marsal, Daniel Muñoz-Segovia, and Adolfo G. Grushin, 2023, "Amorphous topological matter: Theory and experiment," Europhys. Lett. **142**, 16001.

Dabo, Ismaila, Andrea Ferretti, Nicolas Poilvert, Yanli Li, Nicola Marzari, and Matteo Cococcioni, 2010, "Koopmans' condition for density-functional theory," Phys. Rev. B **82**, 115121.

Dai, Zhenbang, Chao Lian, Jon Lafuente-Bartolome, and Feliciano Giustino, 2024a, "Excitonic Polarons and Self-Trapped Excitons from First-Principles Exciton-Phonon Couplings," Phys. Rev. Lett. **132**, 036902.

Dai, Zhenbang, Chao Lian, Jon Lafuente-Bartolome, and Feliciano Giustino, 2024b, "Theory of excitonic polarons: From models to first-principles calculations," Phys. Rev. B **109**, 045202.

Damle, A., and L. Lin, 2018, "Disentanglement via entanglement: A unified method for Wannier localization," Multiscale Model. Simul. **16**, 1392–1410.

Damle, Anil, Antoine Levitt, and Lin Lin, 2019, "Variational formulation for Wannier functions with entangled band structure," Multiscale Model. Simul. **17**, 167–191.

Damle, Anil, Lin Lin, and Lexing Ying, 2015, "Compressed representation of Kohn-Sham orbitals via selected columns of the density matrix," J. Chem. Theory Comput. **11**, 1463–1469.

Damle, Anil, Lin Lin, and Lexing Ying, 2017, "SCDM-k: Localized orbitals for solids via selected columns of the density matrix," J. Comput. Phys. **334**, 1–15.

Dancoff, S. M., 1950, "Non-adiabatic meson theory of nuclear forces," Phys. Rev. **78**, 382–385.

De Gennaro, Riccardo, Nicola Colonna, Edward Linscott, and Nicola Marzari, 2022, "Bloch's theorem in orbital-density-dependent functionals: Band structures from Koopmans spectral functionals," Phys. Rev. B **106**, 035106.

Deng, Tianqi, Gang Wu, Wen Shi, Zicong Marvin Wong, Jian-Sheng Wang, and Shuo-Wang Yang, 2021, "*Ab initio* dipolar electron-phonon interactions in two-dimensional materials," Phys. Rev. B **103**, 075410.

Des Cloizeaux, Jacques, 1964a, "Analytical properties of *n*-dimensional energy bands and Wannier functions," Phys. Rev. **135**, A698–A707.

Des Cloizeaux, Jacques, 1964b, "Energy bands and projection operators in a crystal: Analytic and asymptotic properties," Phys. Rev. **135**, A685–A697.

Dias, Alexandre C., Julian F. R. V. Silveira, and Fanyao Qu, 2023, "`WanTiBEXOS`: A Wannier based tight binding code for electronic band structure, excitonic and optoelectronic properties of solids," Comput. Phys. Commun. **285**, 108636.

Di Marco, I., J. Minár, S. Chadov, M. I. Katsnelson, H. Ebert, and A. I. Lichtenstein, 2009, "Correlation effects in the total energy, the bulk modulus, and the lattice constant of a transition metal:

Combined local-density approximation and dynamical mean-field theory applied to Ni and Mn," Phys. Rev. B **79**, 115111.
Dirac, P. A. M., 1929, "Quantum mechanics of many-electron systems," Proc. R. Soc. A **123**, 714–733.
DiStasio, Jr., Robert A., Biswajit Santra, Zhaofeng Li, Xifan Wu, and Roberto Car, 2014, "The individual and collective effects of exact exchange and dispersion interactions on the *ab initio* structure of liquid water," J. Chem. Phys. **141**, 084502.
Duffin, R. J., 1953, Duke Math. J. **20**, 233.
dynamics-w90 Collaboration, 2023, computer code `dynamics-w90`, https://github.com/michaelschueler/dynamics-w90.
Edmiston, Clyde, and Klaus Ruedenberg, 1963, "Localized atomic and molecular orbitals," Rev. Mod. Phys. **35**, 457–464.
Eiguren, Asier, and Claudia Ambrosch-Draxl, 2008, "Wannier interpolation scheme for phonon-induced potentials: Application to bulk MgB_2, W, and the 1×1 H-covered W(110) surface," Phys. Rev. B **78**, 045124.
Eiguren, Asier, and Idoia G. Gurtubay, 2014, "Helmholtz Fermi surface harmonics: An efficient approach for treating anisotropic problems involving Fermi surface integrals," New J. Phys. **16**, 063014.
Elk Collaboration, 2023, computer code `Elk`, http://elk.sourceforge.net/.
Elliott, Joshua D., Nicola Colonna, Margherita Marsili, Nicola Marzari, and Paolo Umari, 2019, "Koopmans meets Bethe-Salpeter: Excitonic optical spectra without *GW*," J. Chem. Theory Comput. **15**, 3710–3720.
Elphbolt Collaboration, 2023, computer code `elphbolt`, https://github.com/nakib/elphbolt.
Engel, Manuel, Martijn Marsman, Cesare Franchini, and Georg Kresse, 2020, "Electron-phonon interactions using the projector augmented-wave method and Wannier functions," Phys. Rev. B **101**, 184302.
Engel, Manuel, Henrique Miranda, Laurent Chaput, Atsushi Togo, Carla Verdi, Martijn Marsman, and Georg Kresse, 2022, "Zero-point renormalization of the band gap of semiconductors and insulators using the projector augmented wave method," Phys. Rev. B **106**, 094316.
Enkovaara, J., *et al.*, 2010, "Electronic structure calculations with `GPAW`: A real-space implementation of the projector augmented-wave method," J. Phys. Condens. Matter **22**, 253202.
EPIq Collaboration, 2023, computer code `EPIq`, https://the-epiq-team.gitlab.io/epiq-site/.
EPW Collaboration, 2023, computer code `EPW`, https://epw-code.org/.
Errea, Ion, Matteo Calandra, and Francesco Mauri, 2013, "First-Principles Theory of Anharmonicity and the Inverse Isotope Effect in Superconducting Palladium-Hydride Compounds," Phys. Rev. Lett. **111**, 177002.
Errea, Ion, Matteo Calandra, and Francesco Mauri, 2014, "Anharmonic free energies and phonon dispersions from the stochastic self-consistent harmonic approximation: Application to platinum and palladium hydrides," Phys. Rev. B **89**, 064302.
Errea, Ion, *et al.*, 2020, "Quantum crystal structure in the 250-kelvin superconducting lanthanum hydride," Nature (London) **578**, 66.
Eskridge, Brandon, Henry Krakauer, and Shiwei Zhang, 2019, "Local embedding and effective downfolding in the auxiliary-field quantum Monte Carlo method," J. Chem. Theory Comput. **15**, 3949–3959.
Falletta, Stefano, and Alfredo Pasquarello, 2022, "Polarons free from many-body self-interaction in density functional theory," Phys. Rev. B **106**, 125119.
Fang, Chen, Matthew J. Gilbert, Xi Dai, and B. Andrei Bernevig, 2012, "Multi-Weyl Topological Semimetals Stabilized by Point Group Symmetry," Phys. Rev. Lett. **108**, 266802.
Fang, Chen, Hongming Weng, Xi Dai, and Zhong Fang, 2016, "Topological nodal line semimetals," Chin. Phys. B **25**, 117106.
Fang, Zhong, Naoto Nagaosa, Kei S. Takahashi, Atsushi Asamitsu, Roland Mathieu, Takeshi Ogasawara, Hiroyuki Yamada, Masashi Kawasaki, Yoshinori Tokura, and Kiyoyuki Terakura, 2003, "The anomalous Hall effect and magnetic monopoles in momentum space," Science **302**, 92.
Favata, Roberta, and Antimo Marrazzo, 2023, "Single-point spin Chern number in a supercell framework," Electron. Struct. **5**, 014005.
Ferretti, A., A. Calzolari, B. Bonferroni, and R. Di Felice, 2007, "Maximally localized Wannier functions constructed from projector-augmented waves or ultrasoft pseudopotentials," J. Phys. Condens. Matter **19**, 036215.
Ferretti, Andrea, Giuseppe Mallia, Layla Martin-Samos, Giovanni Bussi, Alice Ruini, Barbara Montanari, and Nicholas M. Harrison, 2012, "*Ab initio* complex band structure of conjugated polymers: Effects of hydrid density functional theory and *GW* schemes," Phys. Rev. B **85**, 235105.
Fetter, A. L., and J. D. Walecka, 2003, *Quantum Theory of Many-Particle Systems* (Dover Publications, New York).
Fidkowski, L., T. S. Jackson, and I. Klich, 2011, "Model Characterization of Gapless Edge Modes of Topological Insulators Using Intermediate Brillouin-Zone Functions," Phys. Rev. Lett. **107**, 036601.
Fiori, Gianluca, and Giuseppe Iannaccone, 2007, "Simulation of graphene nanoribbon field-effect transistors," IEEE Electron Device Lett. **28**, 760–762.
Fonseca, J. E., *et al.*, 2013, "Efficient and realistic device modeling from atomic detail to the nanoscale," J. Comput. Electron. **12**, 592–600.
Fontana, Pietro F., Ask H. Larsen, Thomas Olsen, and Kristian S. Thygesen, 2021, "Spread-balanced Wannier functions: Robust and automatable orbital localization," Phys. Rev. B **104**, 125140.
Foreman, Bradley A., 2002, "Consequences of local gauge symmetry in empirical tight-binding theory," Phys. Rev. B **66**, 165212.
Freimuth, F., Y. Mokrousov, D. Wortmann, S. Heinze, and S. Blügel, 2008, "Maximally localized Wannier functions within the FLAPW formalism," Phys. Rev. B **78**, 035120.
Friedrich, Christoph, Stefan Blügel, and Arno Schindlmayr, 2010, "Efficient implementation of the *GW* approximation within the all-electron FLAPW method," Phys. Rev. B **81**, 125102.
Frigo, Matteo, and Steven G. Johnson, 2005, "The design and implementation of FFTW3," Proc. IEEE **93**, 216–231.
Fu, Liang, 2011, "Topological Crystalline Insulators," Phys. Rev. Lett. **106**, 106802.
Fu, Liang, C. L. Kane, and E. J. Mele, 2007, "Topological Insulators in Three Dimensions," Phys. Rev. Lett. **98**, 106803.
Gao, Yang, 2019, "Semiclassical dynamics and nonlinear charge current," Front. Phys. **14**, 33404.
Gao, Yang, Shengyuan A. Yang, and Qian Niu, 2017, "Intrinsic relative magnetoconductivity of nonmagnetic metals," Phys. Rev. B **95**, 165135.
García-Cervera, C. J., Jianfeng Lu, Yulin Xuan, and E. Weinan, 2009, "Linear-scaling subspace-iteration algorithm with optimally localized nonorthogonal wave functions for Kohn-Sham density functional theory," Phys. Rev. B **79**, 115110.
Garrity, Kevin F., and Kamal Choudhary, 2021, "Database of Wannier tight-binding Hamiltonians using high-throughput density functional theory," Sci. Data **8**, 106.
Georges, Antoine, and Gabriel Kotliar, 1992, "Hubbard model in infinite dimensions," Phys. Rev. B **45**, 6479–6483.

Georges, Antoine, Gabriel Kotliar, Werner Krauth, and Marcelo J. Rozenberg, 1996, "Dynamical mean-field theory of strongly correlated fermion systems and the limit of infinite dimensions," Rev. Mod. Phys. **68**, 13–125.

Ghim, Minsu, 2022, "Accurate calculation of Wannier centers and position matrix elements II: Higher-order finite difference," lecture, Wannier 2022 Developers Meeting, Trieste, Italy, 2022, http://video.ictp.it/WEB/2022/2022_05_23-smr3757/2022_05_23-11_20-smr3757.mp4.

Giannozzi, P., *et al.*, 2017, "Advanced capabilities for materials modelling with `Quantum ESPRESSO`," J. Phys. Condens. Matter **29**, 465901.

Giannozzi, Paolo, *et al.*, 2009, "`Quantum ESPRESSO`: A modular and open-source software project for quantum simulations of materials," J. Phys. Condens. Matter **21**, 395502.

Gibertini, Marco, Giovanni Pizzi, and Nicola Marzari, 2014, "Engineering polar discontinuities in honeycomb lattices," Nat. Commun. **5**, 5157.

Giovannetti, Gianluca, Michele Casula, Philipp Werner, Francesco Mauri, and Massimo Capone, 2014, "Downfolding electron-phonon Hamiltonians from *ab initio* calculations: Application to K_3 picene," Phys. Rev. B **90**, 115435.

Giustino, F., 2014, *Materials Modelling Using Density Functional Theory* (Oxford University Press, New York).

Giustino, Feliciano, 2017, "Electron-phonon interactions from first principles," Rev. Mod. Phys. **89**, 015003.

Giustino, Feliciano, Marvin L. Cohen, and Steven G. Louie, 2007, "Electron-phonon interaction using Wannier functions," Phys. Rev. B **76**, 165108.

Giustino, Feliciano, Marvin L. Cohen, and Steven G. Louie, 2010, "*GW* method with the self-consistent Sternheimer equation," Phys. Rev. B **81**, 115105.

Giustino, Feliciano, and Alfredo Pasquarello, 2006, "Mixed Wannier-Bloch Functions for Electrons and Phonons in Periodic Systems," Phys. Rev. Lett. **96**, 216403.

Giustino, Feliciano, Jonathan R. Yates, Ivo Souza, Marvin L. Cohen, and Steven G. Louie, 2007, "Electron-Phonon Interaction via Electronic and Lattice Wannier Functions: Superconductivity in Boron-Doped Diamond Reexamined," Phys. Rev. Lett. **98**, 047005.

Gjerding, Morten, Thorbjørn Skovhus, Asbjørn Rasmussen, Fabian Bertoldo, Ask Hjorth Larsen, Jens Jørgen Mortensen, and Kristian Sommer Thygesen, 2021, "Atomic simulation recipes: A `Python` framework and library for automated workflows," Comput. Mater. Sci. **199**, 110731.

Golze, Dorothea, Marc Dvorak, and Patrick Rinke, 2019, "The *GW* compendium: A practical guide to theoretical photoemission spectroscopy," Front. Chem. **7**, 377.

Gontier, D., A. Levitt, and S. Siraj-dine, 2019, "Numerical construction of Wannier functions through homotopy," J. Math. Phys. (N.Y.) **60**, 031901.

Gonze, Xavier, 1997, "First-principles responses of solids to atomic displacements and homogeneous electric fields: Implementation of a conjugate-gradient algorithm," Phys. Rev. B **55**, 10337–10354.

Gonze, Xavier, *et al.*, 2020, "The `ABINIT` project: Impact, environment and recent developments," Comput. Phys. Commun. **248**, 107042.

Gosálbez-Martínez, Daniel, Ivo Souza, and David Vanderbilt, 2015, "Chiral degeneracies and Fermi-surface Chern numbers in bcc Fe," Phys. Rev. B **92**, 085138.

Graf, M., and P. Vogl, 1995, "Electromagnetic fields and dielectric response in empirical tight-binding theory," Phys. Rev. B **51**, 4940–4949.

Grassano, Davide, Davide Campi, Antimo Marrazzo, and Nicola Marzari, 2023, "Complementary screening for quantum spin Hall insulators in two-dimensional exfoliable materials," Phys. Rev. Mater. **7**, 094202.

Grechnev, Alexei, I. Di Marco, M. I. Katsnelson, A. I. Lichtenstein, John Wills, and Olle Eriksson, 2007, "Theory of bulk and surface quasiparticle spectra for Fe, Co, and Ni," Phys. Rev. B **76**, 035107.

Gresch, Dominik, Gabriel Autès, Oleg V. Yazyev, Matthias Troyer, David Vanderbilt, B. Andrei Bernevig, and Alexey A. Soluyanov, 2017, "`Z2Pack`: Numerical implementation of hybrid Wannier centers for identifying topological materials," Phys. Rev. B **95**, 075146.

Gresch, Dominik, QuanSheng Wu, Georg W. Winkler, Rico Häuselmann, Matthias Troyer, and Alexey A. Soluyanov, 2018, "Automated construction of symmetrized Wannier-like tight-binding models from *ab initio* calculations," Phys. Rev. Mater. **2**, 103805.

Groth, C. W., M. Wimmer, A. R. Akhmerov, J. Tworzydło, and C. W. J. Beenakker, 2009, "Theory of the Topological Anderson Insulator," Phys. Rev. Lett. **103**, 196805.

Groth, Christoph W., Michael Wimmer, Anton R. Akhmerov, and Xavier Waintal, 2014, "`Kwant`: A software package for quantum transport," New J. Phys. **16**, 063065.

Gubernatis, J. E., Mark Jarrell, R. N. Silver, and D. S. Sivia, 1991, "Quantum Monte Carlo simulations and maximum entropy: Dynamics from imaginary-time data," Phys. Rev. B **44**, 6011–6029.

Gunawardana, Thivan M., Ari M. Turner, and Ryan Barnett, 2024, "Optimally localized single-band Wannier functions for two-dimensional Chern insulators," Phys. Rev. Res. **6**, 023046.

Gunst, Tue, Troels Markussen, Kurt Stokbro, and Mads Brandbyge, 2016, "First-principles method for electron-phonon coupling and electron mobility: Applications to two-dimensional materials," Phys. Rev. B **93**, 035414.

Gygi, F., 2008, "Architecture of `Qbox`: A scalable first-principles molecular dynamics code," IBM J. Res. Dev. **52**, 137–144.

Gygi, François, Jean-Luc Fattebert, and Eric Schwegler, 2003, "Computation of maximally localized Wannier functions using a simultaneous diagonalization algorithm," Comput. Phys. Commun. **155**, 1–6.

Haber, Jonah B., Diana Y. Qiu, Felipe H. da Jornada, and Jeffrey B. Neaton, 2023, "Maximally localized exciton Wannier functions for solids," Phys. Rev. B **108**, 125118.

Haldane, F. D. M., 1988, "Model for a Quantum Hall Effect without Landau Levels: Condensed-Matter Realization of the 'Parity Anomaly,' " Phys. Rev. Lett. **61**, 2015–2018.

Hamann, D. R., and David Vanderbilt, 2009, "Maximally localized Wannier functions for *GW* quasiparticles," Phys. Rev. B **79**, 045109.

Hariki, Atsushi, Takayuki Uozumi, and Jan Kuneš, 2017, "LDA + DMFT approach to core-level spectroscopy: Application to 3*d* transition metal compounds," Phys. Rev. B **96**, 045111.

Hariki, Atsushi, Mathias Winder, and Jan Kuneš, 2018, "Continuum Charge Excitations in High-Valence Transition-Metal Oxides Revealed by Resonant Inelastic X-Ray Scattering," Phys. Rev. Lett. **121**, 126403.

Hasan, M. Z., and C. L. Kane, 2010, "Colloquium: Topological insulators," Rev. Mod. Phys. **82**, 3045–3067.

Haule, Kristjan, Viktor Oudovenko, Sergej Y. Savrasov, and Gabriel Kotliar, 2005, "The $\alpha \rightarrow \gamma$ Transition in Ce: A Theoretical View from Optical Spectroscopy," Phys. Rev. Lett. **94**, 036401.

Haule, Kristjan, and Gheorghe L. Pascut, 2016, "Forces for structural optimizations in correlated materials within a DFT + embedded DMFT functional approach," Phys. Rev. B **94**, 195146.

Haule, Kristjan, Chuck-Hou Yee, and Kyoo Kim, 2010, "Dynamical mean-field theory within the full-potential methods: Electronic structure of $CeIrIn_5$, $CeCoIn_5$, and $CeRhIn_5$," Phys. Rev. B **81**, 195107.

Haverkort, M. W., M. Zwierzycki, and O. K. Andersen, 2012, "Multiplet ligand-field theory using Wannier orbitals," Phys. Rev. B **85**, 165113.

Haverkort, Maurits W., 2016, "Quanty for core level spectroscopy—Excitons, resonances and band excitations in time and frequency domain," J. Phys. Conf. Ser. **712**, 012001.

HDF Group, 2023, "Hierarchical Data Format version 5 (HDF5)," https://www.hdfgroup.org/HDF5/ (accessed on December 14, 2023).

He, Xu, Nicole Helbig, Matthieu J. Verstraete, and Eric Bousquet, 2021, "`Tb2j`: A `Python` package for computing magnetic interaction parameters," Comput. Phys. Commun. **264**, 107938.

Held, K., 2007, "Electronic structure calculations using dynamical mean field theory," Adv. Phys. **56**, 829–926.

Herbst, Michael F., Antoine Levitt, and Eric Cancés, 2023, computer code `DFTK`, https://dftk.org.

Heyd, Jochen, Gustavo E. Scuseria, and Matthias Ernzerhof, 2003, "Hybrid functionals based on a screened Coulomb potential," J. Chem. Phys. **118**, 8207–8215.

Hirata, So, and Martin Head-Gordon, 1999, "Time-dependent density functional theory within the Tamm-Dancoff approximation," Chem. Phys. Lett. **314**, 291–299.

Huber, Sebastiaan P., *et al.*, 2020, "`AiiDA 1.0`, a scalable computational infrastructure for automated reproducible workflows and data provenance," Sci. Data **7**, 300.

Huber, Sebastiaan P., *et al.*, 2021, "Common workflows for computing material properties using different quantum engines," npj Comput. Mater. **7**, 136.

Hunter, J. D., 2007, "`Matplotlib`: A 2D graphics environment," Comput. Sci. Eng. **9**, 90–95.

Ibañez-Azpiroz, Julen, Fernando de Juan, and Ivo Souza, 2022, "Assessing the role of interatomic position matrix elements in tight-binding calculations of optical properties," SciPost Phys. **12**, 070.

Ibañez-Azpiroz, Julen, Stepan S. Tsirkin, and Ivo Souza, 2018, "*Ab initio* calculation of the shift photocurrent by Wannier interpolation," Phys. Rev. B **97**, 245143.

Jain, Anubhav, *et al.*, 2015, "`FireWorks`: A dynamic workflow system designed for high-throughput applications," Concurr. Comput. **27**, 5037–5059.

James, A. D. N., E. I. Harris-Lee, A. Hampel, M. Aichhorn, and S. B. Dugdale, 2021, "Wave functions, electronic localization, and bonding properties for correlated materials beyond the Kohn-Sham formalism," Phys. Rev. B **103**, 035106.

Jhalani, Vatsal A., Jin-Jian Zhou, Jinsoo Park, Cyrus E. Dreyer, and Marco Bernardi, 2020, "Piezoelectric Electron-Phonon Interaction from *Ab Initio* Dynamical Quadrupoles: Impact on Charge Transport in Wurtzite GaN," Phys. Rev. Lett. **125**, 136602.

Jiang, Hua, Lei Wang, Qing-feng Sun, and X. C. Xie, 2009, "Numerical study of the topological Anderson insulator in HgTe/CdTe quantum wells," Phys. Rev. B **80**, 165316.

Jin, Gan, Daye Zheng, and Lixin He, 2021, "Calculation of Berry curvature using non-orthogonal atomic orbitals," J. Phys. Condens. Matter **33**, 325503.

Jónsson, Elvar Ö., Susi Lehtola, Martti Puska, and Hannes Jónsson, 2017, "Theory and applications of generalized Pipek-Mezey Wannier functions," J. Chem. Theory Comput. **13**, 460–474.

Kaltak, Merzuk, 2015, "Merging *GW* with DMFT," Ph.D. thesis (University of Vienna).

Kane, C. L., and E. J. Mele, 2005a, "$\mathbb{Z}_2$ Topological Order and the Quantum Spin Hall Effect," Phys. Rev. Lett. **95**, 146802.

Kane, C. L., and E. J. Mele, 2005b, "Quantum Spin Hall Effect in Graphene," Phys. Rev. Lett. **95**, 226801.

Kapil, Venkat, *et al.*, 2019, "`i-PI 2.0`: A universal force engine for advanced molecular simulations," Comput. Phys. Commun. **236**, 214–223.

Karolak, M., G. Ulm, T. Wehling, V. Mazurenko, A. Poteryaev, and A. Lichtenstein, 2010, "Double counting in LDA + DMFT—The example of NiO," J. Electron Spectrosc. Relat. Phenom. **181**, 11–15.

Karp, Jonathan, Alexander Hampel, and Andrew J. Millis, 2021, "Dependence of DFT + DMFT results on the construction of the correlated orbitals," Phys. Rev. B **103**, 195101.

Kaye, Jason, Sophie Beck, Alex Barnett, Lorenzo Van Muñoz, and Olivier Parcollet, 2023, "Automatic, high-order, and adaptive algorithms for Brillouin zone integration," SciPost Phys. **15**, 062.

Khalaf, Eslam, Hoi Chun Po, Ashvin Vishwanath, and Haruki Watanabe, 2018, "Symmetry Indicators and Anomalous Surface States of Topological Crystalline Insulators," Phys. Rev. X **8**, 031070.

King-Smith, R. D., and David Vanderbilt, 1993, "Theory of polarization of crystalline solids," Phys. Rev. B **47**, 1651–1654.

Kivelson, S., 1982, "Wannier functions in one-dimensional disordered systems: Application to fractionally charged solitons," Phys. Rev. B **26**, 4269–4277.

Koçer, Can P., Kristjan Haule, G. Lucian Pascut, and Bartomeu Monserrat, 2020, "Efficient lattice dynamics calculations for correlated materials with DFT + DMFT," Phys. Rev. B **102**, 245104.

Koelling, D. D., and J. H. Wood, 1986, "On the interpolation of eigenvalues and a resultant integration scheme," J. Comput. Phys. **67**, 253–262.

Kohn, W., 1996, "Density Functional and Density Matrix Method Scaling Linearly with the Number of Atoms," Phys. Rev. Lett. **76**, 3168–3171.

Koretsune, Takashi, 2023, "Construction of maximally-localized Wannier functions using crystal symmetry," Comput. Phys. Commun. **285**, 108645.

Kotliar, G., S. Y. Savrasov, K. Haule, V. S. Oudovenko, O. Parcollet, and C. A. Marianetti, 2006, "Electronic structure calculations with dynamical mean-field theory," Rev. Mod. Phys. **78**, 865–951.

Kraisler, Eli, and Leeor Kronik, 2013, "Piecewise Linearity of Approximate Density Functionals Revisited: Implications for Frontier Orbital Energies," Phys. Rev. Lett. **110**, 126403.

Kresse, G., and D. Joubert, 1999, "From ultrasoft pseudopotentials to the projector augmented-wave method," Phys. Rev. B **59**, 1758–1775.

Kruthoff, Jorrit, Jan de Boer, Jasper van Wezel, Charles L. Kane, and Robert-Jan Slager, 2017, "Topological Classification of Crystalline Insulators through Band Structure Combinatorics," Phys. Rev. X **7**, 041069.

Kubo, Ryogo, 1957, "Statistical-mechanical theory of irreversible processes. I. General theory and simple applications to magnetic and conduction problems," J. Phys. Soc. Jpn. **12**, 570–586.

Kühne, Thomas D., *et al.*, 2020, "`CP2K`: An electronic structure and molecular dynamics software package—`Quickstep`: Efficient and accurate electronic structure calculations," J. Chem. Phys. **152**, 194103.

Kümmel, Stephan, and Leeor Kronik, 2008, "Orbital-dependent density functionals: Theory and applications," Rev. Mod. Phys. **80**, 3–60.

Kune, Jan, Ryotaro Arita, Philipp Wissgott, Alessandro Toschi, Hiroaki Ikeda, and Karsten Held, 2010, "`Wien2wannier`: From linearized augmented plane waves to maximally localized Wannier functions," Comput. Phys. Commun. **181**, 1888–1895.

Kuneš, Jan, 2011, "Efficient treatment of two-particle vertices in dynamical mean-field theory," Phys. Rev. B **83**, 085102.

Kurita, Kensuke, Takahiro Misawa, Kazuyoshi Yoshimi, Kota Ido, and Takashi Koretsune, 2023, "Interface tool from `Wannier90` to `RESPACK`: `wan2respack`," Comput. Phys. Commun. **292**, 108854.

Lafuente-Bartolome, Jon, Idoia G. Gurtubay, and Asier Eiguren, 2020a, "Fully anisotropic superconductivity with few Helmholtz Fermi-surface harmonics," Phys. Rev. B **102**, 161107.

Lafuente-Bartolome, Jon, Idoia G. Gurtubay, and Asier Eiguren, 2020b, "Symmetric Helmholtz Fermi-surface harmonics for an optimal representation of anisotropic quantities on the Fermi surface: Application to the electron-phonon problem," Phys. Rev. B **102**, 165113.

Lafuente-Bartolome, Jon, Chao Lian, Weng Hong Sio, Idoia G. Gurtubay, Asier Eiguren, and Feliciano Giustino, 2022, "Unified Approach to Polarons and Phonon-Induced Band Structure Renormalization," Phys. Rev. Lett. **129**, 076402.

Lam, Siu Kwan, Antoine Pitrou, and Stanley Seibert, 2015, "`Numba`: A LLVM-based `Python` JIT compiler," in *Proceedings of the Second Workshop on the LLVM Compiler Infrastructure in HPC (LLVM '15), Austin, 2015* (Association for Computing Machinery, New York), 10.1145/2833157.2833162.

Landauer, Rolf, 1970, "Electrical resistance of disordered one-dimensional lattices," Philos. Mag. **21**, 863–867.

Larsen, Ask Hjorth, *et al.*, 2017, "The `Atomic Simulation Environment`—A `Python` library for working with atoms," J. Phys. Condens. Matter **29**, 273002.

Lechermann, F., A. Georges, A. Poteryaev, S. Biermann, M. Posternak, A. Yamasaki, and O. K. Andersen, 2006, "Dynamical mean-field theory using Wannier functions: A flexible route to electronic structure calculations of strongly correlated materials," Phys. Rev. B **74**, 125120.

Lee, Chengteh, Weitao Yang, and Robert G. Parr, 1988, "Development of the Colle-Salvetti correlation-energy formula into a functional of the electron density," Phys. Rev. B **37**, 785–789.

Lee, Chi-Cheng, Yung-Ting Lee, Masahiro Fukuda, and Taisuke Ozaki, 2018, "Tight-binding calculations of optical matrix elements for conductivity using nonorthogonal atomic orbitals: Anomalous Hall conductivity in bcc Fe," Phys. Rev. B **98**, 115115.

Lee, D. H., and J. D. Joannopoulos, 1981a, "Simple scheme for surface-band calculations. I," Phys. Rev. B **23**, 4988–4996.

Lee, D. H., and J. D. Joannopoulos, 1981b, "Simple scheme for surface-band calculations. II. The Green's function," Phys. Rev. B **23**, 4997–5004.

Lee, Hyungjun, *et al.*, 2023, "Electron-phonon physics from first principles using the `EPW` code," npj Comput. Mater. **9**, 156.

Lee, Nien-En, Hsiao-Yi Chen, Jin-Jian Zhou, and Marco Bernardi, 2021, "Facile *ab initio* approach for self-localized polarons from canonical transformations," Phys. Rev. Mater. **5**, 063805.

Lee, Nien-En, Jin-Jian Zhou, Luis A. Agapito, and Marco Bernardi, 2018, "Charge transport in organic molecular semiconductors from first principles: The bandlike hole mobility in a naphthalene crystal," Phys. Rev. B **97**, 115203.

Lee, Young-Su, Marco Buongiorno Nardelli, and Nicola Marzari, 2005, "Band Structure and Quantum Conductance of Nanostructures from Maximally Localized Wannier Functions: The Case of Functionalized Carbon Nanotubes," Phys. Rev. Lett. **95**, 076804.

Leonov, I., V. I. Anisimov, and D. Vollhardt, 2014, "First-Principles Calculation of Atomic Forces and Structural Distortions in Strongly Correlated Materials," Phys. Rev. Lett. **112**, 146401.

Li, Chen, Xiao Zheng, Aron J. Cohen, Paula Mori-Sánchez, and Weitao Yang, 2015, "Local Scaling Correction for Reducing Delocalization Error in Density Functional Approximations," Phys. Rev. Lett. **114**, 053001.

Li, Chen, Xiao Zheng, Neil Qiang Su, and Weitao Yang, 2018, "Localized orbital scaling correction for systematic elimination of delocalization error in density functional approximations," Natl. Sci. Rev. **5**, 203–215.

Li, Jian, Rui-Lin Chu, J. K. Jain, and Shun-Qing Shen, 2009, "Topological Anderson Insulator," Phys. Rev. Lett. **102**, 136806.

Li, Wu, 2015, "Electrical transport limited by electron-phonon coupling from Boltzmann transport equation: An *ab initio* study of Si, Al, and MoS_2," Phys. Rev. B **92**, 075405.

Li, Zhenglu, Gabriel Antonius, Yang-Hao Chan, and Steven G. Louie, 2024, "Electron-phonon coupling from *GW* perturbation theory: Practical workflow combining `BerkeleyGW`, `ABINIT`, and `EPW`," Comput. Phys. Commun. **295**, 109003.

Li, Zhenglu, Gabriel Antonius, Meng Wu, Felipe H. da Jornada, and Steven G. Louie, 2019, "Electron-Phonon Coupling from *Ab Initio* Linear-Response Theory within the *GW* Method: Correlation-Enhanced Interactions and Superconductivity in $Ba_{1-x}K_xBiO_3$," Phys. Rev. Lett. **122**, 186402.

Lihm, Jae-Mo, 2022, "Accurate calculation of Wannier centers and position matrix elements I: Translationally-invariant formula," lecture, Wannier 2022 Developers Meeting, Trieste, Italy, 2022, http://video.ictp.it/WEB/2022/2022_05_23-smr3757/2022_05_23-11_00-smr3757.mp4.

Lihm, Jae-Mo, and Cheol-Hwan Park, 2019, "Reliable methods for seamless stitching of tight-binding models based on maximally localized Wannier functions," Phys. Rev. B **99**, 125117.

Lihm, Jae-Mo, and Cheol-Hwan Park, 2021, "Wannier Function Perturbation Theory: Localized Representation and Interpolation of Wave Function Perturbation," Phys. Rev. X **11**, 041053.

Lilia, Boeri, *et al.*, 2022, "The 2021 room-temperature superconductivity roadmap," J. Phys. Condens. Matter **34**, 183002.

Linscott, Edward B., Nicola Colonna, Riccardo De Gennaro, Ngoc Linh Nguyen, Giovanni Borghi, Andrea Ferretti, Ismaila Dabo, and Nicola Marzari, 2023, "`koopmans`: An open-source package for accurately and efficiently predicting spectral properties with Koopmans functionals," J. Chem. Theory Comput. **19**, 7097–7111.

Liu, Xiaoxiong, Stepan S. Tsirkin, and Ivo Souza, 2023, "Covariant derivatives of Berry-type quantities: Application to nonlinear transport," arXiv:2303.10129.

Lopez, M. G., David Vanderbilt, T. Thonhauser, and Ivo Souza, 2012, "Wannier-based calculation of the orbital magnetization in crystals," Phys. Rev. B **85**, 014435.

Lucrezi, Roman, Pedro P. Ferreira, Samad Hajinazar, Hitoshi Mori, Hari Paudyal, Elena R. Margine, and Christoph Heil, 2024, "Full-bandwidth anisotropic Migdal-Eliashberg theory and its application to superhydrides," Commun. Phys. **7**, 33.

Lüder, Johann, Johan Schött, Barbara Brena, Maurits W. Haverkort, Patrik Thunström, Olle Eriksson, Biplab Sanyal, Igor Di Marco, and Yaroslav O. Kvashnin, 2017, "Theory of *l*-edge spectroscopy of strongly correlated systems," Phys. Rev. B **96**, 245131.

Luo, Yao, Dhruv Desai, Benjamin K. Chang, Jinsoo Park, and Marco Bernardi, 2024, "Data-Driven Compression of Electron-Phonon Interactions," Phys. Rev. X **14**, 021023.

Ma, Jie, and Lin-Wang Wang, 2016, "Using Wannier functions to improve solid band gap predictions in density functional theory," Sci. Rep. **6**, 24924.

Macheda, Francesco, Paolo Barone, and Francesco Mauri, 2022, "Electron-Phonon Interaction and Longitudinal-Transverse Phonon Splitting in Doped Semiconductors," Phys. Rev. Lett. **129**, 185902.

Macheda, Francesco, and Nicola Bonini, 2018, "Magnetotransport phenomena in *p*-doped diamond from first principles," Phys. Rev. B **98**, 201201.

Madsen, Georg K. H., Jesús Carrete, and Matthieu J. Verstraete, 2018, "BoltzTraP2, a program for interpolating band structures and calculating semi-classical transport coefficients," Comput. Phys. Commun. **231**, 140–145.

Madsen, Georg K. H., and David J. Singh, 2006, "BoltzTraP. A code for calculating band-structure dependent quantities," Comput. Phys. Commun. **175**, 67–71.

Mahler, Aaron, Jacob Williams, Neil Qiang Su, and Weitao Yang, 2022, "Localized orbital scaling correction for periodic systems," Phys. Rev. B **106**, 035147.

Maliyov, Ivan, Jinsoo Park, and Marco Bernardi, 2021, "*Ab initio* electron dynamics in high electric fields: Accurate prediction of velocity-field curves," Phys. Rev. B **104**, L100303.

Margine, E. R., and F. Giustino, 2013, "Anisotropic Migdal-Eliashberg theory using Wannier functions," Phys. Rev. B **87**, 024505.

Marini, Giovanni, Guglielmo Marchese, Gianni Profeta, Jelena Sjakste, Francesco Macheda, Nathalie Vast, Francesco Mauri, and Matteo Calandra, 2024, "EPIq: An open-source software for the calculation of electron-phonon interaction related properties," Comput. Phys. Commun. **295**, 108950.

Markel, J., 1971, "FFT pruning," IEEE Trans. Audio Electroacoust. **19**, 305–311.

Marrazzo, Antimo, and Nicola Colonna, 2024, "Spin-dependent interactions in orbital-density-dependent functionals: Noncollinear Koopmans spectral functionals," Phys. Rev. Res. **6**, 033085.

Marrazzo, Antimo, Marco Gibertini, Davide Campi, Nicolas Mounet, and Nicola Marzari, 2019, "Relative abundance of $\mathbb{Z}_2$ topological order in exfoliable two-dimensional insulators," Nano Lett. **19**, 8431–8440.

Marrazzo, Antimo, and Raffaele Resta, 2016, "Irrelevance of the Boundary on the Magnetization of Metals," Phys. Rev. Lett. **116**, 137201.

Marrazzo, Antimo, and Raffaele Resta, 2019, "Local Theory of the Insulating State," Phys. Rev. Lett. **122**, 166602.

Marsili, Margherita, Edoardo Mosconi, Filippo De Angelis, and Paolo Umari, 2017, "Large-scale *GW*-BSE calculations with N^3 scaling: Excitonic effects in dye-sensitized solar cells," Phys. Rev. B **95**, 075415.

Martin, Richard M., 2004, *Electronic Structure: Basic Theory and Practical Methods* (Cambridge University Press, Cambridge, England).

Martin, Richard M., 2020, *Electronic Structure: Basic Theory and Practical Methods*, 2nd ed. (Cambridge University Press, Cambridge, England).

Marzari, Nicola, Andrea Ferretti, and Chris Wolverton, 2021, "Electronic-structure methods for materials design," Nat. Mater. **20**, 736–749.

Marzari, Nicola, Arash A. Mostofi, Jonathan R. Yates, Ivo Souza, and David Vanderbilt, 2012, "Maximally localized Wannier functions: Theory and applications," Rev. Mod. Phys. **84**, 1419–1475.

Marzari, Nicola, and David Vanderbilt, 1997, "Maximally localized generalized Wannier functions for composite energy bands," Phys. Rev. B **56**, 12847–12865.

Marzari, Nicola, David Vanderbilt, and M. C. Payne, 1997, "Ensemble Density-Functional Theory for *Ab Initio* Molecular Dynamics of Metals and Finite-Temperature Insulators," Phys. Rev. Lett. **79**, 1337–1340.

Mauri, Francesco, Giulia Galli, and Roberto Car, 1993, "Orbital formulation for electronic-structure calculations with linear system-size scaling," Phys. Rev. B **47**, 9973–9976.

Merkel, Maximilian E., Alberto Carta, Sophie Beck, and Alexander Hampel, 2022, "Solid_DMFT: Gray-boxing DFT + DMFT materials simulations with TRIQS," J. Open Source Software **7**, 4623.

Metzner, Walter, and Dieter Vollhardt, 1989, "Correlated Lattice Fermions in $d = \infty$ Dimensions," Phys. Rev. Lett. **62**, 324–327.

Michel, L., and J. Zak, 1999, "Connectivity of energy bands in crystals," Phys. Rev. B **59**, 5998–6001.

Monacelli, Lorenzo, Raffaello Bianco, Marco Cherubini, Matteo Calandra, Ion Errea, and Francesco Mauri, 2021, "The stochastic self-consistent harmonic approximation: Calculating vibrational properties of materials with full quantum and anharmonic effects," J. Phys. Condens. Matter **33**, 363001.

Mori, Hitoshi, Takuya Nomoto, Ryotaro Arita, and Elena R. Margine, 2024, "Efficient anisotropic Migdal-Eliashberg calculations with an intermediate representation basis and Wannier interpolation," Phys. Rev. B **110**, 064505.

Mossotti, O. F., 1850, "Discussione analitica sull'influenza che l'azione di un mezzo dielettrico ha sulla distribuzione dell'elettricità alla superficie di più corpi elettrici disseminati in esso [Analytical discussion on the influence that the action of a dielectric medium has on the distribution of electricity on the surface of several electric bodies scattered in it]," in *Memorie di Matematica e di Fisica della Società Italiana delle Scienze Residente in Modena*, Vol. 24 (Società Italiana delle Scienze, Verona, Italy), p. 49–74, https://media.accademiaxl.it/memorie/S1-VXXIV-P2-1850/Mossotti49-74.pdf.

Mostofi, Arash A., Jonathan R. Yates, Young-Su Lee, Ivo Souza, David Vanderbilt, and Nicola Marzari, 2008, "Wannier90: A tool for obtaining maximally-localised Wannier functions," Comput. Phys. Commun. **178**, 685–699.

Mostofi, Arash A., Jonathan R. Yates, Giovanni Pizzi, Young-Su Lee, Ivo Souza, David Vanderbilt, and Nicola Marzari, 2014, "An updated version of Wannier90: A tool for obtaining maximally-localised Wannier functions," Comput. Phys. Commun. **185**, 2309–2310.

Mountjoy, Jeff, Michelle Todd, and Nicholas J. Mosey, 2017, "Exact exchange with non-orthogonal generalized Wannier functions," J. Chem. Phys. **146**, 104108.

Muechler, Lukas, Danis I. Badrtdinov, Alexander Hampel, Jennifer Cano, Malte Rösner, and Cyrus E. Dreyer, 2022, "Quantum embedding methods for correlated excited states of point defects: Case studies and challenges," Phys. Rev. B **105**, 235104.

Mulliken, R. S., 1955, "Electronic population analysis on LCAO-MO molecular wave functions. I," J. Chem. Phys. **23**, 1833–1840.

Mustafa, Jamal I., Sinisa Coh, Marvin L. Cohen, and Steven G. Louie, 2015, "Automated construction of maximally localized Wannier functions: Optimized projection functions method," Phys. Rev. B **92**, 165134.

Nakamura, Kazuma, Yoshihide Yoshimoto, Yusuke Nomura, Terumasa Tadano, Mitsuaki Kawamura, Taichi Kosugi, Kazuyoshi Yoshimi, Takahiro Misawa, and Yuichi Motoyama, 2021, "RESPACK: An *ab initio* tool for derivation of effective low-energy model of material," Comput. Phys. Commun. **261**, 107781.

Nekrasov, I. A., K. Held, G. Keller, D. E. Kondakov, Th. Pruschke, M. Kollar, O. K. Andersen, V. I. Anisimov, and D. Vollhardt, 2006,

"Momentum-resolved spectral functions of $SrVO_3$ calculated by LDA + DMFT," Phys. Rev. B **73**, 155112.

Nenciu, G., 1991, "Dynamics of band electrons in electric and magnetic fields: Rigorous justification of the effective Hamiltonians," Rev. Mod. Phys. **63**, 91–127.

Neupert, T., and F. Schindler, 2018, "Lecture notes on topological crystalline insulators," in *Topological Matter—Lectures from the Topological Matter School 2017*, edited by D. Bercioux, J. Cayssol, M. G. Vergniory, and M. Reyes Calvo (Springer, Cham, Switzerland), Chap. 2, p. 31.

Nguyen, Ngoc Linh, Nicola Colonna, Andrea Ferretti, and Nicola Marzari, 2018, "Koopmans-Compliant Spectral Functionals for Extended Systems," Phys. Rev. X **8**, 021051.

Nikolaev, S. A., and I. V. Solovyev, 2014, "Orbital magnetization of insulating perovskite transition-metal oxides with a net ferromagnetic moment in the ground state," Phys. Rev. B **89**, 064428.

Noffsinger, Jesse, Feliciano Giustino, Brad D. Malone, Cheol-Hwan Park, Steven G. Louie, and Marvin L. Cohen, 2010, "`EPW`: A program for calculating the electron-phonon coupling using maximally localized Wannier functions," Comput. Phys. Commun. **181**, 2140–2148.

Noffsinger, Jesse, Emmanouil Kioupakis, Chris G. Van de Walle, Steven G. Louie, and Marvin L. Cohen, 2012, "Phonon-Assisted Optical Absorption in Silicon from First Principles," Phys. Rev. Lett. **108**, 167402.

Nomoto, Takuya, Takashi Koretsune, and Ryotaro Arita, 2020, "Local force method for the *ab initio* tight-binding model: Effect of spin-dependent hopping on exchange interactions," Phys. Rev. B **102**, 014444.

Nomura, Yusuke, Shiro Sakai, Massimo Capone, and Ryotaro Arita, 2015, "Unified understanding of superconductivity and Mott transition in alkali-doped fullerides from first principles," Sci. Adv. **1**, e1500568.

Numba-PythTB Collaboration, 2023, high-performance `Numba` implementation of computer code `PythTB`, https://github.com/mikelgda/yeet-pythtb.

Nunes, R. W., and David Vanderbilt, 1994, "Generalization of the density-matrix method to a nonorthogonal basis," Phys. Rev. B **50**, 17611–17614.

Oliveira, Micael J. T., *et al.*, 2020, "The CECAM Electronic Structure Library and the modular software development paradigm," J. Chem. Phys. **153**, 024117.

Ong, Shyue Ping, William Davidson Richards, Anubhav Jain, Geoffroy Hautier, Michael Kocher, Shreyas Cholia, Dan Gunter, Vincent L. Chevrier, Kristin A. Persson, and Gerbrand Ceder, 2013, "`Python` Materials Genomics (`pymatgen`): A robust, open-source `Python` library for materials analysis," Comput. Mater. Sci. **68**, 314–319.

Onida, Giovanni, Lucia Reining, and Angel Rubio, 2002, "Electronic excitations: Density-functional versus many-body Green's-function approaches," Rev. Mod. Phys. **74**, 601–659.

Ordejón, Pablo, David A. Drabold, Matthew P. Grumbach, and Richard M. Martin, 1993, "Unconstrained minimization approach for electronic computations that scales linearly with system size," Phys. Rev. B **48**, 14646–14649.

Oudovenko, V. S., G. Pálsson, K. Haule, G. Kotliar, and S. Y. Savrasov, 2006, "Electronic structure calculations of strongly correlated electron systems by the dynamical mean-field method," Phys. Rev. B **73**, 035120.

Ozaki, T., and H. Kino, 2005, "Efficient projector expansion for the *ab initio* LCAO method," Phys. Rev. B **72**, 045121.

Ozaki, Taisuke, Kengo Nishio, and Hiori Kino, 2010, "Efficient implementation of the nonequilibrium Green function method for electronic transport calculations," Phys. Rev. B **81**, 035116.

Paleari, Fulvio, and Andrea Marini, 2022, "Exciton-phonon interaction calls for a revision of the 'exciton' concept," Phys. Rev. B **106**, 125403.

Panati, Gianluca, 2007, "Triviality of Bloch and Bloch-Dirac bundles," Ann. Henri Poincaré **8**, 995–1011.

Panati, Gianluca, and Adriano Pisante, 2013, "Bloch bundles, Marzari-Vanderbilt functional and maximally localized Wannier functions," Commun. Math. Phys. **322**, 835–875.

Parcollet, Olivier, Michel Ferrero, Thomas Ayral, Hartmut Hafermann, Igor Krivenko, Laura Messio, and Priyanka Seth, 2015, "`TRIQS`: A toolbox for research on interacting quantum systems," Comput. Phys. Commun. **196**, 398–415.

Park, Hyowon, Kristjan Haule, and Gabriel Kotliar, 2011, "Magnetic Excitation Spectra in $BaFe_2As_2$: A Two-Particle Approach within a Combination of the Density Functional Theory and the Dynamical Mean-Field Theory Method," Phys. Rev. Lett. **107**, 137007.

Park, Jinsoo, Jin-Jian Zhou, Vatsal A. Jhalani, Cyrus E. Dreyer, and Marco Bernardi, 2020, "Long-range quadrupole electron-phonon interaction from first principles," Phys. Rev. B **102**, 125203.

Paul, Arpita, and Turan Birol, 2019, "Applications of DFT + DMFT in materials science," Annu. Rev. Mater. Res. **49**, 31–52.

Pavarini, E., S. Biermann, A. Poteryaev, A. I. Lichtenstein, A. Georges, and O. K. Andersen, 2004, "Mott Transition and Suppression of Orbital Fluctuations in Orthorhombic $3d^1$ Perovskites," Phys. Rev. Lett. **92**, 176403.

Pavarini, Eva, Erik, Koch, Alexander, Lichtenstein, and Dieter, Vollhardt, 2011, Eds., *The LDA+DMFT Approach to Strongly Correlated Materials*, Vol. 1 (Schriften des Forschungszentrums Jülich, Jülich, Germany).

Pedersen, Thomas Garm, Kjeld Pedersen, and Thomas Brun Kriestensen, 2001, "Optical matrix elements in tight-binding calculations," Phys. Rev. B **63**, 201101.

Peng, G.-H., P.-Y. Lo, W.-H. Li, Y.-C. Huang, Y.-H. Chen, C.-H. Lee, C.-K. Yang, and S.-J. Cheng, 2019, "Distinctive signatures of the spin- and momentum-forbidden dark exciton states in the photoluminescence of strained WSe_2 monolayers under thermalization," Nano Lett. **19**, 2299.

Perdew, John P., Matthias Ernzerhof, and Kieron Burke, 1996, "Rationale for mixing exact exchange with density functional approximations," J. Chem. Phys. **105**, 9982–9985.

PERTURBO Collaboration, 2023, computer code `PERTURBO`, https://perturbo-code.github.io/.

Phoebe Collaboration, 2023, computer code `Phoebe`, https://mir-group.github.io/phoebe/.

Pick, Robert M., Morrel H. Cohen, and Richard M. Martin, 1970, "Microscopic theory of force constants in the adiabatic approximation," Phys. Rev. B **1**, 910–920.

Pickem, Matthias, Emanuele Maggio, and Jan M. Tomczak, 2023, "LinReTraCe: The linear response transport centre," SciPost Phys. Codebases 16.

Pickett, Warren E., 1989, "Pseudopotential methods in condensed matter applications," Comput. Phys. Rep. **9**, 115–197.

Pickett, Warren E., Henry Krakauer, and Philip B. Allen, 1988, "Smooth Fourier interpolation of periodic functions," Phys. Rev. B **38**, 2721–2726.

Pipek, János, and Paul G. Mezey, 1989, "A fast intrinsic localization procedure applicable for *ab initio* and semiempirical linear combination of atomic orbital wave functions," J. Chem. Phys. **90**, 4916–4926.

Pizzi, Giovanni, Andrea Cepellotti, Riccardo Sabatini, Nicola Marzari, and Boris Kozinsky, 2016, "AiiDA: Automated interactive infrastructure and database for computational science," Comput. Mater. Sci. **111**, 218–230.

Pizzi, Giovanni, Dmitri Volja, Boris Kozinsky, Marco Fornari, and Nicola Marzari, 2014, "BoltzWann: A code for the evaluation of thermoelectric and electronic transport properties with a maximally-localized Wannier functions basis," Comput. Phys. Commun. **185**, 422–429.

Pizzi, Giovanni, *et al.*, 2020, "Wannier90 as a community code: New features and applications," J. Phys. Condens. Matter **32**, 165902.

Plekhanov, Evgeny, Nicola Bonini, and Cedric Weber, 2021, "Calculating dynamical mean-field theory forces in *ab initio* ultrasoft pseudopotential formalism," Phys. Rev. B **104**, 235131.

Plekhanov, Evgeny, Phil Hasnip, Vincent Sacksteder, Matt Probert, Stewart J. Clark, Keith Refson, and Cedric Weber, 2018, "Many-body renormalization of forces in *f*-electron materials," Phys. Rev. B **98**, 075129.

Po, Hoi Chun, Ashvin Vishwanath, and Haruki Watanabe, 2017, "Symmetry-based indicators of band topology in the 230 space groups," Nat. Commun. **8**, 50.

Poncé, S., Y. Gillet, J. Laflamme Janssen, A. Marini, M. Verstraete, and X. Gonze, 2015, "Temperature dependence of the electronic structure of semiconductors and insulators," J. Chem. Phys. **143**, 102813.

Poncé, S., E. R. Margine, C. Verdi, and F. Giustino, 2016, "EPW: Electron-phonon coupling, transport and superconducting properties using maximally localized Wannier functions," Comput. Phys. Commun. **209**, 116.

Poncé, Samuel, Wenbin Li, Sven Reichardt, and Feliciano Giustino, 2020, "First-principles calculations of charge carrier mobility and conductivity in bulk semiconductors and two-dimensional materials," Rep. Prog. Phys. **83**, 036501.

Poncé, Samuel, Francesco Macheda, Elena Roxana Margine, Nicola Marzari, Nicola Bonini, and Feliciano Giustino, 2021, "First-principles predictions of Hall and drift mobilities in semiconductors," Phys. Rev. Res. **3**, 043022.

Poncé, Samuel, Elena R. Margine, and Feliciano Giustino, 2018, "Towards predictive many-body calculations of phonon-limited carrier mobilities in semiconductors," Phys. Rev. B **97**, 121201.

Poncé, Samuel, Miquel Royo, Marco Gibertini, Nicola Marzari, and Massimiliano Stengel, 2023, "Accurate Prediction of Hall Mobilities in Two-Dimensional Materials through Gauge-Covariant Quadrupolar Contributions," Phys. Rev. Lett. **130**, 166301.

Poncé, Samuel, Miquel Royo, Massimiliano Stengel, Nicola Marzari, and Marco Gibertini, 2023, "Long-range electrostatic contribution to electron-phonon couplings and mobilities of two-dimensional and bulk materials," Phys. Rev. B **107**, 155424.

Ponet, Louis, 2023, computer code DFWannier.jl,https://github.com/louisponet/DFWannier.jl.

Posternak, Michel, Alfonso Baldereschi, Sandro Massidda, and Nicola Marzari, 2002, "Maximally localized Wannier functions in antiferromagnetic MnO within the FLAPW formalism," Phys. Rev. B **65**, 184422.

Pozo Ocaña, Óscar, and Ivo Souza, 2023, "Multipole theory of optical spatial dispersion in crystals," SciPost Phys. **14**, 118.

Prentice, Joseph C. A., *et al.*, 2020, "The ONETEP linear-scaling density functional theory program, J. Chem. Phys. **152**, 174111.

Protik, Nakib H., and David A. Broido, 2020, "Coupled transport of phonons and carriers in semiconductors: A case study of *n*-doped GaAs," Phys. Rev. B **101**, 075202.

Protik, Nakib H., and Boris Kozinsky, 2020, "Electron-phonon drag enhancement of transport properties from a fully coupled *ab initio* Boltzmann formalism," Phys. Rev. B **102**, 245202.

Protik, Nakib H., Chunhua Li, Miguel Pruneda, David Broido, and Pablo Ordejón, 2022, "The elphbolt *ab initio* solver for the coupled electron-phonon Boltzmann transport equations," npj Comput. Mater. **8**, 28.

Provost, J. P., and G. Vallee, 1980, "Riemannian structure on manifolds of quantum states," Commun. Math. Phys. **76**, 289–301.

PythTB Collaboration, 2023, computer code PythTB, http://www.physics.rutgers.edu/pythtb/about.html.

Qian, Xiaofeng, Ju Li, Liang Qi, Cai-Zhuang Wang, Tzu-Liang Chan, Yong-Xin Yao, Kai-Ming Ho, and Sidney Yip, 2008, "Quasiatomic orbitals for *ab initio* tight-binding analysis," Phys. Rev. B **78**, 245112.

Qiao, Junfeng, Giovanni Pizzi, and Nicola Marzari, 2023a, "Automated mixing of maximally localized Wannier functions into target manifolds," npj Comput. Mater. **9**, 206.

Qiao, Junfeng, Giovanni Pizzi, and Nicola Marzari, 2023b, "Projectability disentanglement for accurate and automated electronic-structure Hamiltonians," npj Comput. Mater. **9**, 208.

Qiao, Junfeng, Giovanni Pizzi, and Nicola Marzari, 2023c, computer code WannierIO.jl, https://github.com/qiaojunfeng/WannierIO.jl (accessed on December 11, 2023).

Qiao, Junfeng, Giovanni Pizzi, and Nicola Marzari, 2023d, computer code Wannier.jl, https://wannierjl.org (accessed on July 5, 2023).

Qiao, Junfeng, Jiaqi Zhou, Zhe Yuan, and Weisheng Zhao, 2018, "Calculation of intrinsic spin Hall conductivity by Wannier interpolation," Phys. Rev. B **98**, 214402.

Quantum ESPRESSO Collaboration,, 2023, computer code Quantum ESPRESSO, https://www.quantum-espresso.org.

Ratcliff, Laura E., *et al.*, 2020, "Flexibilities of wavelets as a computational basis set for large-scale electronic structure calculations," J. Chem. Phys. **152**, 194110.

Resta, Raffaele, 1992, "Theory of the electric polarization in crystals," Ferroelectrics **136**, 51–55.

Resta, Raffaele, 1994, "Macroscopic polarization in crystalline dielectrics: The geometric phase approach," Rev. Mod. Phys. **66**, 899–915.

Rew, R., and G. Davis, 1990, "NetCDF: An interface for scientific data access," IEEE Comput. Graphics Appl. **10**, 76–82.

Roberts, K. V., 1969, "The publication of scientific Fortran programs," Comput. Phys. Commun. **1**, 1–9.

Rocca, Dario, Ralph Gebauer, Yousef Saad, and Stefano Baroni, 2008, "Turbo charging time-dependent density-functional theory with Lanczos chains," J. Chem. Phys. **128**, 154105.

Rocca, Dario, Deyu Lu, and Giulia Galli, 2010, "*Ab initio* calculations of optical absorption spectra: Solution of the Bethe-Salpeter equation within density matrix perturbation theory," J. Chem. Phys. **133**, 164109.

Rocha, A. R., V. M. García-Suárez, S. Bailey, C. Lambert, J. Ferrer, and S. Sanvito, 2006, "Spin and molecular electronics in atomically generated orbital landscapes," Phys. Rev. B **73**, 085414.

Rohlfing, Michael, and Steven G. Louie, 2000, "Electron-hole excitations and optical spectra from first principles," Phys. Rev. B **62**, 4927–4944.

Rohringer, G., H. Hafermann, A. Toschi, A. A. Katanin, A. E. Antipov, M. I. Katsnelson, A. I. Lichtenstein, A. N. Rubtsov, and K. Held, 2018, "Diagrammatic routes to nonlocal correlations beyond dynamical mean field theory," Rev. Mod. Phys. **90**, 025003.

Romero, Aldo H., *et al.*, 2020, "ABINIT: Overview and focus on selected capabilities," J. Chem. Phys. **152**, 124102.

Rösner, M. and E. Şaşıoğlu, C. Friedrich, S. Blügel, and T. O. Wehling, 2015, "Wannier function approach to realistic Coulomb interactions in layered materials and heterostructures," Phys. Rev. B **92**, 085102.

Royo, Miquel, and Massimiliano Stengel, 2019, "First-Principles Theory of Spatial Dispersion: Dynamical Quadrupoles and Flexoelectricity," Phys. Rev. X **9**, 021050.

Royo, Miquel, and Massimiliano Stengel, 2021, "Exact Long-Range Dielectric Screening and Interatomic Force Constants in Quasi-Two-Dimensional Crystals," Phys. Rev. X **11**, 041027.

Ryoo, Ji Hoon, Cheol-Hwan Park, and Ivo Souza, 2019, "Computation of intrinsic spin Hall conductivities from first principles using maximally localized Wannier functions," Phys. Rev. B **99**, 235113.

Sakai, Akito, *et al.*, 2020, "Iron-based binary ferromagnets for transverse thermoelectric conversion," Nature (London) **581**, 53.

Sakuma, R., 2013, "Symmetry-adapted Wannier functions in the maximal localization procedure," Phys. Rev. B **87**, 235109.

Sancho, M. P. Lopez, J. M. Lopez Sancho, and J. Rubio, 1984, "Quick iterative scheme for the calculation of transfer matrices: Application to Mo (100)," J. Phys. F **14**, 1205.

Sangalli, D., *et al.*, 2019, "Many-body perturbation theory calculations using the `Yambo` code," J. Phys. Condens. Matter **31**, 325902.

Sarangapani, Prasad, James Charles, and Tillmann Kubis, 2022, "Tuning Band Tails in Mono- and Multilayered Transition-Metal Dichalcogenides: A Detailed Assessment and a Quick-Reference Guide," Phys. Rev. Appl. **17**, 024005.

Satpathy, S., and Z. Pawlowska, 1988, "Construction of bond-centered Wannier functions for silicon valence bands," Phys. Status Solidi (b) **145**, 555–565.

Savrasov, S. Yu., 1992, "Linear Response Calculations of Lattice Dynamics Using Muffin-Tin Basis Sets," Phys. Rev. Lett. **69**, 2819–2822.

Schüler, M., O. E. Peil, G. J. Kraberger, R. Pordzik, M. Marsman, G. Kresse, T. O. Wehling, and M. Aichhorn, 2018, "Charge self-consistent many-body corrections using optimized projected localized orbitals," J. Phys. Condens. Matter **30**, 475901.

Schüler, Michael, Jacob A. Marks, Yuta Murakami, Chunjing Jia, and Thomas P. Devereaux, 2021, "Gauge invariance of light-matter interactions in first-principle tight-binding models," Phys. Rev. B **103**, 155409.

Schulz, Werner W., Philip B. Allen, and Nandini Trivedi, 1992, "Hall coefficient of cubic metals," Phys. Rev. B **45**, 10886–10890.

Schwalbe-Koda, Daniel, 2023, "`mkite`: A distributed computing platform for high-throughput materials simulations," Comput. Mater. Sci. **230**, 112439.

Sgiarovello, Claudia, Maria Peressi, and Raffaele Resta, 2001, "Electron localization in the insulating state: Application to crystalline semiconductors," Phys. Rev. B **64**, 115202.

Shelley, Matthew, Nicolas Poilvert, Arash A. Mostofi, and Nicola Marzari, 2011, "Automated quantum conductance calculations using maximally-localised Wannier functions," Comput. Phys. Commun. **182**, 2174–2183.

Sheng, Nan, Christian Vorwerk, Marco Govoni, and Giulia Galli, 2022, "Green's function formulation of quantum defect embedding theory," J. Chem. Theory Comput. **18**, 3512–3522.

Shinaoka, Hiroshi, Junya Otsuki, Mitsuaki Kawamura, Nayuta Takemori, and Kazuyoshi Yoshimi, 2021, "`DCore`: Integrated DMFT software for correlated electrons," SciPost Phys. **10**, 117.

Silvestrelli, Pier Luigi, 1999, "Maximally localized Wannier functions for simulations with supercells of general symmetry," Phys. Rev. B **59**, 9703–9706.

Singh, Vijay, Uthpala Herath, Benny Wah, Xingyu Liao, Aldo H. Romero, and Hyowon Park, 2021, "`DMFTwDFT`: An open-source code combining dynamical mean field theory with various density functional theory packages," Comput. Phys. Commun. **261**, 107778.

Sio, Weng Hong, and Feliciano Giustino, 2022, "Unified *ab initio* description of Fröhlich electron-phonon interactions in two-dimensional and three-dimensional materials," Phys. Rev. B **105**, 115414.

Sio, Weng Hong, and Feliciano Giustino, 2023, "Polarons in two-dimensional atomic crystals," Nat. Phys. **19**, 629.

Sio, Weng Hong, Carla Verdi, Samuel Poncé, and Feliciano Giustino, 2019, "Polarons from First Principles, without Supercells," Phys. Rev. Lett. **122**, 246403.

Sjakste, J., N. Vast, M. Calandra, and F. Mauri, 2015, "Wannier interpolation of the electron-phonon matrix elements in polar semiconductors: Polar-optical coupling in GaAs," Phys. Rev. B **92**, 054307.

Skone, Jonathan H., Marco Govoni, and Giulia Galli, 2014, "Self-consistent hybrid functional for condensed systems," Phys. Rev. B **89**, 195112.

Sodemann, Inti, and Liang Fu, 2015, "Quantum Nonlinear Hall Effect Induced by Berry Curvature Dipole in Time-Reversal Invariant Materials," Phys. Rev. Lett. **115**, 216806.

Sohier, Thibault, Matteo Calandra, and Francesco Mauri, 2016, "Two-dimensional Fröhlich interaction in transition-metal dichalcogenide monolayers: Theoretical modeling and first-principles calculations," Phys. Rev. B **94**, 085415.

Soler, José M., Emilio Artacho, Julian D. Gale, Alberto García, Javier Junquera, Pablo Ordejón, and Daniel Sánchez-Portal, 2002, "The SIESTA method for *ab initio* order-*N* materials simulation," J. Phys. Condens. Matter **14**, 2745–2779.

Soluyanov, Alexey A., and David Vanderbilt, 2011a, "Computing topological invariants without inversion symmetry," Phys. Rev. B **83**, 235401.

Soluyanov, Alexey A., and David Vanderbilt, 2011b, "Wannier representation of $\mathbb{Z}_2$ topological insulators," Phys. Rev. B **83**, 035108.

Song, Zhida, Tiantian Zhang, Zhong Fang, and Chen Fang, 2018, "Quantitative mappings between symmetry and topology in solids," Nat. Commun. **9**, 3530.

Sorensen, H. V., and C. S. Burrus, 1993, "Efficient computation of the DFT with only a subset of input or output points," IEEE Trans. Signal Process. **41**, 1184–1200.

Souza, Ivo, Nicola Marzari, and David Vanderbilt, 2001, "Maximally localized Wannier functions for entangled energy bands," Phys. Rev. B **65**, 035109.

Sporkmann, B., and H. Bross, 1994, "Calculation of Wannier functions for fcc transition metals by Fourier transformation of Bloch functions," Phys. Rev. B **49**, 10869–10876.

SSCHA Collaboration, 2023, computer code `SSCHA`, https://sscha.eu/.

Stefanucci, Gianluca, Robert van Leeuwen, and Enrico Perfetto, 2023, "In and Out-of-Equilibrium *Ab Initio* Theory of Electrons and Phonons," Phys. Rev. X **13**, 031026.

Stengel, Massimiliano, and Nicola A. Spaldin, 2006, "Accurate polarization within a unified Wannier function formalism," Phys. Rev. B **73**, 075121.

StraWBerryPy Collaboration, 2023, computer code `StraWBerryPy`, https://github.com/strawberrypy-developers/strawberrypy.git.

Stubbs, Kevin D., Alexander B. Watson, and Jianfeng Lu, 2021, "Iterated projected position algorithm for constructing exponentially localized generalized Wannier functions for periodic and nonperiodic insulators in two dimensions and higher," Phys. Rev. B **103**, 075125.

Sun, Qiming, *et al.*, 2018, "PySCF: The Python-based simulations of chemistry framework," Comput. Mol. Sci. **8**, e1340.
Sun, Qiming, *et al.*, 2020, "Recent developments in the PySCF program package," J. Chem. Phys. **153**, 024109.
Supka, Andrew R., *et al.*, 2017, "AFLOWπ: A minimalist approach to high-throughput *ab initio* calculations including the generation of tight-binding Hamiltonians," Comput. Mater. Sci. **136**, 76–84.
Taherinejad, Maryam, Kevin F. Garrity, and David Vanderbilt, 2014, "Wannier center sheets in topological insulators," Phys. Rev. B **89**, 115102.
Talirz, Leopold, Luca M. Ghiringhelli, and Berend Smit, 2021, "Trends in atomistic simulation software usage [article v1.0]," Living J. Comput. Mol. Sci. **3**, 1483.
Talirz, Leopold, *et al.*, 2020, "Materials Cloud, a platform for open computational science," Sci. Data **7**, 299.
Tancogne-Dejean, Nicolas, *et al.*, 2020, "Octopus, a computational framework for exploring light-driven phenomena and quantum dynamics in extended and finite systems, J. Chem. Phys. **152**, 124119.
Tang, Feng, Hoi Po, Ashvin Vishwanath, and Xiangang Wan, 2019, "Comprehensive search for topological materials using symmetry indicators," Nature (London) **566**, 486–489.
TBmodels Collaboration, 2023, computer code TBmodels, https://tbmodels.greschd.ch/en/latest/index.html.
TDEP Collaboration, 2023, computer code TDEP, https://tdep-developers.github.io/tdep/.
Thonhauser, T., D. Ceresoli, D. Vanderbilt, and R. Resta, 2005, "Orbital Magnetization in Periodic Insulators," Phys. Rev. Lett. **95**, 137205.
Thonhauser, T., and D. Vanderbilt, 2006, "Insulator/Chern-insulator transition in the Haldane model," Phys. Rev. B **74**, 235111.
Thunström, P., I. Di Marco, A. Grechnev, S. Lebègue, M. I. Katsnelson, A. Svane, and O. Eriksson, 2009, "Multiplet effects in the electronic structure of intermediate-valence compounds," Phys. Rev. B **79**, 165104.
Thygesen, K. S., L. B. Hansen, and K. W. Jacobsen, 2005, "Partly Occupied Wannier Functions," Phys. Rev. Lett. **94**, 026405.
Thygesen, K. S., and K. W. Jacobsen, 2005, "Molecular transport calculations with Wannier functions," Chem. Phys. **319**, 111–125.
Thygesen, Kristian S., and Angel Rubio, 2008, "Conserving *GW* scheme for nonequilibrium quantum transport in molecular contacts," Phys. Rev. B **77**, 115333.
Tillack, Sebastian, Andris Gulans, and Claudia Draxl, 2020, "Maximally localized Wannier functions within the (L)APW + LO method," Phys. Rev. B **101**, 235102.
Tokura, Yoshinori, Masashi Kawasaki, and Naoto Nagaosa, 2017, "Emergent functions of quantum materials," Nat. Phys. **13**, 1056–1068.
Tomassetti, Charlsey R., Gyanu P. Kafle, Edan T. Marcial, Elena R. Margine, and Aleksey N. Kolmogorov, 2024, "Prospect of high-temperature superconductivity in layered metal borocarbides," J. Mater. Chem. C **12**, 4870–4884.
Tomczak, Jan M., Kristjan Haule, and Gabriel Kotliar, 2012, "Signatures of electronic correlations in iron silicide," Proc. Natl. Acad. Sci. U.S.A. **109**, 3243–3246.
Tsirkin, Stepan S., 2021, "High performance Wannier interpolation of Berry curvature and related quantities with WannierBerri code," npj Comput. Mater. **7**, 33.
Tsirkin, Stepan S., Ivo Souza, and David Vanderbilt, 2017, "Composite Weyl nodes stabilized by screw symmetry with and without time-reversal invariance," Phys. Rev. B **96**, 045102.
Uehara, Kentaro, and John S. Tse, 2000, "Calculations of transport properties with the linearized augmented plane-wave method," Phys. Rev. B **61**, 1639–1642.
Uhrin, Martin, Sebastiaan P. Huber, Jusong Yu, Nicola Marzari, and Giovanni Pizzi, 2021, "Workflows in AiiDA: Engineering a high-throughput, event-based engine for robust and modular computational workflows," Comput. Mater. Sci. **187**, 110086.
Umari, P., X. Qian, N. Marzari, G. Stenuit, L. Giacomazzi, and S. Baroni, 2011, "Accelerating *GW* calculations with optimal polarizability basis," Phys. Status Solidi (b) **248**, 527–536.
Uría-Álvarez, Alejandro José, Juan José Esteve-Paredes, M. A. García-Blázquez, and Juan José Palacios, 2024, "Efficient computation of optical excitations in two-dimensional materials with the Xatu code," Comput. Phys. Commun. **295**, 109001.
Vanderbilt, D., 2018, *Berry Phases in Electronic Structure Theory: Electric Polarization, Orbital Magnetization and Topological Insulators* (Cambridge University Press, Cambridge, England).
Vanderbilt, David, and R. D. King-Smith, 1993, "Electric polarization as a bulk quantity and its relation to surface charge," Phys. Rev. B **48**, 4442–4455.
Van Muñoz, Lorenzo, Sophie Beck, and Jason Kaye, 2024, "AutoBZ.jl: Automatic, adaptive Brillouin zone integration using Wannier interpolation," J. Open Source Software **9**, 7080.
Van Muñoz, Lorenzo, Jason Kaye, Alex Barnett, and Sophie Beck, 2024, "High-order and adaptive optical conductivity calculations using Wannier interpolation," arXiv:2406.15466.
Varnava, Nicodemos, Ivo Souza, and David Vanderbilt, 2020, "Axion coupling in the hybrid Wannier representation," Phys. Rev. B **101**, 155130.
Verdi, Carla, and Feliciano Giustino, 2015, "Fröhlich Electron-Phonon Vertex from First Principles," Phys. Rev. Lett. **115**, 176401.
Vergniory, M. G., L. Elcoro, Claudia Felser, Nicolas Regnault, B. Andrei Bernevig, and Zhijun Wang, 2019, "A complete catalogue of high-quality topological materials," Nature (London) **566**, 480–485.
Vergniory, M. G., L. Elcoro, Zhijun Wang, Jennifer Cano, C. Felser, M. I. Aroyo, B. Andrei Bernevig, and Barry Bradlyn, 2017, "Graph theory data for topological quantum chemistry," Phys. Rev. E **96**, 023310.
Vitale, Valerio, Giovanni Pizzi, Antimo Marrazzo, Jonathan R. Yates, Nicola Marzari, and Arash A. Mostofi, 2020, "Automated high-throughput Wannierisation," npj Comput. Mater. **6**, 1–18.
Vogl, P., 1976, "Microscopic theory of electron-phonon interaction in insulators or semiconductors," Phys. Rev. B **13**, 694–704.
Walker, Brent, A. Marco Saitta, Ralph Gebauer, and Stefano Baroni, 2006, "Efficient Approach to Time-Dependent Density-Functional Perturbation Theory for Optical Spectroscopy," Phys. Rev. Lett. **96**, 113001.
Wallerberger, Markus, Andreas Hausoel, Patrik Gunacker, Alexander Kowalski, Nicolaus Parragh, Florian Goth, Karsten Held, and Giorgio Sangiovanni, 2019, "w2dynamics: Local one- and two-particle quantities from dynamical mean field theory," Comput. Phys. Commun. **235**, 388–399.
Wang, Chong, Xiaoyu Liu, Lei Kang, Bing-Lin Gu, Yong Xu, and Wenhui Duan, 2017, "First-principles calculation of nonlinear optical responses by Wannier interpolation," Phys. Rev. B **96**, 115147.
Wang, Chong, Sibo Zhao, Xiaomi Guo, Xinguo Ren, Bing-Lin Gu, Yong Xu, and Wenhui Duan, 2019, "First-principles calculation of optical responses based on nonorthogonal localized orbitals," New J. Phys. **21**, 093001.

Wang, Jing, and Shou-Cheng Zhang, 2017, "Topological states of condensed matter," Nat. Mater. **16**, 1062–1067.

Wang, Kuang-Chung, Daniel Valencia, James Charles, Alex Henning, Megan E. Beck, Vinod K. Sangwan, Lincoln J. Lauhon, Mark C. Hersam, and Tillmann Kubis, 2021, "Atomic-level charge transport mechanism in gate-tunable anti-ambipolar van der Waals heterojunctions," Appl. Phys. Lett. **118**, 083103.

Wang, Kuang-Chung, *et al.*, 2017, "Control of interlayer physics in 2H transition metal dichalcogenides," J. Appl. Phys. **122**, 224302.

Wang, Runzhi, Emanuel A. Lazar, Hyowon Park, Andrew J. Millis, and Chris A. Marianetti, 2014, "Selectively localized Wannier functions," Phys. Rev. B **90**, 165125.

Wang, Xin, Emanuel Gull, Luca de' Medici, Massimo Capone, and Andrew J. Millis, 2009, "Antiferromagnetism and the gap of a Mott insulator: Results from analytic continuation of the self-energy," Phys. Rev. B **80**, 045101.

Wang, Xinjie, David Vanderbilt, Jonathan R. Yates, and Ivo Souza, 2007, "Fermi-surface calculation of the anomalous Hall conductivity," Phys. Rev. B **76**, 195109.

Wang, Xinjie, Jonathan R. Yates, Ivo Souza, and David Vanderbilt, 2006, "*Ab initio* calculation of the anomalous Hall conductivity by Wannier interpolation," Phys. Rev. B **74**, 195118.

Wang, Y. L., G. Fabbris, M. P. M. Dean, and G. Kotliar, 2019, "`EDRIXS`: An open source toolkit for simulating spectra of resonant inelastic x-ray scattering," Comput. Phys. Commun. **243**, 151–165.

Wannier, Gregory H., 1937, "The structure of electronic excitation levels in insulating crystals," Phys. Rev. **52**, 191–197.

Weinan, E., Carlos J. García-Cervera, and Jianfeng Lu, 2007, "A sub-linear scaling algorithm for computing the electronic structure of materials," Commun. Math. Sci. **5**, 999–1026.

Weng, Hongming, Taisuke Ozaki, and Kiyoyuki Terakura, 2009, "Revisiting magnetic coupling in transition-metal-benzene complexes with maximally localized Wannier functions," Phys. Rev. B **79**, 235118.

Werner, Philipp, and Michele Casula, 2016, "Dynamical screening in correlated electron systems—From lattice models to realistic materials," J. Phys. Condens. Matter **28**, 383001.

Wieder, Benjamin J., *et al.*, 2022, "Topological materials discovery from crystal symmetry," Nat. Rev. Mater. **7**, 196–216.

Wing, Dahvyd, Guy Ohad, Jonah B. Haber, Marina R. Filip, Stephen E. Gant, Jeffrey B. Neaton, and Leeor Kronik, 2021, "Band gaps of crystalline solids from Wannier-localization-based optimal tuning of a screened range-separated hybrid functional," Proc. Natl. Acad. Sci. U.S.A. **118**, e2104556118.

Wissgott, P., J. Kuneš, A. Toschi, and K. Held, 2012, "Dipole matrix element approach versus Peierls approximation for optical conductivity," Phys. Rev. B **85**, 205133.

Wissgott, P., A. Toschi, H. Usui, K. Kuroki, and K. Held, 2010, "Enhancement of the Na_xCoO_2 thermopower due to electronic correlations," Phys. Rev. B **82**, 201106.

Wortmann, Daniel, *et al.*, 2023, computer code `FLEUR`, https://zenodo.org/records/7891361.

Wu, QuanSheng, ShengNan Zhang, Hai-Feng Song, Matthias Troyer, and Alexey A. Soluyanov, 2018, "`WannierTools`: An open-source software package for novel topological materials," Comput. Phys. Commun. **224**, 405–416.

Wu, Xifan, Annabella Selloni, and Roberto Car, 2009, "Order-*n* implementation of exact exchange in extended insulating systems," Phys. Rev. B **79**, 085102.

Xiao, D., M.-C. Chang, and Q. Niu, 2010, "Berry phase effects on electronic properties," Rev. Mod. Phys. **82**, 1959.

Xiao, Di, Junren Shi, and Qian Niu, 2005, "Berry Phase Correction to Electron Density of States in Solids," Phys. Rev. Lett. **95**, 137204.

Xiao, Di, Yugui Yao, Zhong Fang, and Qian Niu, 2006, "Berry-Phase Effect in Anomalous Thermoelectric Transport," Phys. Rev. Lett. **97**, 026603.

Yang, Shuo-Ying, Hao Yang, Elena Derunova, Stuart S. P. Parkin, Binghai Yan, and Mazhar N. Ali, 2018, "Symmetry demanded topological nodal-line materials," Adv. Phys. X **3**, 1414631.

Yao, Yugui, Leonard Kleinman, A. H. MacDonald, Jairo Sinova, T. Jungwirth, Ding-sheng Wang, Enge Wang, and Qian Niu, 2004, "First Principles Calculation of Anomalous Hall Conductivity in Ferromagnetic bcc Fe," Phys. Rev. Lett. **92**, 037204.

Yates, Jonathan R., Xinjie Wang, David Vanderbilt, and Ivo Souza, 2007, "Spectral and Fermi surface properties from Wannier interpolation," Phys. Rev. B **75**, 195121.

Yin, M. T., and Marvin L. Cohen, 1980, "Microscopic Theory of the Phase Transformation and Lattice Dynamics of Si," Phys. Rev. Lett. **45**, 1004–1007.

Yokouchi, Tomoyuki, Yuya Ikeda, Takahiro Morimoto, and Yuki Shiomi, 2023, "Giant Magnetochiral Anisotropy in Weyl Semimetal WTe_2 Induced by Diverging Berry Curvature," Phys. Rev. Lett. **130**, 136301.

Yoon, Hongkee, Taek Jung Kim, Jae-Hoon Sim, and Myung Joon Han, 2020, "`Jx`: An open-source software for calculating magnetic interactions based on magnetic force theory," Comput. Phys. Commun. **247**, 106927.

Yu, Rui, Xiao Liang Qi, Andrei Bernevig, Zhong Fang, and Xi Dai, 2011, "Equivalent expression of $\mathbb{Z}_2$ topological invariant for band insulators using the non-Abelian Berry connection," Phys. Rev. B **84**, 075119.

Yusufaly, Tahir, David Vanderbilt, and Sinisa Coh, 2023, "`PythTB` tight-binding formalism and conventions," https://www.physics.rutgers.edu/pythtb/_downloads/e39c23ce476d399b268efa520e7a9091/pythtb-formalism.pdf (accessed June 20, 2023).

Z2Pack Collaboration, 2023, computer code `Z2Pack`, https://z2pack.greschd.ch/en/latest/index.html.

Zacharias, Marios, and Feliciano Giustino, 2016, "One-shot calculation of temperature-dependent optical spectra and phonon-induced band-gap renormalization," Phys. Rev. B **94**, 075125.

Zacharias, Marios, and Feliciano Giustino, 2020, "Theory of the special displacement method for electronic structure calculations at finite temperature," Phys. Rev. Res. **2**, 013357.

Zacharias, Marios, George Volonakis, Feliciano Giustino, and Jacky Even, 2023a, "Anharmonic lattice dynamics via the special displacement method," Phys. Rev. B **108**, 035155.

Zacharias, Marios, George Volonakis, Feliciano Giustino, and Jacky Even, 2023b, "Anharmonic lattice dynamics via the special displacement method," npj Comput. Mater. **9**, 153.

Zak, J., 1982, "Band representations of space groups," Phys. Rev. B **26**, 3010–3023.

Zak, J., 1989, "Berry's Phase for Energy Bands in Solids," Phys. Rev. Lett. **62**, 2747–2750.

Železný, Jakub, 2023, computer code `Wannier linear response`, https://bitbucket.org/zeleznyj/wannier-linear-response/wiki/Home.

Zgid, Dominika, and Emanuel Gull, 2017, "Finite temperature quantum embedding theories for correlated systems," New J. Phys. **19**, 023047.

Zhang, Chenmu, and Yuanyue Liu, 2022, "Phonon-limited transport of two-dimensional semiconductors: Quadrupole scattering and free carrier screening," Phys. Rev. B **106**, 115423.

Zhang, Tiantian, Yi Jiang, Zhida Song, He Huang, Yuqing He, Zhong Fang, Hongming Weng, and Chen Fang, 2019, "Catalogue of topological electronic materials," Nature (London) **566**, 475–479.

Zhang, Xiao, Guangsha Shi, Joshua A. Leveillee, Feliciano Giustino, and Emmanouil Kioupakis, 2022, "*Ab initio* theory of free-carrier absorption in semiconductors," Phys. Rev. B **106**, 205203.

Zhi, Guo-Xiang, Chenchao Xu, Si-Qi Wu, Fanlong Ning, and Chao Cao, 2022, "`WannSymm`: A symmetry analysis code for Wannier orbitals," Comput. Phys. Commun. **271**, 108196.

Zhou, Jin-Jian, and Marco Bernardi, 2019, "Predicting charge transport in the presence of polarons: The beyond-quasiparticle regime in $SrTiO_3$," Phys. Rev. Res. **1**, 033138.

Zhou, Jin-Jian, Jinsoo Park, I-Te Lu, Ivan Maliyov, Xiao Tong, and Marco Bernardi, 2021, "`PERTURBO`: A software package for *ab initio* electron-phonon interactions, charge transport and ultrafast dynamics," Comput. Phys. Commun. **264**, 107970.

Zhou, Jin-Jian, Jinsoo Park, Iurii Timrov, Andrea Floris, Matteo Cococcioni, Nicola Marzari, and Marco Bernardi, 2021, "*Ab Initio* Electron-Phonon Interactions in Correlated Electron Systems," Phys. Rev. Lett. **127**, 126404.

Zicovich-Wilson, Claudio M., Roberto Dovesi, and Victor R. Saunders, 2001, "A general method to obtain well localized Wannier functions for composite energy bands in linear combination of atomic orbital periodic calculations," J. Chem. Phys. **115**, 9708–9719.

Ziman, J., 1972, *Principles of the Theory of Solids*, 2nd ed. (Cambridge University Press, Cambridge, England).

Zingl, Manuel, Jernej Mravlje, Markus Aichhorn, Olivier Parcollet, and Antoine Georges, 2019, "Hall coefficient signals orbital differentiation in the Hund's metal Sr_2RuO_4," npj Quantum Mater. **4**, 35.